On the fatigue behavior of ductile F.C.C. metals

Thesis by

Eduardo A. Repetto

In Partial Fulfillment of the Requirements

for the Degree of

Doctor of Philosophy

California Institute of Technology

Pasadena, California

1998

(Submitted August 15, 1997)

Aquí me pongo a cantar
al compás de la vigüela,
que el hombre que lo desvela
una pena estrordinaria,
como la ave solitaria
con el cantar se consuela.

Pido a los santos del cielo
que ayuden mi pensamiento:
les pido en este momento
que voy a cantar mi historia
me refresquen la memoria
y aclaren mi entendimiento.

El gaucho Martín Fierro (1872),
José Hernandez (1834-1886)

to Roberto, Helda, Roxana, Enrique and Carla

Acknowledgements

I would like to express my gratitude to Professor Michael Ortiz, my advisor, for his continuous support, guidance and ideas.

I am also thankful to the professors of the Solids Mechanics Division of the Graduate Aeronautical Laboratory and the ones of the Applied Mechanics Department at Caltech.

It would not be fair to forget my former professors at Brown University that have guided me during my first two years of graduate school.

I would also like to thank Alberto Cuitiño and Gustavo Gioia for their example and advice, and Sonia Oliveira, David Owen and Raúl Radovitzky for the fruitful interactions that I have mantained with them.

The support of the Office of Naval Research under grant N00014-96-1-0068 is gratefully acknowledged.

Abstract

A micromechanically based model for fatigue crack nucleation in ductile F.C.C. metals is developed. The theory includes a model of F.C.C. crystal-plasticity in finite deformations that takes into account the Bauschinger effect, dipole annihilation in the persistent slip bands (PSBs), with vacancy generation and PSB elongation as a byproduct, as well as coupled vacancy diffusion and the attendant surface motion due to the flux of vacancies out of the body.

Finite element simulations are performed in order to establish the predictive capability of the theory. Detailed modelling of the intersection of the PSB with a free surface, enhanced by the use of remeshing and surface evolution techniques, enable the prediction of nucleation sites, life expectancy, surface profile, alternate slip between the sides of the PSB and strain localization at the grooves.

In an attempt to resolve the dislocation structures experimentally observed during cyclic loading, a theory based on the non-convexity of a pseudo-energy density is developed. Non-homogeneous minimizers are found containing variants oriented in coincidence with the dislocation walls observed experimentally. Due to the latent hardening and geometrical softening, the minimizing structures are found to consist of regions of single slip which is in accordance with the observed "patchy slip."

Contents

List of Figures

List of Tables

Chapter 1 Introduction

Engineers and designers have been aware of fatigue failure for over 150 years. In the early nineteeth century, with the arrival of steam machinery, failure due to fatigue started to show its relevance. Engineers, mostly in the mining and railway industries, began studies of the behavior of metal parts subject to cyclic loads.

The first work on fatigue is believed to be that of W. A. J. Albert in the 1830s [Alb38]. He was interested in the cyclic behavior of mine-hoist chains made of welded iron and conducted experiments of up to 10^5 cycles. Bending test on beams were performed as early as 1840s by E. A. Hodgkinson [Hod49] and Fairbairn [Fai64]. Whöler discovered that the fatigue life of specimens is determined by the range of applied stress (S-N curves) and that there is a stress under which specimens would not fail by fatigue (endurance limit). The fact that the yield strength decreases with load reversals, referred as Bauschinger effect, was reported for the first time in the 1880s.

In 1903 Ewing and Humfrey performed experiments on iron. By examining the free surfaces, they discovered that the fatigue failure is related to slip band formation and broadening [EH03]. They also noticed that the crack nucleation sites coincide with the places where the bands broaden, thus taking the first steps in the physical characterization of the fatigue phenomena.

In the mid-1950s, Coffin [Cof54] and Mason established the dependence of fatigue life on the plastic strains through a phenomenological approach. They noticed a linear relation between the logarithm of the plastic amplitude and number of cycles from which they were able to deduce the life expectancy of specimens.

In 1961 Paris *et al.* ([PGA61]; [PE63]) established that the crack growth rate per cycle, da/dN, is proportional to a power of the difference between the applied stress intensity factors, ΔK, *i.e.*, $da/DN \approx C(\Delta K)^m$, a relation presently known as the Paris Law.

The phenomenological approaches to fatigue life based on macroscopic variables has found wide use among designers. Stress-based methods, such as the early work of Whöler, can estimate, for a given applied stress amplitude, the number of cycles to failure and the stress range under which no failure occurs, or endurance limit. Strain-based methods, such as that of Coffin and Mason, can also be used to predict the fatigue life. Depending on the amplitudes of the plastic and elastic strains at failure, these methods divide the fatigue process into those that are ductile, with $\Delta\epsilon_{plastic} > \Delta\epsilon_{elastic}$, or strength driven otherwise. The two above-mentioned methods were developed under conditions of constant stress or strain amplitude. By contrast, the Palmgren-Miner rule [Min45] allows for the extension of constant amplitude predictions of fatigue life to varying amplitude.

If the existence of an initial crack is assumed, the Paris Law provides a powerful tool to determine the extent of crack growth. The Paris Law is used extensively in practice to establish inspection intervals for parts and structures subjected to fatigue loading.

The fatigue crack growth phenomenon can be divided in two stages. In stage I, where microstructural effects are of great relevance, the crack path follows slip lines and crack-growth rates are low. In stage II the crack fields extend over presence in a domain surrounding the tip that encompasses many grains. The transition from the first to the second stage occurs when the size of the plastic zone around the crack tip exceeds the grain size. Since the nucleation and initial growth of microcracks is associated with localized surface regions of plastic slip, the early stages of fatigue are independent of the mean tensile stress, but depend on the amplitude of the cycle. Compressive mean stresses prevent the development of macrocracks, but not the initiation of the microcracks. There is plenty of evidence that the existence of stage I microcracks does not imply the growth of them to stage II macrocracks [FMP74].

It has been observed microscopically ([FMP74]; [TWL56]) that in the free surface plays an important role in fatigue processes. In many metals, it is known that transgranular cracks occur more readily at lower temperatures than intergranular cracks, in particular when the surface is not exposed to an aggressive atmosphere [FMP74].

There is evidence that damage in polycrystalline ductile metals is associated with the grains close to the free surface: specimens that have the surface re-polished during the test exhibit a longer life ([TWL56]; [BPB83]). Environmental effects are also of considerable importance in the behavior of surface grains ([GS32]; [TWL56]). In addition, examination of the failure surface of homogeneous specimens does not reveal cracks in the bulk [FMP74].

The majority of the experimental data on fatigue problems has been obtained during the last fifty years of this century. The term persistent slip band (PSB) was first used by Thompson *et al.* [TWL56]. Their fatigue tests were interrupted in order to look for slip bands on the surfaces and then continued. In some of the test they re-polished the surface during the interruptions, finding that slip band traces appear at the same places after restarting the loading. This was a clear evidence that the PSBs are part of a bulk effect and not only a surface perturbation. Forsyth [FS55] was the first to report the extrusion phenomena at the surfaces. The localized slip activity in the PSBs and the attendant produce high dislocation density and vacancy concentration, accounting for the different etching properties observed in the PSB and the matrix.

At room temperature, it has been observed that cracks initiate at the intersection of slip bands with the free surface [FMP74]. Examination of tested specimens by transmission electron microscopy shows that there exists an intricate dislocation arrangement in the bulk of the material. Complex dislocation structures have been observed in many studies, with large number of dislocation loops condensed in the walls [Fel65].

With the use of electron microscopes, many advances have been made in understanding the micromechanics of the fatigue process [Sur91]. Observation of strain localization into PSBs and dislocation structures have been correlated with imposed strain amplitudes and surface roughness. In F.C.C. metals, endurance limits have also been correlated with the formation of PSBs. The absence of strain localization has been found to prevent the formation of cracks ([Lai76]; [BM65]).

The formation of PSBs and their ladder structure has not been explained in a

manner that accounts for all the experimental observations. Different authors have variously endeavored to understand this problem by positing: kinetic instabilities produced by annihilation of dislocations during the activation of a secondary slip system [KWL80]; energy minimization of dislocation structures ([DBL86]; [DHL86]) and instabilities in dislocation motion governed by diffusion-reaction like equation ([WA85]; [Aif87]; [GLL95]), with varying degrees of success.

The first part of this thesis is concerned with the micromechanical understanding of the nucleation of fatigue cracks in F.C.C. single crystals. The fact that in clean specimens with smooth surfaces the fatigue crack nucleation stage can account for up to 80% of the total life [Sur91], and that in ductile metals the fatigue cracks are nucleated in the surface grains, provides impetus for this work.

A micromechanical model is developed which uses multiphysics simulations including: crystal plasticity and a micromechanical based model for the Bauschinger effect; vacancy generation due to dipole annihilation; vacancy diffusion, taking into account the stress-assisted diffusion and an anisotropic diffusivity due to pipe diffusion; and surface profile evolution due to the outward flux of vacancies. The finite element implementation of the theory [RO97] enables the simulation of realistic test conditions. The objectives of the work are: to predict the number of cycles necessary to nucleate a crack; to identify crack initiation sites and probable mechanisms that lead to surface roughness; and to observe the alternate slip in the PSBs and the slip concentration at the grooves, among others.

The second part of the thesis focuses on the dislocation structures (*i.e.*, walls, cells, labyrinth structures) that are experimentally found in cyclic fatigue of F.C.C. metals ([AKLM84]; [Sur91]; [RP80]; [Cha81]). A model based on minimization of a pseudoenergy density is developed which allows for non-homogeneous deformations satisfiying rank-one compatibility at the interface between variants. Due to latent hardening and geometrical softening, single-slip variants are found to be energy minimizers. Dislocations at the interface of the variants form wall structures with orientations that are in accordance with TEM observations. In particular "patchy slip" ([PAN82], [Asa79]), where a uniform global deformation decomposes into different

zones of single slip, is an observed phenomenon. The predicted wall orientations and dislocation structures are found to be in good agreement with published experimental observations.

Chapter 2 Fatigue crack nucleation in F.C.C. ductile metals

2.1 Introduction

Fatigue-crack nucleation often accounts for a substantial part of the fatigue life of components. In clean specimens, with smooth surfaces the nucleation stage can be up to 80% of the life. However, while the observational evidence accumulated to date on the mechanisms underlying fatigue crack initiation is quite copious (see [Sur91] for a recent review), success in developing a quantitative understanding of crack initiation processes has been somewhat limited. Indeed, a micromechanically based computational capability enabling the prediction of the number of cycles to fatigue-crack nucleation appears to be unavailable at present. In this work, we develop a micromechanical finite-element model of fatigue-crack initiation in nominally defect-free pure F.C.C. metals. The scale of observation envisioned is that of a single persistent slip band (PSB) intersecting the free surface of a single crystal. The nucleation event is identified with the formation of a sharp surface crack, whose subsequent growth obeys the laws of fracture mechanics.

Experiments dating back to Thompson *et al.* [TWL56] and, more recently, to Basinski *et al.* [BPB83], have conclusively demonstrated that fatigue-crack nucleation is mediated by surface roughness. This roughness arises at the intersection between the surface and PSBs extending through the entire cross section of the crystal. In the saturation stage of the cyclic behavior of metals, PSBs carry the majority of the deformation. As the PSBs are cycled in shear, they simultaneously elongate and extrude out of the surface, forming surface protrusions ([For53]; [FS55]; [For57]; [CH57]). The re-entrant corners induced by the surface protrusions at the matrix/PSB interface are preferential sites for fatigue-crack nucleation ([ML89b]; [KOK$^+$77]; [BM65]).

The accurate modeling of surface roughening is, therefore, an important stepping stone towards the formulation of micromechanical models of fatigue-crack nucleation.

Essmann, Gösele and Mughrabi [EGM81] developed a comprehensive theory of surface roughening based on the hypothesis that dislocation pair annihilation is the origin of PSB elongation. We take this theory as the basis of our model. However, we have departed from the kinematics proposed by Essmann *et al.* [EGM81], who argued that the net effect of pair annihilation is to tilt the *effective* slip plane away from the plane of the PSBs. We show that PSB elongation can be understood within the conventional kinematics of dislocation motion as the consequence of the *climb* which inevitably accompanies dislocation annihilation. This climb component of the motion of dislocations directly accounts for the elongation of the PSBs and, eventually, for the development of surface extrusions.

An additional byproduct of dislocation pair annihilation is the generation of vast numbers of vacancies. The vacancy concentration within the PSBs is much larger than the vacancy concentration in the matrix, and it greatly exceeds the equilibrium vacancy concentration at the free surface. These concentration differentials promote vacancy diffusion, which is aided by pipe diffusion through the screw segments even at relatively low temperatures. Owing to the dislocation structures which develop within the PSBs, pipe diffusion operates preferentially towards the free surface. The resulting net outward flux of vacancies causes the surface to recede. Our simulations show that this mechanism is particularly effective at the PSB/matrix interface, and contributes to the formation of grooves at those locations. As the specimen is cycled, those grooves steadily sharpen. After a predictable number of cycles, the angle subtended at the groove tip reduces to zero, signalling the nucleation of a sharp crack.

This chapter is organized as follows. In Section 2.2 we succinctly review the salient aspects of the experimental record which form the basis of our model. Copper is adopted as a convenient model material throughout this paper. In Section 2.3, a single-crystal plasticity theory developed by Cuitiño and Ortiz ([CnO92]; [CnO96]) is extended to account for cyclic behavior, PSB elongation due to climb and fully-coupled diffusion. The accuracy of the model is demonstrated by comparison with

cyclic stress-strain data. The finite-element implementation of the theory is discussed in Section 2.4. It bears emphasis that the ability to follow the formation of surface protrusions requires finite deformation capability. To sidestep difficulties associated with deformation-induced mesh distortion, as well as to resolve the fine-scale features of the solution, we resort to automatic and adaptive remeshing. Finally, in Section 2.5 selected simulations are reported which demonstrate the ability of the theory to predict the number of cycles required for fatigue-crack nucleation.

2.2 Experimental background

There is presently a wealth of experimental data concerning the cyclic behavior of single-crystal specimens under uniaxial loading. For completeness and subsequent reference, we begin by reviewing those aspects of the experimental record which form the basis of our model. Crystalline copper is one of the materials which have been most thoroughly investigated and, consequently, we have adopted it as a convenient model material. For simplicity, we confine our review to fully reversed, constant plastic-strain amplitude loading histories. More detailed experimental accounts of fatigue-crack nucleation may be found elsewhere [Sur91].

2.2.1 Saturation stress-strain behavior

During the early stages of loading, the uniaxial cyclic response of single crystals is transient in nature. If the crystal is oriented such that plastic deformation takes place predominantly by single slip, the dislocations gradually orient themselves normal to the slip direction, thereby taking on a predominantly edge character ([BBH69]; [HG69]). The main hardening mechanism consists of the mutual trapping of parallel edge dislocations of opposite sign into dipoles and multipoles, leading to the formation of vein and channel structures. Eventually, a saturation stage is reached wherein the resolved shear stress τ acting on the primary slip system attains a constant value τ_s.

The saturation stress-strain curve of a crystal is conventionally defined as the relation between the plastic slip-strain amplitude γ_{pl} and the saturation resolved shear

stress τ_s. In Fig. 2.2.1 [Mug78], Mughrabi shows the saturation stress-strain curve of a copper single-crystal specimen. Three well-differentiated stages may be identified in this curve. In the first stage, $\gamma_{pl} < 7\times10^{-5}$, τ_s is a monotonically increasing function of γ_{pl}. The deformation in this stage is fairly uniform over the specimen, and no signs of strain localization are as yet evident. Dislocations are predominantly of edge character and collected in veins of high dislocation density separated by channels containing comparatively low densities of screw dislocations ([BKB80]; [Sur91]); see Fig. 2.2.1. The dislocations in the veins form dense multipoles of zero net Burgers vector and, consequently, do not result in long-range stresses [Mug80]. The mean dislocation density in the veins is of the order of 10^{15} m^{-2} and three orders of magnitude lower in the channels. Veins are roughly 1.5μm wide and can fill up to 50% of the material [Woo73]. The saturation stage is characterized by the ability of the back and forth motion of the dislocations in the veins to accommodate the deformation ([Fel65]; [FL75]; [GM75]; [KW79]). This flip-flop mechanism can accommodate plastic strains up to 10^{-4}. No fatigue cracks are observed in the first stage of the saturation stress-strain curve, which strongly suggests that strain localization is a prerequisite for crack nucleation ([Lai76]; [BM65]).

The second stage of the saturation stress-strain curve, $\gamma_{pl,M} \approx 7 \times 10^{-5} < \gamma_{pl} < \gamma_{pl,PSB} \approx 7 \times 10^{-3}$, exhibits a plateau wherein τ_s is ostensibly independent of γ_{pl}. The deformation in the specimen ceases to be uniform and localizes to narrow bands of intense deformation, or persistent slip bands (PSB). The volume of PSBs is a monotonically increasing function of γ_{pl}. Assuming that the matrix can accommodate a maximum slip strain $\gamma_{pl,M}$ independent of γ_{pl} and that each PSB can carry a fixed amount of slip, the slip-strain amplitude is related to the volume fraction f of PSBs through the law of mixtures [Win74]

$$\gamma_{pl} = f\,\gamma_{pl,PSB} + (1-f)\,\gamma_{pl,M} \tag{2.1}$$

where $\gamma_{pl,PSB}$ is the slip strain at $f = 1$, corresponding to the end of the second stage of the saturation stress-strain curve. The PSBs cross the entire crystal and

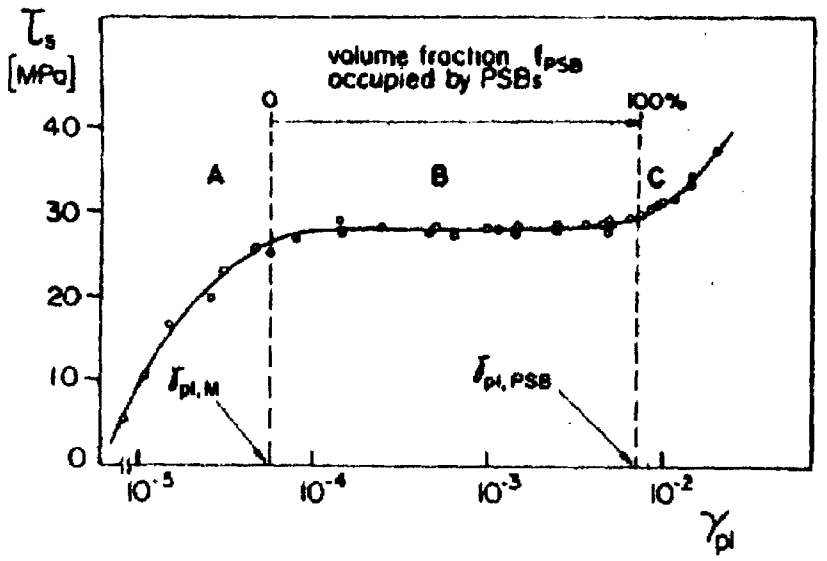

Figure 2.1: Saturation stress-strain curve (CSSC) of a copper single-crystal specimen [Mug78].

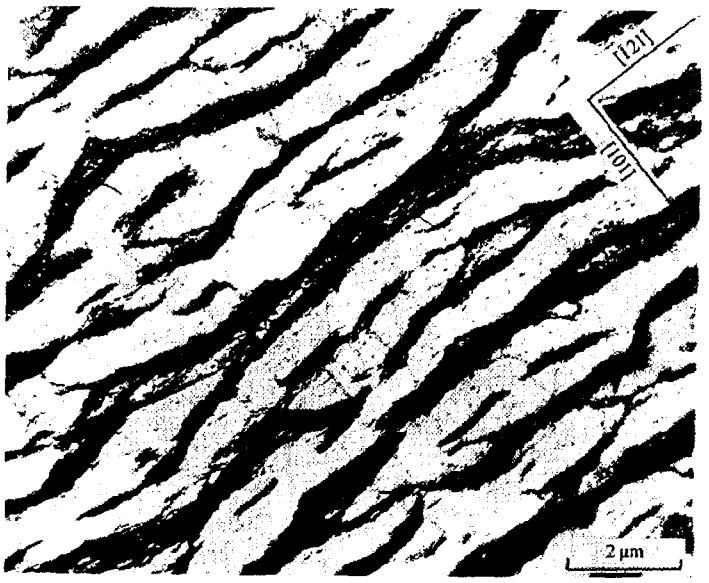

Figure 2.2: Matrix vein structure in a single crystal of copper fatigued to saturation at 77.4 K. The primary glide plane coincides with the plane of the figure and the Burgers vector with the [101] direction [BKB80].

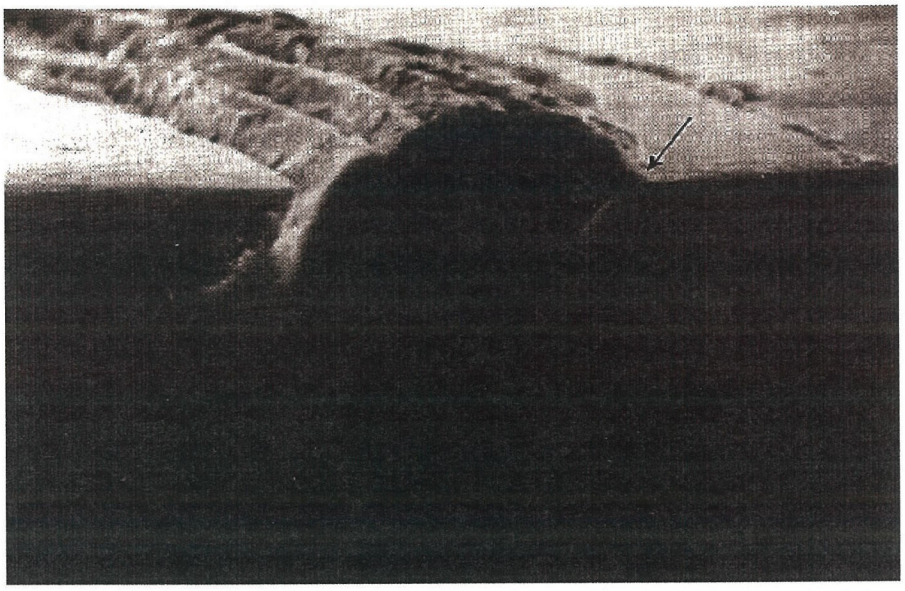

Figure 2.3: Fatigue crack initiation at a PSB-matrix interface in a copper crystal fatigued for 60,000 cycles at $\gamma_{pl} = 0.002$ and room temperature, [ML89b].

intersect the surfaces, where they give rise to surface roughness [ML89b]. After a sufficient number of cycles, fine surface cracks are observed to appear at the matrix-PSB interface ([EH03]; [Gou33]; [ML89b]; [Sur91]); Fig. 2.2.1. These and similar observations suggest that fatigue-crack initiation is mediated by PSB formation and surface roughening.

The dislocation structures found in the PSBs differ markedly from those in the matrix ([MAH79]; [Sur91]); see Fig. 2.2.1. PSBs are characterized by dense walls of edge dislocations oriented in the direction of the deformation. These walls are separated by channels containing comparatively low densities of screw segments. The walls occupy about 10% of the volume of the PSBs, are $0.03 - 0.25\mu m$ thick and roughly $1.3\mu m$ apart. The dislocation density within the PSBs remains roughly constant owing to a dynamic equilibrium between dislocation multiplication and annihilation. About two thirds of the dipoles in the walls are of vacancy type and the remaining one third are of interstitial type ([ABW76]; [AW76]). The deformation in the PSB is carried by dislocation loops which bow out of their walls and jump across the adjacent channel. As a loop bows out, it forms two kinks of screw character which sweep the length of

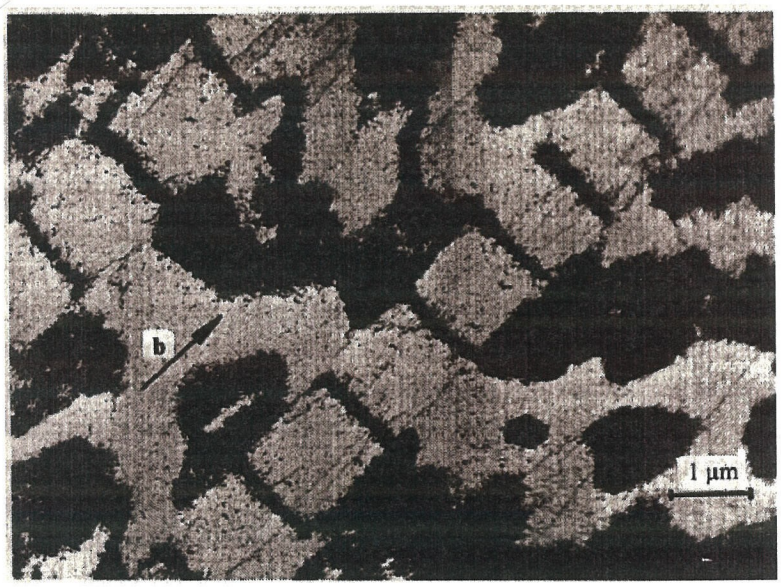

Figure 2.4: Ladder structure of PSBs in a copper crystal fatigued at $\gamma_{pl} = 1 \times 10^{-3}$ and room temperature [MAH79].

the channel. When a bowing dislocation loop impinges upon a neighboring wall, it may activate the emission of a new loop, which results in a snowballing effect. The main deformation mechanism in the matrix is the flip-flop motion of dislocation pairs within the veins.

The formation of PSBs is a poorly-understood phenomenon. Kuhlmann-Wilsdorf and Laird [KWL80] have proposed that PSBs are formed from the veins by the activation of a second slip system that causes massive dislocation annihilation and redistribution. Other authors ([WA85]; [Aif87]; [GLL95]) have suggested that PSBs are the net result of a process of patterning governed by a reaction-diffusion equation. Yet other authors [DBL86] and [DHL86] have proposed that the wall structures arise as energy minimizers.

In the third stage of the saturation stress-strain curve, $\gamma_{pl,PSB} < \gamma_{pl}$, τ_s is once again an increasing function of γ_{pl}. This stage is characterized by the activation of a secondary slip system at the PSB/matrix interface and the subsequent formation of cell and labyrinth dislocation structures ([AKLM84]; [Sur91]); see Fig. 2.2.1.

Figure 2.5: Labyrinth structure in a copper single crystal cycled to saturation at $\gamma_{pl} = 5 \times 10^{-3}$, [AKLM84].

2.2.2 Surface roughness and crack nucleation

The irreversibility of slip within the PSBs results in the roughening of the crystal surface. This surface roughening manifests itself in two forms: a) extrusions and intrusions, at sites where PSB emerge into the surface, with wave length of the order of the width of the PSB ([ML89a]; [DEM86]; [Sur91]); see Figs. 2.2.2 and 2.2.2; b) a roughness of shorter wave length than the protrusions caused by the randomness of the slip activity.

The interface between the PSBs and the matrix are preferential sites for the nucleation of cracks ([ML89a]; [ML89b]; [HN86]; [Hem59]; [HD78]; [BM65]; [ABW76]; [EGM81]; [ML89b]; [TWL56]; [NVF77]); see Figs. 2.2.2 and 2.2.1. The importance of surface roughness as regards fatigue crack initiation was unambiguously established by Basinski *et al.* [BPB83], who showed that the fatigue life of the specimen could be prolonged by electropolishing of the surfaces during test interruptions.

A number of theories ([FL75]; [Woo58]; [May60]; [DEM86]) and mechanistic models ([TM81]; [MN90]; [VCNM90]; [Lin92]) of the surface roughening phenomenon have been proposed. It is by now well established that surface roughness first appears when

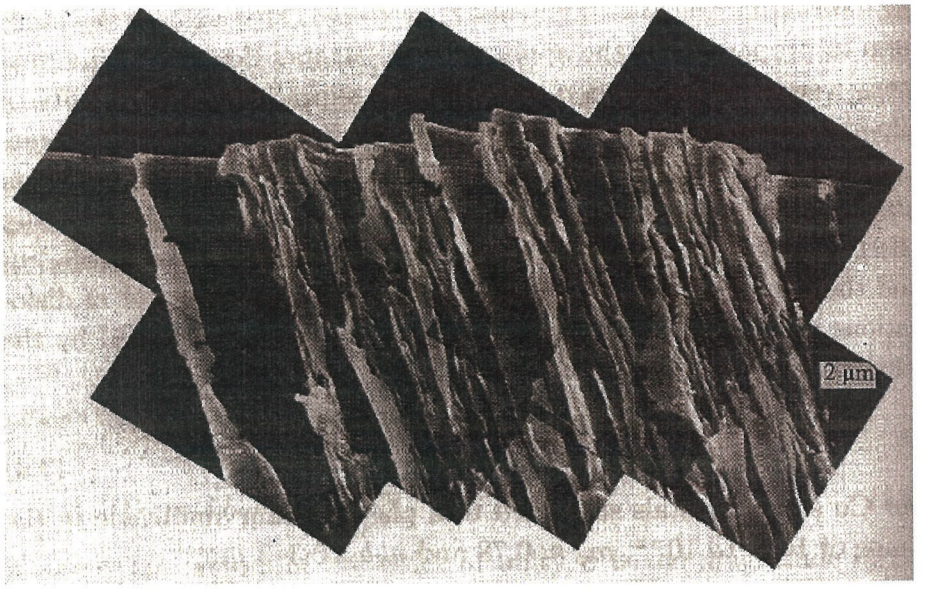

Figure 2.6: Protrusions on the surface of a copper crystal fatigue at room temperature for 1.2×10^5 cycles at $\gamma_{pl} = 2 \times 10^{-3}$, [ML89a].

Figure 2.7: PSB protrusion profile in a copper crystal [DEM86].

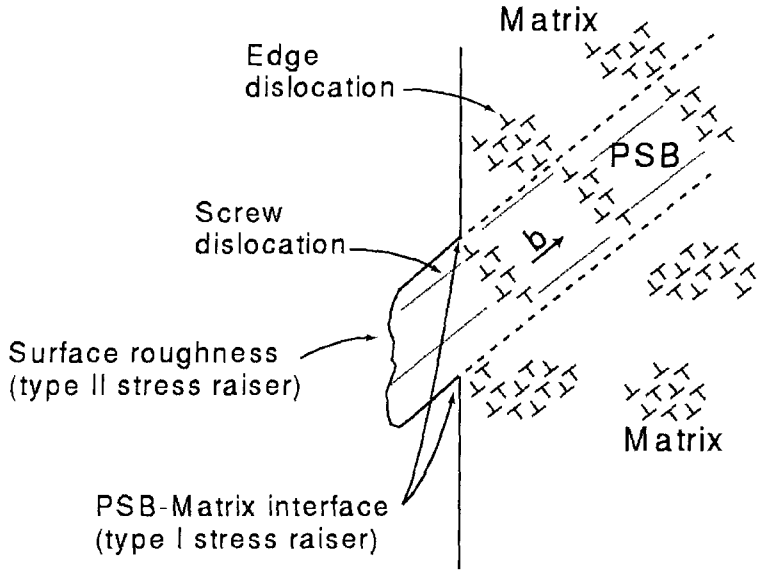

Figure 2.8: PSB and matrix dislocation structure and stress raiser sites.

the mean dislocation distance approaches the annihilation distance. Thus, a dipole consisting of edge dislocations in copper will annihilate to form a vacancy or an interstitial if the spacing of the dislocations becomes smaller than about 1.6 nm [EGM81]. The majority of the dislocation dipoles which are annihilated during fatigue are of the vacancy type [ABW76], leading to a substantial increase in the vacancy concentration. Using electrical conductivity techniques, Johnson and Johnson [JJ65] and Polák [Pol70] measured vacancy concentrations of the order of 10^{-4} in fatigued metals.

Differt, Essmann and Mughrabi [DEM86] have modelled the short wave roughness by randombly irreversible slip process caused by the production and annihilation of screw dislocation. This process could be able to produce the observed hills and valleys.

Essmann, Gösele and Mughrabi [EGM81] have developed a model of surface extrusion and fatigue crack nucleation based on the hypothesis that dislocation annihilation within the PSBs, and the attendant vacancy generation, are the origin of slip irreversibility. The PSB is loaded with a non-cycling compression in this model [BO85]. Driven by the concentration differential between PSBs and matrix, vacancies diffuse from the PSBs into the matrix ([Han55]; [BH59]; [JD66]; [RH66]). Voids formed by vacancy aggregation can grow at the interface between the PSB and the matrix, es-

pecially near the surface where entrapped gas can render the voids stable ([Mug81]; [KB78]). Void nucleation and growth are known to constitute a mechanism of ductile crack growth in single crystals ([LW75]; [Wil82]). Antonopouluos *et al.* [ABW76] introduced an alternative model in which the PSBs are loaded in tension due to the generation of vacancy dipoles, a mechanism which is also responsible for surface roughening. Possible ways to reconcile the models of Essmann *et al.* [EGM81] and Antonopouluos *et al.* [ABW76] have been discussed by Brown and Ogin in [BO85].

2.3 Constitutive behavior

In order to follow the processes of deformation leading to the nucleation of a fatigue crack, constitutive models of the inelastic behavior of the PSBs are required. In this paper, we focus on the response of a fatigued single crystal at saturation, and, consequently, we shall not concern ourselves with the transient preceding saturation. In most cases of interest, this transient constitutes a small portion of the fatigue life of the specimen and can, therefore, be neglected to a first approximation.

As noted earlier, the main deformation mechanisms operating in the matrix at saturation are the motion of screw segments in the channels and the flip-flop of dislocation pairs in the veins. This latter effect has been modeled by idealizing the veins as Taylor dislocation lattices ([KW79]; [CL81]). Because dislocation motion in the veins is reversible at saturation, its effect can be understood as an effective reduction in the shear modulus of the crystal. Under the conditions of interest here this reduction will be neglected to a first approximation. Likewise, following Winter [Win74], Brown and Ogin [BO85], we shall assume that most of the slip strain is carried by the PSBs, and will simply treat the matrix as elastic.

Next, we turn to the inelastic behavior of the PSBs. Away from free surfaces and grain boundaries, plastic deformation in the PSBs occurs predominantly by single slip. The dislocations in the primary slip system adopt the characteristic ladder structure alluded to in Section 2.2.1. By contrast, multiple slip inevitably occurs at the intersection between a PSB and, e.g., a free surface. Therefore, modeling of these regions

necessitates constitutive descriptions which account for multiple slip. To this end, we have adapted a micromechanical theory of slip in F.C.C. single crystals proposed by Ortiz and Popov [OP82] and further developed by Cuitiño and Ortiz [CnO92], by explicitly accounting for the ladder structure of PSBs and the Bauschinger effect.

Under the conditions envisioned here, the total deformation of the crystal is the result of three main mechanisms: lattice distortion; dislocation motion within the active slip systems; and vacancy generation. Mathematically, this suggests a multiplicative decomposition

$$\mathbf{F} = \mathbf{F}^e \mathbf{F}^p \mathbf{F}^v \tag{2.2}$$

of the deformation gradient $\mathbf{F}$ into: a factor $\mathbf{F}^v$ which represents the effect of vacancy generation; a plastic part $\mathbf{F}^p$, defined as the cumulative effect of dislocation motion; and an elastic part $\mathbf{F}^e$, which describes the distortion of the lattice. Eq. (2.2) generalizes the conventional multiplicative kinematics of Lee [Lee69]. Following Teodosiu [Teo69] and others ([AR77]; [Hav73]; [HR72]; [Man72]; [Ric71]) we shall assume that $\mathbf{F}^p$ leaves the crystal lattice not only essentially undistorted, but also unrotated. Thus, the rotation of the lattice is contained in $\mathbf{F}^e$. In this section we begin by considering pure slip processes and defer consideration of the vacancy generation mechanism until Section 2.3.3.

Stresses in the crystal are induced by the lattice distortions described by $\mathbf{F}^e$. One might express this connection by, for instance, postulating a relation $\boldsymbol{\tau}(\mathbf{F}^e)$ between the Kirchhoff stress tensor $\boldsymbol{\tau}$ and $\mathbf{F}^e$. A standard exercise shows that the most general form of this relation consistent with the principle of material frame indifference is

$$\bar{\mathbf{S}} = \bar{\mathbf{S}}(\bar{\mathbf{C}}^e) \tag{2.3}$$

where $\bar{\mathbf{S}} = \mathbf{F}^{e-1}\boldsymbol{\tau}\mathbf{F}^{e-T}$ is a symmetric second Piola-Kirchhoff stress tensor relative to the crystal lattice, and $\bar{\mathbf{C}}^e = \mathbf{F}^{eT}\mathbf{F}^e$ is the elastic right Cauchy-Green deformation tensor. For most applications involving metals, a linear–albeit anisotropic–relation

between $\bar{\mathbf{S}}$ and the elastic lagrangean strain $\bar{\mathbf{E}}^e = (\bar{\mathbf{C}}^e - \mathbf{I})/2$ can be assumed without much loss of generality. Higher-order elastic moduli have been given by Teodosiu [Teo82].

From the kinematics of dislocation motion, Rice [Ric71] derived the flow rule

$$\dot{\mathbf{F}}^p \mathbf{F}^{p-1} \equiv \bar{\mathbf{L}}^p = \sum_\alpha \dot{\gamma}^\alpha \bar{\mathbf{s}}^\alpha \otimes \bar{\mathbf{m}}^\alpha \tag{2.4}$$

where $\dot{\gamma}^\alpha$ is the shear strain rate on system α and $\bar{\mathbf{s}}^\alpha$ and $\bar{\mathbf{m}}^\alpha$ are the corresponding slip direction and slip plane normal. In FCC crystals, the potentially active slip systems are the 12 octahedral systems belonging to the family of $\{111\}$ planes and $[\bar{1}10]$ directions. We adopt throughout the convention of differentiating between the positive and negative slip directions $\pm\bar{\mathbf{m}}^\alpha$ for each slip system, whereupon the slip rates $\dot{\gamma}^\alpha$ can be constrained to be nonnegative.

A simple calculation shows that the stress measure conjugate to γ^α is the resolved shear stress τ^α acting on the plane of normal $\bar{\mathbf{m}}^\alpha$ in the direction $\bar{\mathbf{s}}^\alpha$. The resolved shear stress follows from, e.g., the Kirchhoff stress tensor $\boldsymbol{\tau}$ through the relation

$$\tau^\alpha = \mathbf{s}^{\alpha T} \boldsymbol{\tau} \mathbf{m}^\alpha \tag{2.5}$$

where one defines $\mathbf{s}^\alpha = \mathbf{F}^e \bar{\mathbf{s}}^\alpha$ and $\mathbf{m}^\alpha = \mathbf{F}^{e-T} \bar{\mathbf{m}}^\alpha$. In view of the work conjugacy of the variables τ^α and γ^α, it is possible to interpret the resolved shear stress τ^α as the driving force for the slip strain rate $\dot{\gamma}^\alpha$.

To render the preceding constitutive relations complete, an equation of evolution for γ^α needs to be formulated. For definiteness, we shall restrict our discussion to the case of fully reversed, constant plastic-strain amplitude loading histories, and to rate-independent plasticity. Rate effects, which can be non-negligible for very high-frequency loading, may be built into the formulation by recourse to a viscosity law (see, e.g., [CnO92]). In keeping with our focus on saturation, we shall assume the dislocation densities in all slip systems to remain constant. Extensions of the model to account for dislocation multiplication and annihilation may be found elsewhere

(see, e.g., [CnO92]).

2.3.1 Loading

Each active system in the crystal, say system α, yields during the course of one half of every cycle, with the opposite system $-\bar{\mathbf{m}}^{\alpha}$ taking up the remaining half. During loading, the motion of dislocations within an active system α is driven by the resolved shear stress τ^{α} and is resisted by obstacles. There are two main sources of obstacles to be considered, both of which contribute to the hardening of the crystal: forest dislocations and the mutual trapping of edge dislocations in PSB walls. The primary slip system within the PSBs hardens almost exclusively by the trapping mechanism, as the dislocation densities in the secondary systems are too low for forest hardening to be of significance. By contrast, secondary systems, such as are activated at the free surface/PSB intersection, lack a self-organized ladder structure and are subject to forest hardening only. These hardening mechanisms are next considered in turn.

Trapping hardening in PSBs

Consider the primary slip system within a fully developed PSB. The main obstacle to dislocation motion in the ladder structure is the mutual trapping of edge dislocations of opposite sign. Let s denote the strength of the bond between a dislocation and the wall which contains it. Alternatively, s is the critical value of the resolved shear stress required for the dislocation to break loose from the wall. Since the arrangement of dislocations within a wall is, to some extent, random, it follows that s itself is a random variable. Let $\tilde{f}(s)$ denote the probability density of bond strengths s in a wall structure under zero resolved shear stress. Thus, $\tilde{f}(s)ds$ is the fraction of bond strengths in the interval $(s, s+ds)$ in an unstressed dislocation wall.

Next, consider a process of monotonic loading of the slip system under consideration. The assumption of rate-independent behavior requires that all dislocations occupy stable positions throughout the loading process. In particular, if the load is held fixed, no dislocation motion and, correspondingly, no slip strain, should ensue.

Let $f(s)$ denote the probability density of bond strengths in the wall after the resolved shear stress has been increased monotonically to τ. Evidently, for all dislocations to be stable at this stage, all bonds must have a strength $s \geq \tau$, i. e., $f(s) \equiv 0$ in the interval $0 \leq s \leq \tau$.

Imagine now that the resolved shear stress is further increased from τ to $\tau + d\tau$. Evidently, this causes a fraction $f(\tau)d\tau$ of the dislocation density to become unstable, break free from their respective walls and jump to neighboring walls. Under the assumption of rate-independent behavior, these jumps occur instantaneously. A subfraction $(1 - \tilde{P}(\tau))$ of the destabilized dislocations will be trapped by the nearest wall after one single jump, while the remainder will proceed beyond. Of these, again a subfraction $(1 - \tilde{P}(\tau))$ will be trapped at the second wall, while the remainder will proceed beyond, and so on. The average number of jumps taken by a dislocation before it is trapped at a stable position is, therefore,

$$\begin{aligned} \bar{N} &= (1 - \tilde{P}(\tau)) + 2\tilde{P}(\tau)(1 - \tilde{P}(\tau)) + 3\tilde{P}(\tau)^2(1 - \tilde{P}(\tau)) + \dots \\ &= \frac{1}{(1 - \tilde{P}(\tau))}. \end{aligned} \tag{2.6}$$

Mobile dislocations need not physically cross walls in order to effect multiple jumps. It suffices that, when a dislocation impinges upon a wall, it destabilizes a dislocation segment on the opposite side, which then proceeds through the next channel.

Evidently, the probability that one of the destabilized dislocations forms a stable bond of strength s after its flight is $\tilde{f}(s)$. The function $f(s)$ has to be adjusted to reflect these newly created bonds and for the fact that $f(s)$ must vanish over the extended interval $0 \leq s \leq \tau + d\tau$. An analytical treatment of this problem has been given by Cuitiño and Ortiz [CnO93] within the statistical mechanical framework proposed by Ortiz and Popov [OP82], who derived a kinetic equation governing the evolution of $f(s)$ using standard tools of nonequilibrium statistical mechanics. Cuitiño and Ortiz [CnO92] obtained analytical solutions of the kinetic equation for the case of monotonic loading and an arbitrary time variation of the density of point obstacles.

The solution is

$$f(s) = \frac{\tilde{f}(s)\ H(s-\tau)}{1-\tilde{P}(\tau)} \tag{2.7}$$

where $H(x)$ is the Heaviside step function. We verify that $f(s) = 0$ for $s \leq \tau$, as required.

The hardening law follows from the preceding results and standard relations from dislocation mechanics. The incremental slip strain may be written in the form

$$d\gamma = b\, d\rho\, \bar{L} \tag{2.8}$$

where $d\rho$ is the fraction of dislocations which are destabilized by the load increment, b is the magnitude of the Burgers vector and $\bar{L}$ is mean free flight distance of the dislocations. By virtue of the preceding results, one has

$$d\rho = \rho f(\tau) d\tau = \rho \frac{\tilde{f}(\tau)}{1-\tilde{P}(\tau)} d\tau \tag{2.9}$$

where ρ is the dislocation density in the primary system and

$$\bar{L} = \bar{N} w = \frac{w}{(1-\tilde{P}(\tau))} \tag{2.10}$$

where w is the separation between walls. Inserting (2.9) and (2.10) into (2.8) yields

$$d\gamma = h(\tau)\ d\tau \tag{2.11}$$

where

$$h(\tau) = b\rho w \frac{\tilde{f}(\tau)}{(1-\tilde{P}(\tau))^2} \tag{2.12}$$

is the sought plastic hardening modulus due to trapping.

In order to have an explicit expression for the hardening relations, the unstressed bond strength probability $\tilde{f}(s)$ needs to be identified. To aid in this identification,

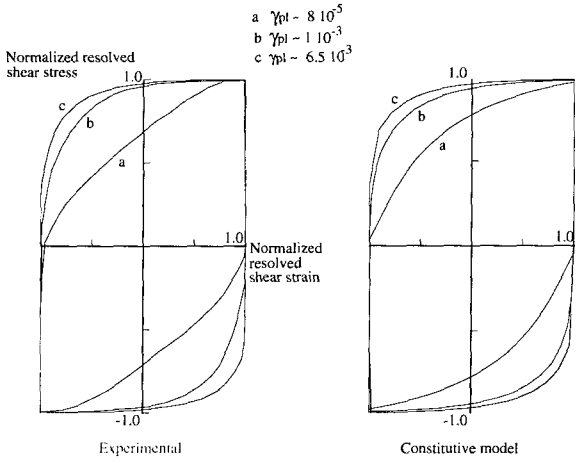

Figure 2.9: Comparison between experimental [Mug78] and theoretical hysteresis loops at saturation for different values of γ_{pl}.

eq. (2.11) may be integrated, with the result

$$\gamma(\tau) = b\rho w(\frac{1}{1-\tilde{P}(\tau)} - 1). \tag{2.13}$$

This relation permits the direct identification of $\tilde{P}(\tau)$ from an experimentally measured hysteresis loop $\gamma(\tau)$. From Mughrabi's data in Fig. 10, page 213 of [Mug78], we have found that $\tilde{f}(\tau)$ is well-approximated by the beta distribution

$$\tilde{f}(s) = \frac{1}{\tau_s}\frac{(s/\tau_s)^{p-1}(1-s/\tau_s)^{q-1}}{B(p,q)}, \tag{2.14}$$

where $B(p,q)$ is the beta function and τ_s is the saturation stress which depends on temperature (Table 2.1 of ref. [Sur91]). A choice of parameters which fits well Mughrabi's data is $p = 20$, $q = 1.03$. A comparison between simulated and experimental hysteresis loops for a copper single crystal fatigued to saturation is shown in Fig. 2.3.1. As may be seen from the figure, the predicted hysteresis loops are in good agreement with observation.

Forest hardening

At the intersection between the PSB and the free surface, a complex pattern of deformation arises which cannot be accommodated by single slip, and multiple slip ensues. The highly self-organized ladder dislocation structure cannot be assumed to develop in the secondary systems. Instead, we shall presume that hardening in these systems occurs by the forest dislocation mechanism, i.e., that dislocations piercing the slip plane, or forest dislocations, constitute the principal source of obstacles to the motion of dislocations. Detailed numerical simulations of a dislocation line propagating through a random array of point obstacles have been carried out by Foreman and Makin ([FM66]; [FM67]), and by Kocks [Koc66]. In Kocks' model, all obstacles opposing the motion of the dislocation line are idealized as pinning points. Pairs of such points arrest dislocations, which require a certain threshold resolved shear stress s to overcome the barrier. For a given temperature, s can be estimated from a line tension calculation (see, e.g., the review of [KZ73]). The simplest such estimate gives $s = \alpha\mu b/l$, where μ is the shear modulus, b, the length of the Burgers vector, l, the distance between pinning points, and α is a temperature-dependent coefficient of the order of 0.3.

The motion of the dislocations through a random distribution of obstacles obeys a kinetic equation which was derived by Ortiz and Popov [OP82] using standard tools of nonequilibrium statistical mechanics. Cuitiño and Ortiz [CnO92] obtained analytical solutions of the governing kinetic equation which determine the analytical form of the hardening law. For randomly distributed obstacles in the slip plane, the result is (see [CnO92])

$$\dot{\gamma}^\alpha = \frac{\dot{\tau}^\alpha}{h^{\alpha\alpha}}, \qquad h^{\alpha\alpha} = h_c^{\alpha\alpha}\left(\frac{\tau^\alpha}{\tau_c^\alpha}\right)^3\left\{\cosh\left[\left(\frac{\tau_c^\alpha}{\tau^\alpha}\right)^2\right]-1\right\},$$
$$h_c^\alpha = \frac{\tau_c^\alpha}{\gamma_c^\alpha}, \qquad \tau_c^\alpha \equiv C\mu b\sqrt{\pi n^\alpha}, \qquad \gamma_c^\alpha \equiv \frac{b\rho^\alpha}{2\sqrt{n^\alpha}}, \tag{2.15}$$

where n^α is the density of point obstacles, ρ^α is the dislocation density, $h^{\alpha\alpha}$ is the self-hardening modulus, τ_c^α is a characteristic or 'flow' stress, γ_c^α is a characteristic slip

strain, and h_c^α is a characteristic hardening modulus. In keeping with our focus on the saturation stress-strain behavior of fatigued single crystals, we presume all dislocation densities ρ^α to remain constant throughout. The values of τ_c^α and γ_c^α determine the location of the 'bend' in the resolved shear stress-slip strain curve. In particular, τ_c^α correlates with the value of the flow stress determined by back-extrapolation. As is evident from (2.15), τ_c^α and γ_c^α are a function of the dislocation density ρ^α and the density n^α of point obstacles in the slip plane.

The hardening matrix predicted by the above dislocation model is diagonal, and, consequently, the hardening law (2.15) conforms to the general structure suggested by Bassani and Wu ([BW91a]; [BW91b]) on the basis of their experimental data. The precise manner in which the dislocation model accounts for latent hardening effects in high-purity FCC metals has been extensively discussed by Cuitiño and Ortiz [CnO93]. Detailed comparisons demonstrating good agreement between the predictions of the theory and stress-strain and latent-hardening data have also been given by Cuitiño and Ortiz [CnO93].

A key variable in the description of the forest hardening is the density n^α of point obstacles afforded by forest dislocations. Evidently, n^α is a function of the dislocation densities in all remaining systems. The experimental work of Franciosi and co-workers ([FBZ80]; [FZ82]; [FZ83]; [Fra85b]; [Fra85a]; [Fra88]) is suggestive of a dependence of the form

$$n^\alpha = \sum_\beta a^{\alpha\beta} \rho^\beta. \tag{2.16}$$

Experimentally determined values of the interaction matrix $a^{\alpha\beta}$ have been given by Franciosi and Zaoui [FZ82] for the 12 slip systems belonging to the family of $\{111\}$ planes and $[110]$ directions in FCC crystals, and by Franciosi [FZ83] for the 24 systems of types $\{211\}$ $[111]$ and $\{110\}$ $[111]$ in B.C.C. crystals. They classify the interactions according to whether the dislocations belong to the same system (interaction coefficient a_0), fail to form junctions (interaction coefficient a_1), form Hirth locks (interaction coefficient a_1), co-planar junctions (interaction coefficient a_1), glis-

sile junctions (interaction coefficient a_2), or sessile Lomer-Cottrell locks (interaction coefficient a_3), with $a_0 \leq a_1 \leq a_2 \leq a_3$. Franciosi has also found the interaction coefficients to be linearly dependent on the stacking fault energy of the crystal, the degree of anisotropy increasing with decreasing stacking fault energy.

In regions of multiple slip of the PSB, the trapping and forest hardening mechanisms operate concurrently on the primary system. For simplicity, in calculations we have assumed that the combined hardening matrix $h^{\alpha\beta}$ can be approximated as the sum of the hardening matrices due to trapping and forest hardening. It bears emphasis that, since the dislocation density in the secondary systems is orders of magnitude lower than in the primary system, the overwhelmingly dominant hardening mechanism in the primary system is trapping. Conversely, the high dislocation density in the primary system hardens greatly the secondary systems through the forest mechanism, with the result that secondary slip can only be activated in regions of stress concentration such as the junctures between PSB boundaries and the free surface.

2.3.2 Unloading and the Bauschinger effect

The Bauschinger effect refers to the experimental observation that, after a certain amount of plastic deformation, the material yields at a reduced stress when the direction of loading is reversed. The Bauschinger effect was modeled within the context of the forest theory of hardening by Ortiz and Popov [OP82]. After a process of monotonic loading up to a resolved shear stress τ, the probability density $f(s)$ of obstacle strengths s faced by the dislocations in the slip system under consideration is given by (2.7). In particular, for quasi-static loading leading to rate-independent behavior, all dislocations in the system must be pinned by obstacles of strength $s \geq \tau$. Ortiz and Popov [OP82] argued that reversed slip gradually causes this dislocation/obstacle arrangement to dissolve, with the result that $f(s)$ approaches the virgin distribution $\tilde{f}(s)$ when the reverse slip strain γ greatly exceeds a characteristic slip strain γ_c. Thus, after sufficient reverse slip, a process of reloading ostensibly gives rise to the

virgin stress-strain curve once again, in keeping with the observed Bauschinger effect.

Ortiz and Popov [OP82] derived a kinetic equation governing the transition of $f(s)$ towards $\tilde{f}(s)$ brought about by reverse slip. However, a computationally more convenient means of modeling the transition is to simply assume that $f(s)$ remains of the form

$$f(s) = \frac{\tilde{f}(s)\ H(s-\tau_0)}{1-\tilde{P}(\tau_0)} \tag{2.17}$$

where τ_0 is the critical resolved shear stress for re-loading. In this manner, the hardening moduli derived in Sections 2.3.1 and 2.3.1 retain their validity upon re-loading. Clearly, at the onset of reverse slip, τ_0 should be set to the maximum resolved shear stress $\tau_{\max}$ attained during loading. Conversely, for sufficiently large reverse slip, τ_0 should tend to zero. The law of evolution of τ_0 with γ can be derived from the kinetic equation of Ortiz and Popov [OP82]; see Appendix I. The result is

$$\tilde{P}(\tau_0) = \frac{\tilde{P}(\tau_{\max})\mathrm{e}^{-\gamma/\gamma_c}}{1+\tilde{P}(\tau_{\max})(\mathrm{e}^{-\gamma/\gamma_c}-1)}. \tag{2.18}$$

Evidently, when $\gamma = 0$ this equation returns $\tau_0 = \tau_{\max}$, whereas for $\gamma/\gamma_c \gg 1$ the same equation gives $\tau_0 \to 0$, as required. Upon reloading, the system remains elastic while $\tau < \tau_0$ and slip begins when $\tau \geq \tau_0$. Following the onset of slip, hardening is taken to be governed by the hardening laws derived in Sections 2.3.1 and 2.3.1.

2.3.3 Vacancy generation and volumetric expansion

During saturation, the dislocation density in the PSB remains constant, at roughly $\rho_w \approx 6\times 10^{15} m^{-2}$, by virtue of the establishment of a dynamical equilibrium between multiplication and annihilation. Annihilation occurs when two edge segments of opposite sign get closer than a critical distance $y_e \approx 1.6$ nm. As noted in Section 2.2, most dipoles observed in PSBs are of the vacancy type. Indeed, dislocation annihilation is thought to be the principal source of vacancies in the PSBs. Another effect of dislocation annihilation is a steady elongation of the PSBs, which is ultimately

responsible for the formation of surface protrusions. In this section, we formulate simple relations quantifying these two effects, namely, vacancy generation and PSB elongation.

If single slip were the sole deformation mechanism, PSBs would merely shear back and forth and no elongation of the slip plane would be kinematically possible. Discounting the activation of a secondary slip system, it is clear that the elongation of the PSBs in the direction of the nominal slip plane must necessarily involve *climb* as well as slip. Dislocation climb is not conservative and gives rise to point defects such as vacancies. Consequently, PSB elongation and vacancy generation are necessarily simultaneous. However, it should be carefully noted that PSB elongation is not *caused* by vacancy accumulation, as the change of volume corresponding to the saturation vacancy concentration is often much smaller than the extruded volume.

Dislocation climb takes place during pair annihilation. The geometry of the process is schematically shown in Fig. 2.3.3, which shows an elongated rectangular loop in a PSB in which the main edge segments are at the critical distance y_e for spontaneous annihilation. The length L of the loop is taken to be commensurate with the width of the specimen. The edge segments are parallel to the walls and, consequently, the Burgers vector is normal to the plane of the loop. Clearly, the mutual annihilation of the edge segments requires them to undergo climb until the area Ly of the loop reduces to zero; see Fig. 2.3.3. Denoting by b and $\bar{\mathbf{s}}$ the magnitude and direction of the Burgers vector, respectively, the rate of deformation induced by climb is

$$\dot{\mathbf{F}}^v \mathbf{F}^{v-1} = \frac{\dot{A}b}{V} \bar{\mathbf{s}} \otimes \bar{\mathbf{s}} \tag{2.19}$$

where $\dot{A}$ is the area rate swept by climbing dislocations and V is the volume of the PSB. The vacancy concentration rate induced by climb is

$$\dot{c}_v = \frac{1}{N} \frac{\dot{A}b}{\Omega} = \frac{\dot{A}b}{V} \tag{2.20}$$

where N is the number of atoms in the PSB and Ω is the atomic volume. Using this

relation, (2.19) can be recast in the form

$$\dot{\mathbf{F}}^v \mathbf{F}^{v-1} = \dot{c}_v \bar{\mathbf{s}} \otimes \bar{\mathbf{s}} \tag{2.21}$$

which gives the rate of elongation in terms of the vacancy concentration rate.

The vacancy concentration rate can be related to the rate of slip by estimating the frequency of pair annihilation events. To this end, consider an edge segment circumscribed by a circle of radius y_e, the distance for spontaneous pair annihilation. The number of dislocations of opposite sign which enter the circle in an interval of time $\triangle t$ is $\rho y_e v \triangle t$, where v is the mean dislocation velocity. The number of annihilation events per unit time is, therefore, $(n/2)\rho y_e v$, where n is the total number of edge segments of length L in the PSB. Using the relation $n = \rho V/L$, the number of annihilation events per unit time and volume is computed to be $(1/2)\rho^2 y_e v/L$. Each annihilation event generates $y_e L b/\Omega$ vacancies. Therefore, the number of vacancies generated per unit time and volume is $(1/2)\rho^2 y_e^2 b v/\Omega$, and the vacancy concentration rate is

$$\dot{c}_v = \frac{1}{2}\rho^2 y_e^2 b v. \tag{2.22}$$

Finally, using the relation $\dot{\gamma} = b\rho v$ to eliminate v gives the expression

$$\dot{c}_v = \frac{1}{2}\rho y_e^2 \dot{\gamma}. \tag{2.23}$$

This equation enables the calculation of the vacancy concentration rate when the slip rate is known. The elongation rate then follows from (2.21).

2.3.4 Vacancy diffusion and crack nucleation

The process of pair annihilation introduces a large concentration differential between PSBs and matrix. The vacancy concentration in the PSBs is also greatly in excess of the equilibrium vacancy concentration at the free surface. This induces strong

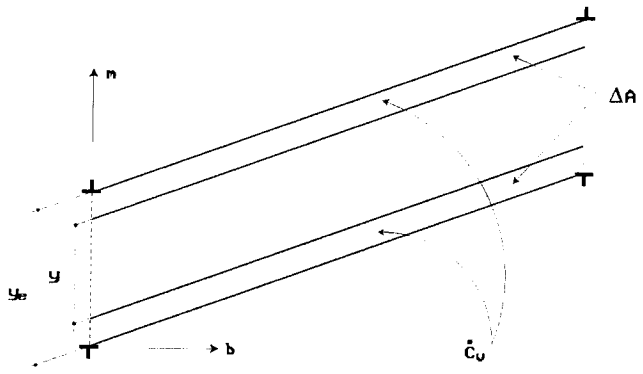

Figure 2.10: Effect of loops annihilation and vacancy generation.

concentration gradients which provide a driving force for vacancy diffusion. In addition, vacancy diffusion may be enhanced by pipe diffusion and assisted by stress concentrations at the PSB/surface interface. Due to the protracted nature of fatigue loading, diffusive mechanisms often have ample time to operate. The outward flow of vacancies causes the boundary of the crystal to change its shape. As we shall see, this effect contributes to boundary grooving and the eventual nucleation of a surface crack.

The vacancy flux through the crystal follows as [PE92]

$$\mathbf{J}_v = -\mathbf{D}\left(\nabla_0 c_v + \frac{c_v}{RT}\nabla_0 W\right) \tag{2.24}$$

where $\mathbf{D}$ is the diffusivity tensor, W is the elastic strain energy density, R is the universal gas constant, T is the absolute temperature and ∇_0 is the material gradient operator. In components, $(\nabla_0 f)_I = \partial f/\partial X_I$, where (X_1, X_2, X_3) denotes a material reference frame defined on the undeformed configuration of the crystal. Care must be exercised in properly defining material gradients due to the large deformations undergone by the crystal, e.g., within the PSB. In particular, material frame indifference is ensured by formulating the laws governing vacancy diffusion on the undeformed configuration. Stress assisted diffusion, driven by the strain energy density gradient, may be expected to be of significance at the PSB/surface interface, where stress concen-

trations arise. The evolution of vacancy concentration is governed by the continuity equation

$$\frac{\partial c_v}{\partial t} = -\nabla_0 \cdot \mathbf{J}_v + s_v \tag{2.25}$$

where s_v is the vacancy generation rate given by (2.23). Substitution of (2.25) into (2.24) gives rise to the diffusion equation

$$\frac{\partial c_v}{\partial t} = \nabla_0 \cdot \mathbf{D}\left(\nabla_0 c_v + \frac{c_v}{RT}\nabla W\right) + s_v \tag{2.26}$$

which must be satisfied throughout the undeformed configuration of the crystal. At the surface, the vacancy concentration must remain at its equilibrium value, which is given by [PE92]

$$c_{eq} = \mathrm{e}^{-\Delta G_v/kT} \tag{2.27}$$

where ΔG_v is the free energy per vacancy added to the system, k is Boltzmann's constant and T is the absolute temperature. The free energy ΔG_v and the surface energy γ may be expected to depend sensitively on the presence of impurities [RW89] and, therefore, on the environment.

Two principal mechanisms contribute to the diffusivity of vacancies in single crystals, namely, lattice diffusion and 'pipe' diffusion along dislocation lines. Assuming for simplicity parallel dislocations, the effective diffusion coefficient D in the direction of the dislocations can be estimated through the rule of mixtures [BG79]

$$D = D_{\text{lattice}} + b^2 \rho D_{\text{pipe}} \tag{2.28}$$

where ρ is the dislocation density. The activation energy for diffusion through the lattice is considerably larger than that for dislocation or pipe diffusion. Consequently, pipe diffusion dominates up to near the melting temperature, whereupon lattice diffusion becomes dominant [CF57]. In addition, Balluffi and Granato [BG79] concluded

that high-rate vacancy diffusion takes place in a narrow region surrounding the dislocation core where an appreciable positive binding energy for vacancies exists. Vacancy diffusivities are commonly measured in undeformed specimens containing low dislocation densities. Therefore, the required value of D_{pipe} can be estimated as

$$D_{\text{pipe}} = \frac{D_0}{b^2 \rho_0} \tag{2.29}$$

where D_0 is the experimentally determined diffusivity and ρ_0 is the corresponding dislocation density. Eq. (2.29) can be used to calibrate the model.

In the PSBs, the dislocations are oriented predominantly in two directions. Most dislocations are of an edge character and are parallel to the surface. However, these dislocations do not contribute to vacancy diffusion towards the matrix or the surface, and their effect can therefore be neglected in a two-dimensional model. While screw segments crossing the channels between walls are less numerous, with densities three orders of magnitude smaller than those of edge dislocations in the walls, they are, however, oriented towards the surface and, consequently, contribute significantly to boundary diffusion. Letting, as before, $\bar{s}$ be the Burgers vector direction in the undeformed configuration of the crystal, the diffusivity tensor may therefore be written as

$$\mathbf{D} = D_{\text{lattice}}\mathbf{I} + b^2 \rho_{\text{screw}} D_{\text{pipe}} \bar{\mathbf{s}} \otimes \bar{\mathbf{s}} \tag{2.30}$$

where $\mathbf{I}$ is the identity tensor. Evidently, the vacancy flux due to pipe diffusion along screw segments is unidirectional and parallel to the PSBs. Because the vacancy concentration within the PSBs is expected to be greatly in excess of the equilibrium concentration c_{eq} at the free surface, a net flux of vacancies is expected to develop towards the surface. Since pipe diffusion is relatively insensitive to temperature, this mechanism should remain operative at relatively low temperatures.

The net effect of the outward vacancy flux is to cause the surface of the crystal to recede. The inward motion of the surface is expected to be most pronounced at the

PSB/matrix interface, and thus result in groove formation. In order to compute the inward velocity of the surface, begin by writing the vacancy flux as $\mathbf{J}_v = c_v \mathbf{V}_v$, where $\mathbf{V}_v$ is the vacancy velocity relative to the undeformed configuration of the crystal. Next consider a small element of area $\triangle S_0$ on the undeformed surface of the crystal. Over a small increment of time $\triangle t$, all vacancies in the right cylinder of base $\triangle S_0$ and height $\mathbf{V}_v \cdot \mathbf{N} \triangle t$ exit though the boundary. Here $\mathbf{N}$ is the unit outward normal to $\triangle S_0$. The volume of this cylinder is $\triangle V_0 = \triangle S_0 \mathbf{V}_v \cdot \mathbf{N} \triangle t$ and, consequently, the number of vacancies which exit the crystal is $\triangle N_v = \rho_v \triangle V_0$, where $\rho_v = c_v/\Omega$ is the vacancy density, i. e., the number of vacancies per unit volume. The volume of vacancies which exit the crystal is $\triangle V_v = \Omega \triangle N_v$, and the inward velocity of the surface is $V_N = \triangle V_v/(\triangle S_0 \triangle t)$. Combining these relations finally gives

$$V_N = \mathbf{J}_v \cdot \mathbf{N} \tag{2.31}$$

It bears emphasis that V_N is a configurational velocity which expresses the rate at which the undeformed surface of crystal recedes due to the exit of vacancies. In particular, V_N should be carefully differentiated from the velocity of the material particles pertaining to the motion of the crystal.

2.4 Numerical implementation

Our finite-element implementation of the preceding theory extends the approach of Cuitiño and Ortiz ([CnO92]; [CnO96]) to account for fully-coupled vacancy diffusion. The finite deformations undergone by the crystal are followed incrementally. Equilibrium is enforced weakly at the end of each increment by recourse to the principle of virtual work, which renders the method implicit. Likewise, the stresses, plastic deformations and the hardening parameters are updated implicitly by the backward-Euler method. A particularly appealing property of implicit integration is that the finite-kinematical aspects of the calculations, such as the finite rotations undergone by the lattice, are treated exactly. The collection of active slip systems is determined itera-

tively [CnO92]. The incremental displacements are solved for via a Newton-Raphson iteration. The exact algorithmic or "consistent" tangent stiffness matrix has been derived by Cuitiño and Ortiz [CnO92]. All meshes are generated automatically by the advancing front method [PVMZ87]. Meshes are graded exponentially away from the PSB/matrix/surface junctions.

As can be expected from the subtle changes that take place with each load cycle, there are two well-differentiated time scales in the processes under consideration: i) the loading period, and ii) the characteristic time of evolution of surface protrusions. The simulation of the growth of a protrusion requires extending the calculations over many loading cycles. In principle, the incremental approach just described requires an appropriate resolution of each cycle of deformation, which would appear to render the method impractical. However, the cyclic response of the crystal, and other aspects of the solution such as the distribution of vacancy concentrations, vary slowly over many cycles of deformation. To exploit this situation, we simulate one cycle in detail and calculate the difference between the values of the field quantities at the beginning and end of the cycle. This difference is then *extrapolated* over a large number of cycles. The results of this extrapolation are then taken as initial conditions for the next direct calculation.

The coupling between diffusion and deformation is taken into account by a staggered procedure. Following one mechanical step, the rate of vacancy generation due to dislocation pair annihilation is calculated from eq. (2.23). The diffusion equation (2.26) is then solved and the vacancy concentrations updated. The finite-element treatment of the vacancy diffusion problem is based on the weak statement of the diffusion equation

$$\int_{B_0} \left[\frac{\partial c_v}{\partial t} \psi + \nabla_0 \psi \cdot \mathbf{D} \left(\nabla c_v + \frac{c_v}{RT} \nabla_0 W \right) - s_v \right] dV_0 = 0 \tag{2.32}$$

where B_0 denotes the undeformed configuration of the crystal and $\psi = 0$ on its boundary ∂B_0. Since the diffusion step is taken at fixed deformation, the elastic strain energy density W enters (2.32) as a known function of position. In order to

avoid unsymmetric terms in the diffusion equation, which complicate the formulation of finite element approximations ([BH82]; [MH85]), we introduce the integration factor $\exp(W/RT)$ leading to the alternative weak form

$$\int_{B_0} \left[e^{W/RT} \frac{\partial c_v}{\partial t} \psi + \nabla_0 \psi \cdot \left(e^{W/RT} \mathbf{D} \nabla c_v \right) - e^{W/RT} s_v \right] dV_0 = 0. \tag{2.33}$$

We discretize this equation in time using the trapezoidal rule [Hug87]. Following the update of the vacancy concentration, the motion of the referential surface of the crystal due to the outward flux of vacancies is computed from (2.31). Finally, the elongation of the PSB is determined from (2.21), which completes one application of the staggered procedure.

2.5 Numerical simulation of fatigue-crack initiation

In this section, we apply the theory developed in the foregoing to the simulation of fatigue-crack nucleation in a copper specimen subjected to fully reversed, constant strain amplitude loading. The specimen is oriented for single slip, with loading applied in the [125] direction. The principal objective of the simulation is to follow in detail the formation of surface roughness and eventual nucleation of a surface crack. Therefore, we consider a fully formed PSB and focus sharply at the intersection between the PSB and the free surface of the crystal, which is taken to coincide with the plane $(\bar{2}10)$. The crystal is assumed to undergo plane strain in the plane $(12\bar{1})$. The applied plastic strain amplitude is $\delta\epsilon_p = 6\times10^{-3}$, and the loading frequency is 0.25 Hz, which is in the bulk part of laboratory testing ([Mug78]; [BBH69]; [CL81]; [HD78]). For simplicity, we neglect the initial transient entirely and presume the PSB to be saturated from the outset. The specimen dimensions and geometry are shown in Fig. 2.5, which is not drawn to scale. We use an exponentially graded mesh to triangulate the full specimen. This is important since the elongation of the PSB scales with its length. A detail of the initial mesh in shown in Fig. 2.13. The material parameters used in

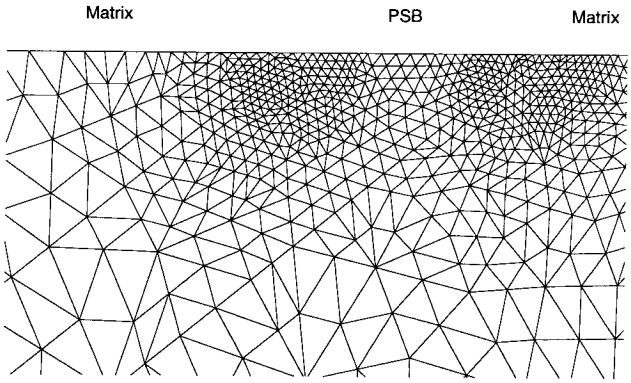

(a)

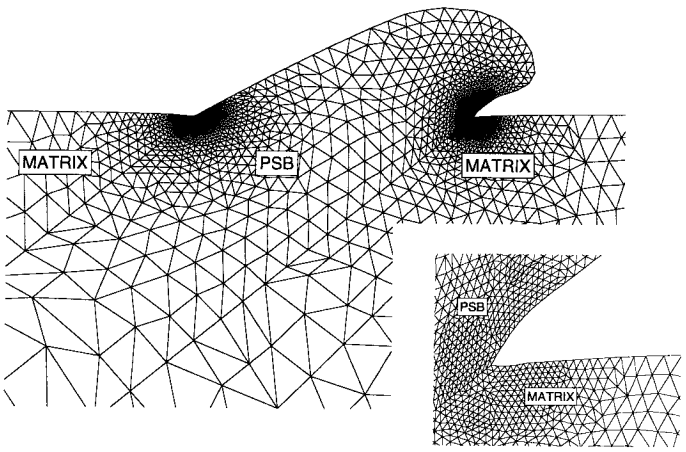

(b)

Figure 2.11: a) Mesh after 400 cycles, b) mesh after 5600 cycles.

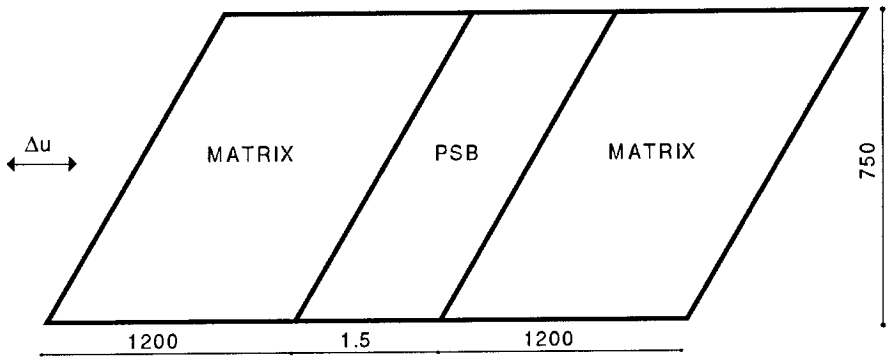

Figure 2.12: Geometry of the computational model.

$c11$	=	168.4GPa
$c12$	=	121.4GPa
$c44$	=	75.4GPa
Burgers vector b	=	0.256nm
Wall separation w	=	1.3μm
PSBdislocation density ρ	=	$4.2 \times 10^{16}\mathrm{m}^{-2}$
saturation CRSS τ_s	=	28MPa
D_{lattice}	=	$1.5 \times 10^{-15}\mathrm{m}^2/\mathrm{s}$
$D_{\text{pipe}}/D_{\text{lattice}}$	=	800

Table 2.1: Material parameters.

calculations are collected in Table 2.5 and in Cuitiño and Ortiz [CnO92].

Fig. 2.13 shows the solution after 4,800 cycles. No evidence of extrusion is as yet apparent at this stage. As expected, all fields attain nearly constant values within the PSB far away from the surface. By contrast, some incipient spatial variation is already visible near the surface. Thus, the slip activity, as measured by the effective slip strain $\dot{\epsilon}_p = \sum_\alpha \dot{\gamma}^\alpha$, exhibits maxima which alternate between both sides of the PSB. Likewise, the values of the vacancy generation rate $\dot{c}_v$, and the PSB elongation due to pair annihilation, also peak near the surface at the PSB/matrix interfaces. These trends are accentuated with the passage of time. After 45,000 cycles, a protrusion is clearly visible and the alternating character of the near-surface slip activity fields in the PSB is fully apparent, Fig. 2.5, as are the peaks in vacancy generation rate and

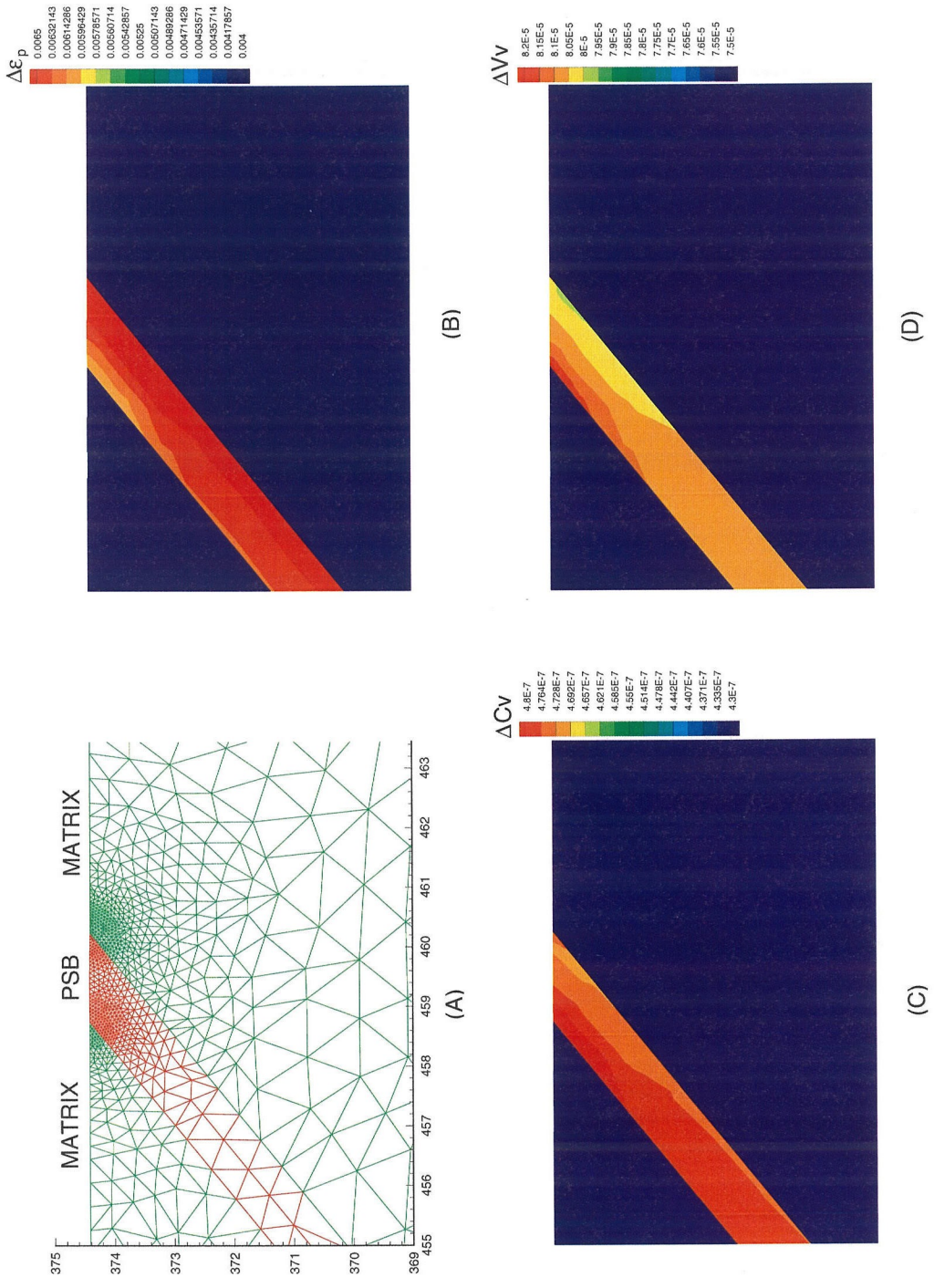

Figure 2.13: Solution after 4,800 cycles. a) Deformed mesh; b) equivalent slip strain increment ($\sum_\alpha \Delta\gamma^\alpha$); c) vacancy concentration increment; d) volume increment ($\det(\mathbf{F}^v)$). All increments correspond to the one cycle.

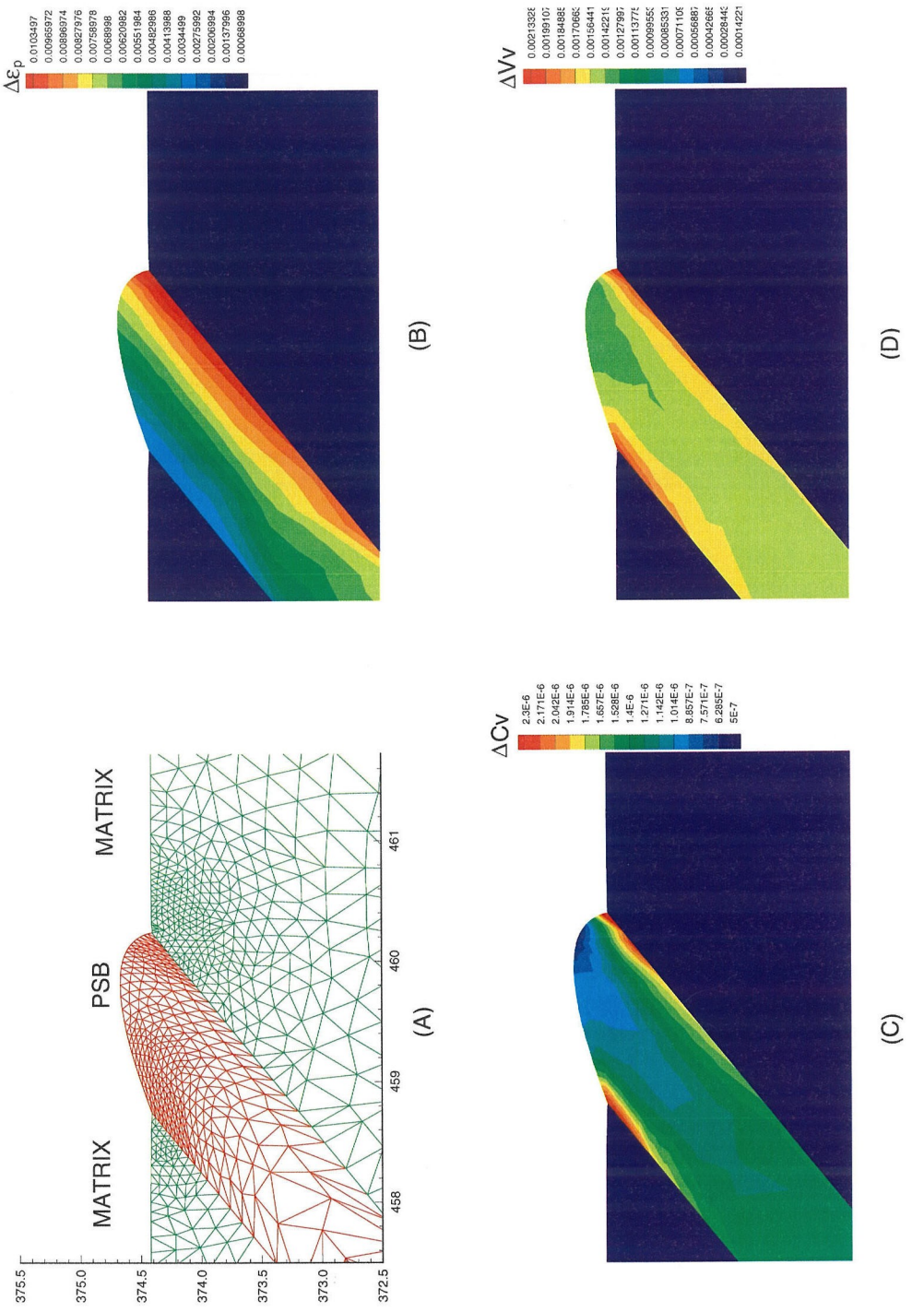

Figure 2.14: Solution after 45,000 cycles. a) Deformed mesh; b) equivalent slip strain increment ($\sum_\alpha \triangle\gamma^\alpha$); c) vacancy concentration increment; d) volume increment ($\det(\mathbf{F}^v)$). All increments correspond to one cycle.

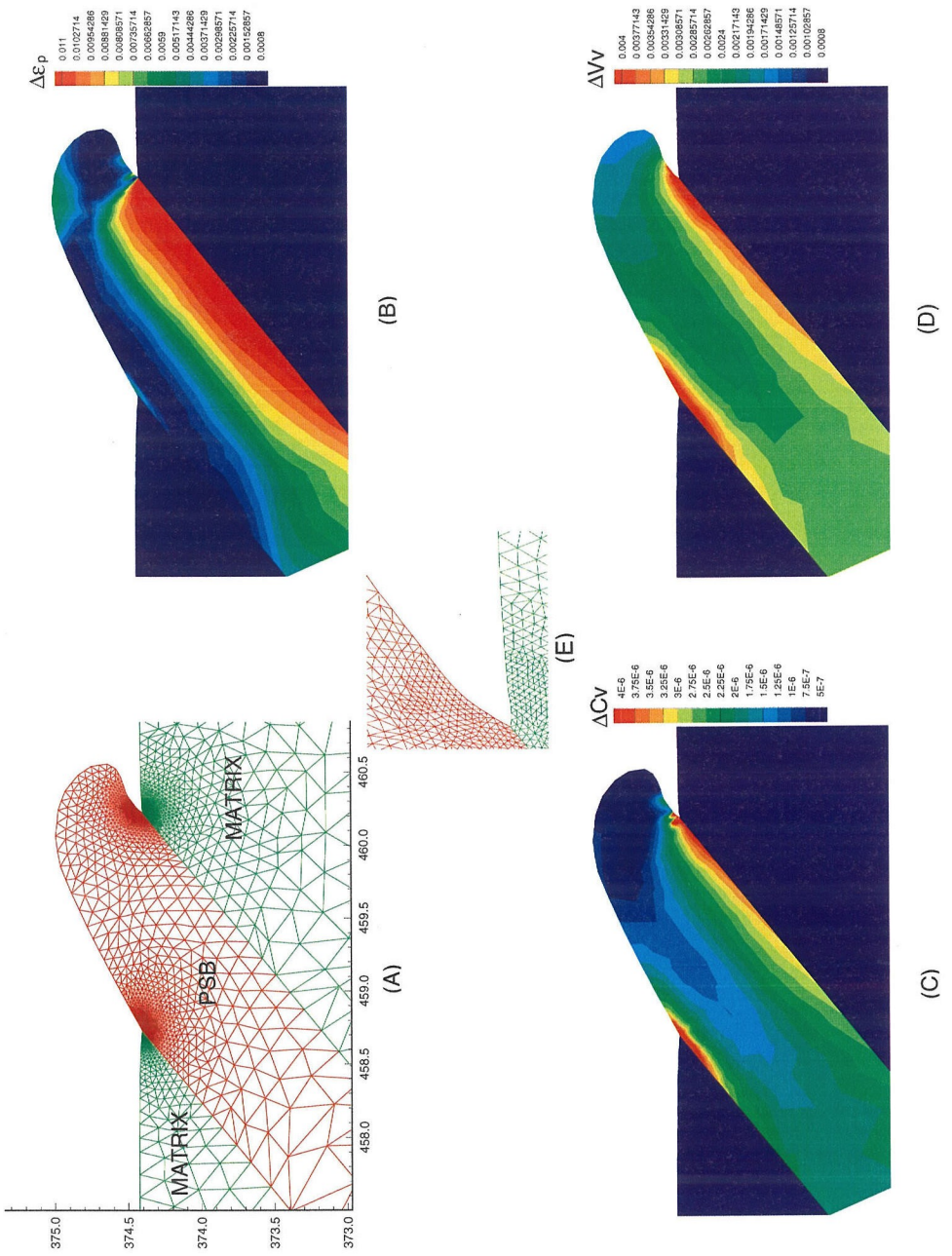

Figure 2.15: Solution after 65,000 cycles. a) Deformed mesh; b) equivalent slip strain increment ($\sum_\alpha \Delta\gamma^\alpha$); c) vacancy concentration increment; d) volume increment ($\det(\mathbf{F}^v)$); e) close-up view of the nascent crack. All increments correspond to one cycle.

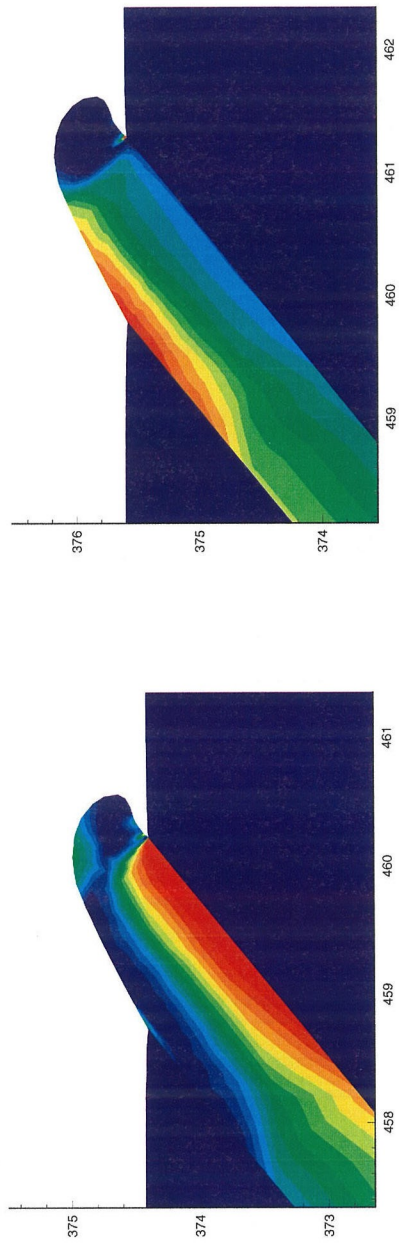

Figure 2.16: Slip activity distribution during the compressive and tensile half-cycles.

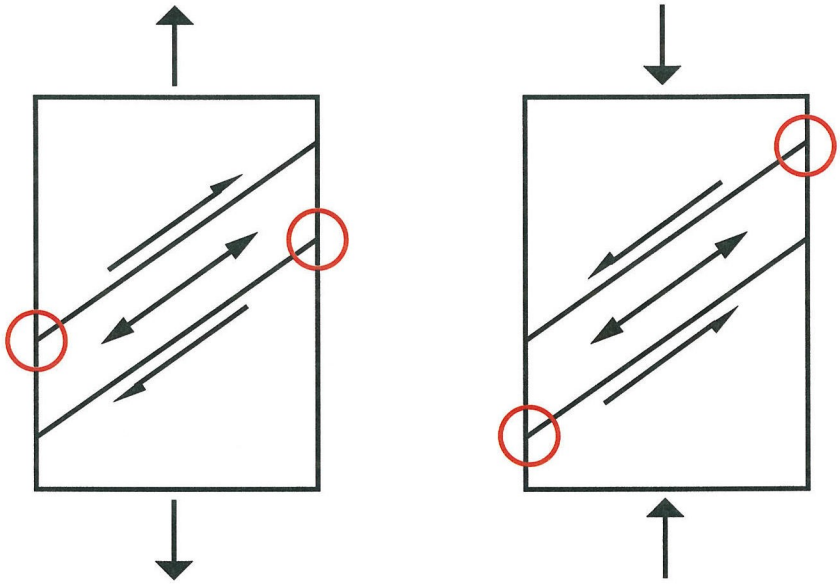

Figure 2.17: Schematic model for the alternating slip activity.

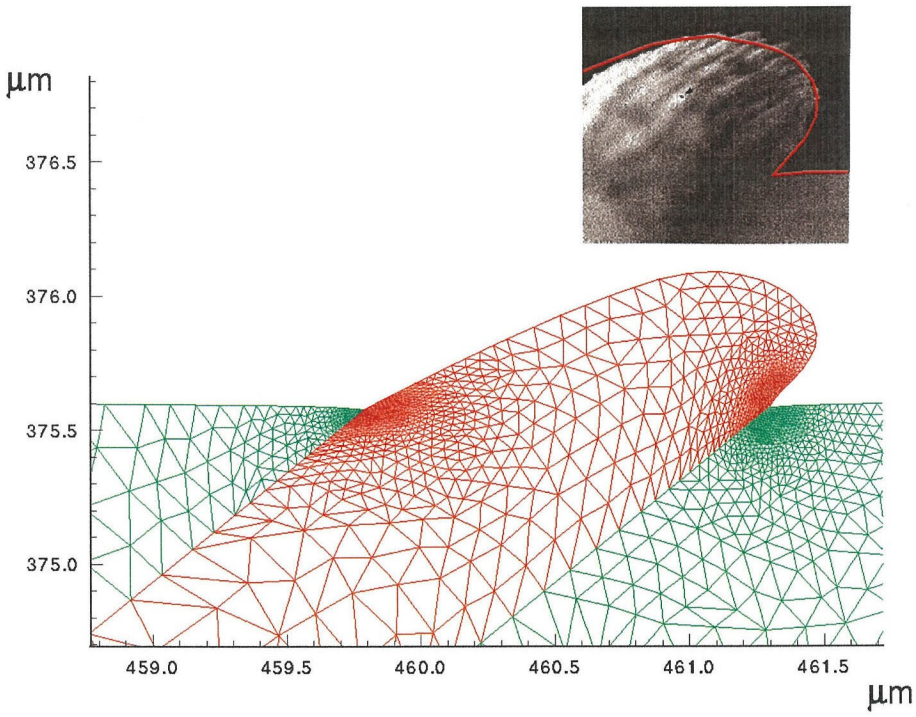

Figure 2.18: Experimental and numerical surface profiles.

PSB elongation. The final shape of the surface protrusion and the attendant fields after 65,000 cycles is shown in Fig. 2.5. As the elongation of the PSB is constrained by the matrix, the PSB is left in a state of residual compression. As pointed out by Lin [Lin92], this compression combines with the applied loads to cause the slip activity to alternate from the acute corner of the protrusion during the compressive half-cycle to the obtuse corner during the tensile half-cycle, Fig. 2.5 and 2.5.

The shape of the protrusion is the result of a competition between the elongation of the PSB, which pushes material out of the matrix, and the vacancy flux through the surface, which causes the surface to recede. Elongation wins out at the center of the PSB, which results in the development of a protrusion. Compatibility between PSB and matrix requires the activation of multiple slip systems near the surface and forces the protrusion to take on a rounded shape. The magnitude of the local deformations near the surface can be quite substantial, which attests to the need for finite-deformation computational capability. Continuous remeshing is also required to maintain the aspect ratio of the elements within acceptable bounds. A close-up view of a typical adapted mesh is shown in Fig. 2.5, showing the requisite mesh refinement at the re-entrant corners of the protrusion. Fig. 2.5 also shows a comparison between the computed protrusion profile and that observed by Differt *et al.* [DEM86]. The good agreement between the predictions of the theory and observation is evident from the figure. The rate at which the protrusion grows is shown in Fig. 2.5. Initially the rate of growth is slow. At about 30,000 cycles the rate of growth accelerates and eventually attains a nearly constant value.

Remarkably, the combination of PSB elongation, multiple slip at the re-entrant corners and, most notably, vacancy flux through the surface results in the development of *grooves*. These grooves are clearly visible in Fig. 2.5, especially at the acute corner of the protrusion. A close-up view of this groove, which has already developed into a sharp notch, is shown in Fig. 2.5e. A measure of the sharpness of the grooves is the angle α subtended at the apex. The variation of these angles with the number of cycles is shown in Fig. 2.5. As may be seen from this figure, sharpening of the main groove accelerates after about 30,000 cycles and subsequently attains a constant rate.

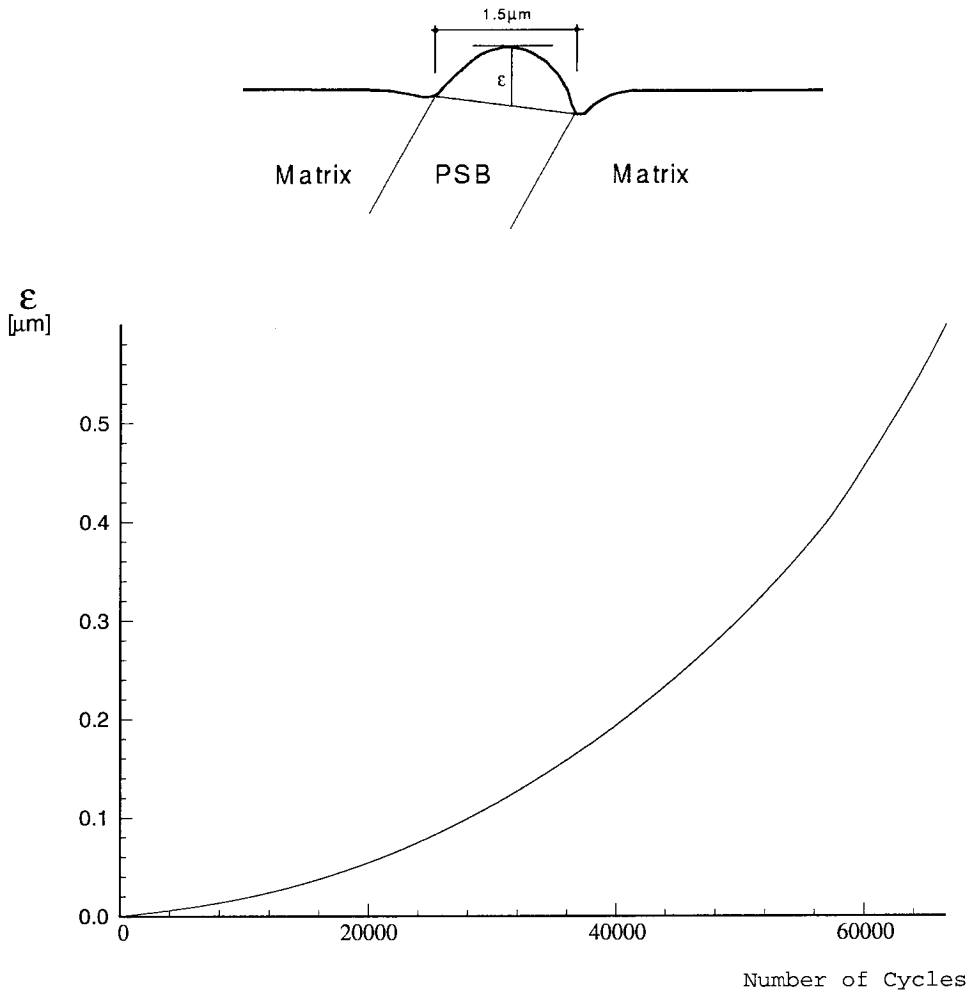

Figure 2.19: Growth of extrusion with number of cycles.

The extrapolation of this trend to the limit of $\alpha = 0$ affords an unequivocal definition of fatigue-crack nucleation. In the present simulation, nucleation occurs after about 80,000 cycles. An alternative measure of the extent of growth of the grooves is their depth δ. The variation of this depth with the number of cycles is shown in Fig. 2.5. As before, growth accelerates at roughly 30,000 cycles and subsequently attains a constant rate.

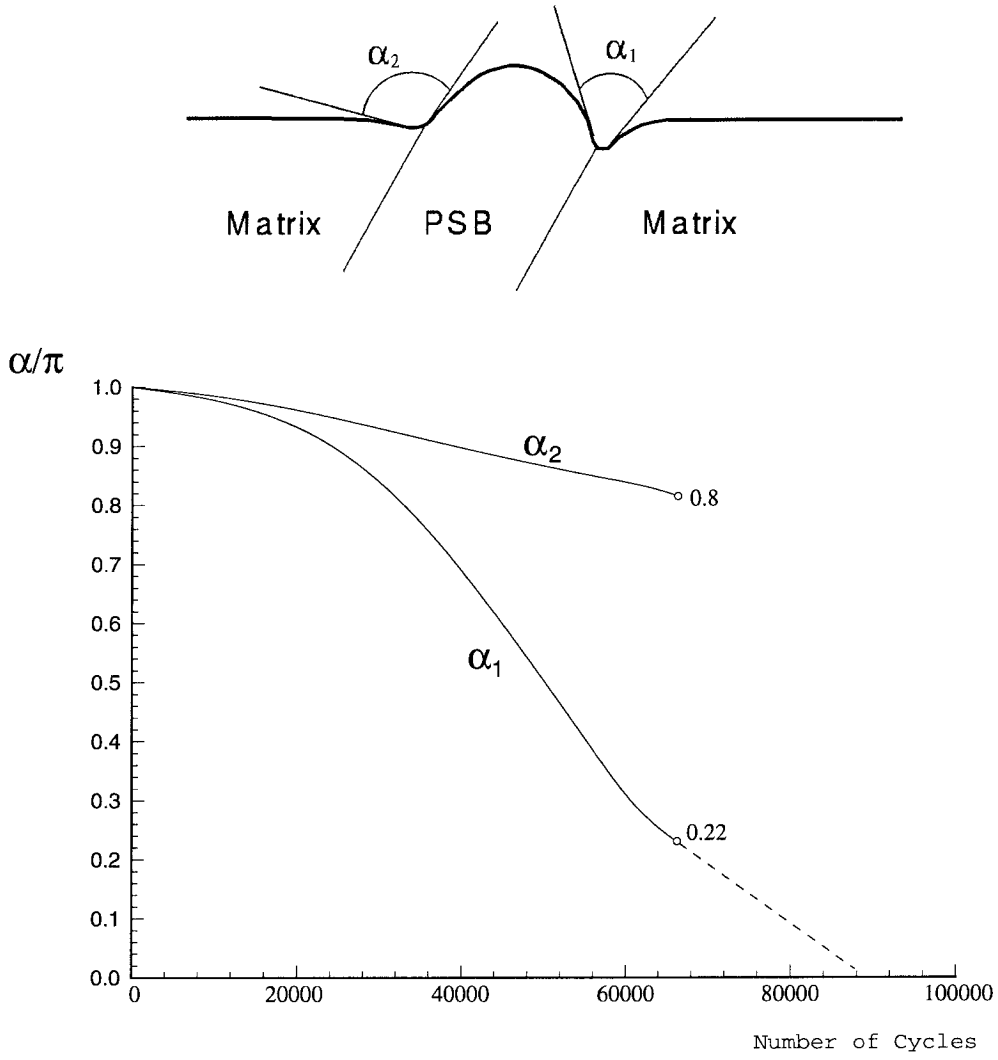

Figure 2.20: Evolution of the groove angles with the number of cycles.

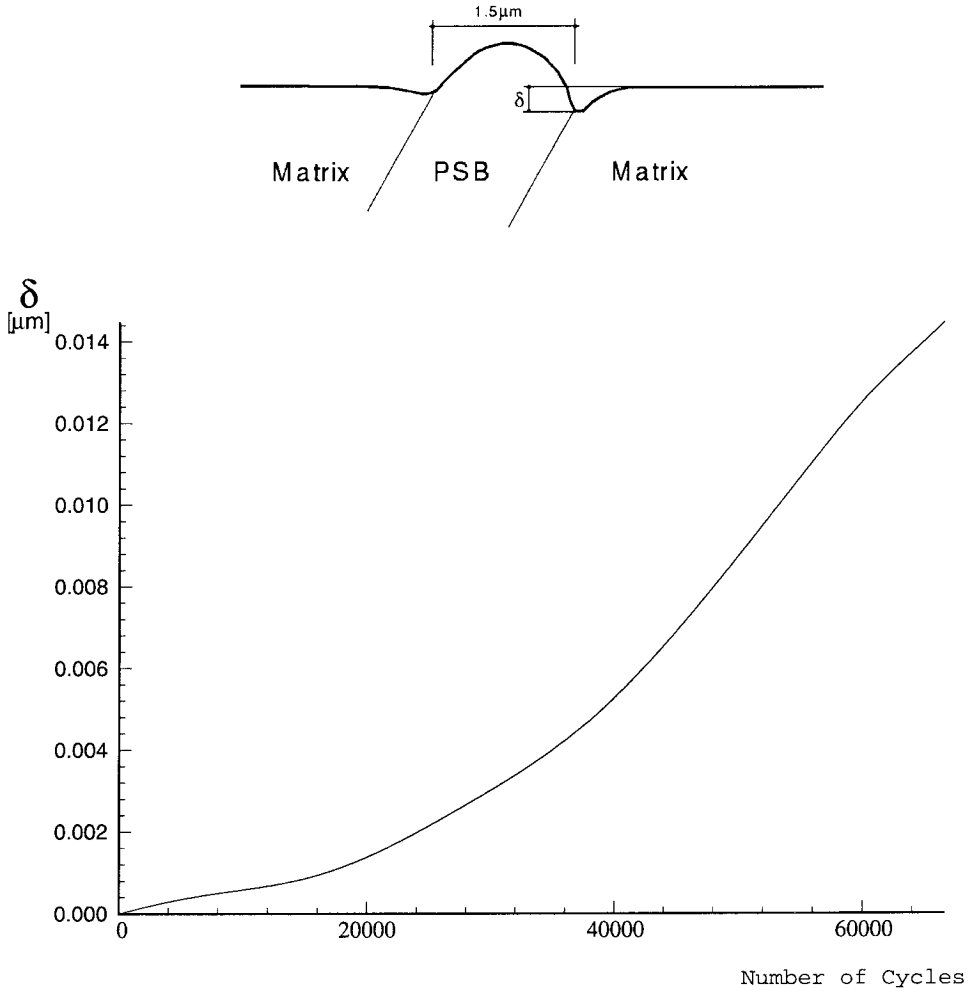

Figure 2.21: Evolution of the main groove depth with the number of cycles.

2.6 Summary and conclusions

We have developed a micromechanical finite-element model of fatigue-crack initiation in nominally defect-free F.C.C. metals. The scale of observation envisioned is that of a single persistent slip band (PSB) intersecting the free surface of a near-surface grain. The nucleation event is identified with the formation of a sharp surface crack, whose subsequent growth obeys the laws of fracture mechanics. Basic building blocks of the theory are: a model of cyclic plasticity tailored to PSBs which accounts for the Bauschinger effect, PSB elongation due to pair annihilation, and vacancy generation; and a model of vacancy diffusion which accounts for pipe diffusion and the surface motion resulting from the outward flux of vacancies.

Our numerical simulations show that the outward vacancy flux causes the surface to recede, which promotes the formation of grooves at the PSB/matrix interface. These grooves sharpen steadily until, after a predictable number of cycles, the angle subtended by one of the grooves reduces to zero. This event furnishes an unequivocal definition of fatigue-crack nucleation. It also signals the end of the range of usefulness of the model, as the expectation is that once a sharp crack is formed and the attendant singular field is established at its tip, laws governing the subsequent growth of the crack can be formulated within the conventional confines of fracture mechanics. Thus, fracture mechanics picks up where the present theory exhausts its usefulness.

The numerical model developed in the foregoing opens the possibility of detailed parametric studies of the dependence of fatigue-crack nucleation on material properties and microstructure, loading and temperature histories, and environmental conditions.

2.7 Appendix I. The Bauschinger effect

Ortiz and Popov [OP82] derived a kinetic equation governing the evolution of the obstacle strength density function $f(s)$ during reverse slip. The kinetic equation is

$$\frac{\partial f}{\partial t} = \frac{\dot{\gamma}}{\gamma_c}(\tilde{f}(s) - f(s)) \tag{2.34}$$

where $\dot{\gamma}$ is the slip rate in the reverse slip direction and γ_c is a characteristic slip strain. Evidently, (2.34) compels f to approach the virgin distribution $\tilde{f}$ with large γ on the scale of γ_c. Eq. (2.34) is linear in f and its solution is elementary [OP82]. However, the function f at the end of reverse loading is not generally of the form (2.7) and, upon reloading, the hardening modulus differs from (2.12). An approximate–but computationally convenient–treatment of (2.34) is to insert into (2.34) a trial function of the form (2.17), which is consistent with (2.7), and collocate (2.34) at τ_0. After a trite calculation, this procedure yields the rate equation

$$\frac{\partial \tau_0}{\partial t} = -\frac{\dot{\gamma}}{\gamma_c}\frac{\tilde{P}(\tau_0)(1-\tilde{P}(\tau_0))}{\tilde{f}(\tau_0)}. \tag{2.35}$$

Rearranging terms, this equation can be written in the form

$$\frac{d\tilde{P}(\tau_0)}{d\gamma} = -\frac{1}{\gamma_c}\tilde{P}(\tau_0)(1-\tilde{P}(\tau_0)). \tag{2.36}$$

This equation is separable and admits the solution

$$\log\frac{\tilde{P}(\tau_0)}{1-\tilde{P}(\tau_0)} - \log\frac{\tilde{P}(\tau_{\max})}{1-\tilde{P}((\tau_{\max}))} = -\frac{\gamma}{\gamma_c} \tag{2.37}$$

where $\tau_{\max}$ is the maximum resolved shear stress attained during the previous loading and $\gamma = 0$ coincides with the onset of reverse slip. Evidently, the choice of constants in (2.37) ensures that $\tau_0 = \tau_{\max}$ for $\gamma = 0$, as required. Solving (2.37) for $\tilde{P}(\tau_0)$ finally gives (2.18).

Chapter 3 Non-homogeneous deformations as energy minimizers in ductile crystals and their relation with dislocation structures

3.1 Introduction

Plastically deformed crystals are often observed to develop intricate dislocation structures such as: the dipolar wall, labyrinth and mosaic structures which arise in cyclically deformed polycrystals and in single crystals oriented for multiple slip ([AKLM84]; [RP80]; [Cha81]; [MB82]; [BBT85]; [JW84a]; [WM84]; [LVD86]; [LKK86]); the persistent slip bands in cyclically deformed crystals oriented for single slip ([Mug78]; [Woo73]; [Win74]); the coplanar slip zones which develop during the stage I of hardening of FCC single crystals [HTN86]; and the fence and carpet structures characteristic of the early stages of stage II of hardening ([HTN86]; [Ste66]), to name a few salient examples. The characterization of these and other dislocation structures from first principles of mechanics has long been a principal–albeit largely unfulfilled–aim of physical metallurgy.

It has been suggested that at least some of these structures can be understood as energy minimizers ([HKW86]; [LCM86]; [LWMC89]). Neumann [Neu86] investigated the structure and stability of loop patches, such as are found in the matrix of single crystals oriented for single slip and cycled to saturation, by explicitly considering an ensemble of parallel straight edge dislocations and numerically minimizing their interaction energy. A similar approach has been followed in other recent studies of dislocation loop patches [LBN93]. In these investigations, the primary unknown is the

equilibrium position of the discrete dislocations, and their motion, which is driven by their mutual interaction forces, is not explicitly related to the plastic deformation of the crystal. Consequently, the resulting structures cannot be interpreted as deformation microstructures in general.

Kocks [Koc60] pointed out that interactions between primary and secondary dislocations, which are responsible for latent hardening in single crystals, necessarily inhibit the simultaneous operation of more than one slip system over the same region of the crystal and, consequently, cause the slip activity to segregate into regions of single slip. Mobile dislocations belonging to two neighboring active systems meet at the interface between the corresponding single slip regions and interact strongly, e.g., through the formation of immobile sessile jogs. The accumulation of such trapped dislocations leads to the formation of dislocation walls. In general, these dislocation walls contain two types of glide dislocations and therefore are referred to as dipolar walls (e.g., [HKW86]). According to the energy minimization principle, the walls thus formed should tend to adopt energy minimizing configurations. The minimum condition was derived by Frank [Fra50] within the framework of linear elasticity. In turn, Hirth and Lothe [HL68] (see also [BS86]) found the dipolar walls which satisfy Frank's condition. Evidently, this theory relates the dislocation structures to plastic deformation processes only to the extent that the dislocation walls are required to be composed of glide dislocations.

Despite the valuable insights revealed by these studies, a comprehensive mathematical analysis of dislocation structures in plastically deformed crystals does not appear to have been attempted. In particular, the recently developed direct methods of the calculus of variations (e.g., [Dac89]), including notions of weak convergence and effective behavior, have not been applied to ductile single crystals to the best of our knowledge. One of the primary goals of this work is to formulate the problem of the determination of dislocation structures as a nonconvex minimization problem. Because the constitutive behavior of ductile single crystals is inelastic, it is not immediately clear what–if any–minimum principle characterizes the stable equilibrium configurations of the crystals. We show, however, that a sequence of pseudoelastic

energy densities may be defined which is minimized by the successive incremental deformations of the crystal. The incremental nature of the variational principle reflects the inelastic and irreversible nature of plastic deformations.

The identification of an incremental pseudoelastic energy confers the problem of determining the equilibrium deformations of ductile single crystals a variational character. It also reveals the following crucial insight: the pseudoelastic energy densities of crystals undergoing geometrical softening or latent hardening are *nonconvex*. Here geometrical softening refers to a reduction in the resolved shear stress required for the operation of a system induced by lattice rotations [Asa83]; and latent hardening refers to a high rate of hardening of the primary system due to the activation of a secondary system ([Koc66]; [BW91a]; [BW91b]; [FBZ80]; [Koc64]; [RKC65]). In particular, we find that the pseudoelastic energy density of previously undeformed crystals possessing latent hardening has wells corresponding to those deformations which are attainable by the activation of a single slip system followed by a lattice or elastic rotation. Such crystals find it energetically favorable to deform locally in single slip. A strategy for minimizing the energy of the crystal is, in essence, to attempt to construct compatible deformations satisfying the following requirements: the plastic deformation field consists locally of single slip; the elastic deformation consists locally of a lattice rotation, which ensures the absence of "long-range stresses"; and the average deformation matches a prescribed macroscopic value. A somewhat more precise statement of this prescription is given in Section 3.4 in terms of minimizing sequences of deformations.

As just stated, the determination of microstructures in ductile single crystals is strictly a problem of compatibility and, as such, is in analogy to other problems of microstructural development, e.g., those arising in the crystallographic theory of martensite ([BJ87]; [Koh91]; [Bha91]; [KM92]; [Bha92]). It bears emphasis that the present theory seeks primarily to characterize the equilibrium *deformations* of ductile single crystals, and is therefore at variance with approaches which regard the disposition of discrete dislocation ensembles as the primary unknown. However, it should be carefully noted that the energy-minimizing dislocation structures may be

deduced from the deformation fields. Thus, while the deformation gradient field must be compatible in some suitable sense, neither the elastic nor the plastic deformation fields need be compatible in general. Physically, the incompatibility of the plastic and elastic deformations is equivalent to a distribution of dislocations. The mathematical connection between dislocations and incompatibility is discussed in Section 3.4 and used subsequently to infer the geometry of dislocation structures.

In Section 3.4.1, interfaces between two single slip variants are characterized analytically. These interfaces are subsequently taken as the basic building block for sequential lamination, which results in the construction of complex wall structures. The general results are specialized to the FCC crystal class in Section 3.5. The predicted interfaces are of a precise crystallographic character and constitute a compendium of commonly observed dislocation walls, e.g., the $\{100\}$ walls characteristic of the labyrinth structures in cyclically deformed crystals oriented for multiple slip ([Cha81]; [MB82]); [BBT85]; [JW84a]; [AKLM84]; [LVD86]), which attests to the soundness of the theory. Many commonly observed dislocation structures consist of roughly parallel arrays of dislocation walls which, we argue, are instances of lamination. This includes coplanar slip zones such as observed by Higashida *et al.* [HTN86] to form during the stage I of hardening in Cu-1at.%Ge single crystals; the fence structures observed during the early stages of stage II of hardening in FCC crystals [Ste66]; and the parallel arrays of dipolar walls which develop in FCC crystals fatigued to saturation ([WM84]; [Yum89]; [LKK86]; [Bou83]; [DBL86]; [DHL86]). An instance of a possible rank-two laminate, or a laminate of laminates, is discussed in Section 3.5.4.

Finally, in Section 3.6 a nonlocal extension of the theory is derived by adding to the local free energy density of the crystal the self-energy density of the dislocations. This extension introduces an absolute microstructural length scale and permits to accord the dislocation walls a well-defined interfacial energy. On the basis of this interfacial energy, the spacing l of the dislocation walls is estimated. In the absence of branching the theory predicts the scaling laws $l \sim L^{1/2}$ and $l \sim \gamma^{-1/2}$ in terms of the grain size L and the slip strain γ, respectively. This latter scaling relation is consistent with observations of the dependence of cell sizes on the applied strain

[BK86]. Simple estimates of the wall spacing in copper single crystals fatigued to saturation are also in the ball park of experimental observation.

3.2 Variational formulation of inelastic problems

Our first objective is to devise a variational formulation for *inelastic solids.* In particular, we endeavor to formulate the boundary value problem of finite deformation plasticity as a sequence of *incremental* energy minimization problems. The appropriate definition of the energy function to be minimized is the principal aim of this section. We show that, when the constitutive equations are integrated along deformation histories which minimize the work of deformation, the resulting incremental stress-strain relations take a pseudoelastic form, with the work of deformation itself supplying the appropriate strain energy potential. This approach has been used in the past to derive deformation, or pseudoelastic, theories of plasticity ([MP66]; [Mai69]; [SL69]; [CM76]).

3.2.1 Field equations and constitutive framework

We begin by considering a general inelastic solid occupying a domain Ω in its reference configuration. Deformations of the solid are described by deformation mappings $y(x) : \Omega \to R^3$ with gradient

$$F(x) = \nabla y(x). \tag{3.1}$$

We adopt an internal variable formalism ([Lub72]; [Lub73]) to describe inelastic processes undergone by the solid and postulate the existence of a Helmholtz free energy density $\phi(F, q)$ per unit undeformed volume, where $q \in R^N$ is some suitable finite collection of internal variables. For simplicity, we restrict our attention to isothermal processes and omit the dependence of ϕ and all other state functions on temperature. The local value of the first Piola-Kirchhoff stress tensor follows from Coleman's

relations in the form

$$P = \frac{\partial \phi(F, q)}{\partial F}. \tag{3.2}$$

Here and in all subsequent discussions of local behavior, we omit the dependence of the fields on x for simplicity, and local relations such as (3.2) are tacitly presumed to hold at all material points $x \in \Omega$. The equilibrium of the solid demands that

$$\nabla \cdot P = 0. \tag{3.3}$$

In order to determine the evolution of the internal variable field, suitable kinetic equations must be supplied. Assuming that the rate of the internal processes is determined solely by the local thermodynamic state, the general form of the kinetic equations is

$$\dot{q} = f(F, q). \tag{3.4}$$

The second law of thermodynamics places the following restriction on the rate equations:

$$Q \cdot \dot{q} \geq 0 \tag{3.5}$$

where

$$Q = -\frac{\partial \phi(F, q)}{\partial q} \tag{3.6}$$

are the thermodynamic "forces" conjugate to q. The kinetic relations are said to derive from an inelastic potential if there exists a differentiable function $\psi(Q, q)$ such that

$$f = \frac{\partial \psi(Q, q)}{\partial Q}. \tag{3.7}$$

For single crystals, the concept of inelastic potential was introduced by Rice [Ric75].

All the preceding constitutive relations are subject to material frame indifference, i. e., must remain invariant under superimposed rigid body motions. In the particular case in which the internal variables are scalars or remain unchanged under rotations superimposed on the deformed configuration, material frame indifference requires that

$$\phi(RF, q) = \phi(F, q), \qquad \forall R \in SO(3). \tag{3.8}$$

A standard exercise (see, e.g., [Gur81]) then shows that the most general form of ϕ consistent with the requirements of material frame indifference is

$$\phi = \phi(C, q), \qquad C = F^T F \tag{3.9}$$

where C is the right Cauchy-Green deformation tensor.

3.2.2 Minimizing deformation paths

We shall assume sufficient regularity of the local deformation histories $F(t)$ and the rates $f(F, q)$ to ensure existence and uniqueness of continuously differentiable solutions $q(t)$ of the local initial value problem

$$\dot{q}(t) = f(F(t), q(t)), \qquad q(0) = q_0 \tag{3.10}$$

over some time interval $[0, T]$. For instance, it suffices to assume that $F(t)$ is a continuous function of $t \in [0, T]$ and $f(F, q)$ a continuous function of F satisfying the Lipschitz condition

$$\| f(F, q) - f(F, q') \| \leq L \| q - q' \| \tag{3.11}$$

for all F, q and q', $t \in [0, T]$, and some constant L (see, e.g., [Gea71]). These conditions may reasonably be expected to be met, e.g., by most models of viscoelastic and viscoplastic behavior, including viscoplastic regularizations of rate-independent

plasticity models (see [Lub72] for examples of these models; [Ort81], chp. 3, for a discussion of the viscoplastic regularization). If the rates satisfy the Lipschitz condition (3.11), it then follows that problem (3.10) is well-posed with respect to the initial conditions, i. e., there exists a constant M such that

$$\| q(t) - q'(t) \| \leq M \| q_0 - q'_0 \| \tag{3.12}$$

for all q and q', $t \in [0, T]$ (see, e.g., [Gea71]).

In order to define an incremental pseudoelastic energy density, we consider the following auxiliary local problem. Let $F(t)$ and $q(t)$, $t \in [0, T]$, be deformation and internal variable histories at the point under consideration. Suppose that the initial conditions $F(0)$ and $q(0)$ are known and the final deformation $F(T)$ is prescribed. Then we wish to determine histories of deformation $F(t)$, having the prescribed initial and terminal values $F(0)$ and $F(T)$, respectively, which minimize the work of deformation density

$$W = \int_0^T P \cdot \dot{F} dt. \tag{3.13}$$

In writing (3.13) it is tacitly understood that $q(t)$ follows from $F(t)$ by integration of the kinetic equations (3.4). From relations (3.2) and (3.6), (3.13) may be recast as

$$W = \int_0^T (\dot{\phi} + Q \cdot \dot{q}) dt. \tag{3.14}$$

The first term is a perfect differential and integrates exactly, with the result

$$W = [\phi]_0^T + \int_0^T Q \cdot \dot{q} dt. \tag{3.15}$$

The minimizing deformation paths satisfy the stationarity condition

$$\delta W = \left[\frac{\partial \phi}{\partial F} \cdot \delta F + \frac{\partial \phi}{\partial q} \cdot \delta q \right]_0^T + \int_0^T [\delta Q \cdot \dot{q} + Q \cdot \delta \dot{q}] dt = 0. \tag{3.16}$$

Using (3.2) and the fact that $\delta F(0) = 0$, (3.16) reduces to

$$\delta W = P(T) \cdot \delta F(T) + \left[\frac{\partial \phi}{\partial q} \cdot \delta q\right]_0^T + \int_0^T [\delta Q \cdot \dot{q} + Q \cdot \delta \dot{q}] dt = 0. \tag{3.17}$$

An integration by parts of the second term in the integrand and (3.6) gives

$$\delta W = P(T) \cdot \delta F(T) + \int_0^T [\delta Q \cdot \dot{q} - \dot{Q} \cdot \delta q] dt = 0. \tag{3.18}$$

Finally, noting that $\delta F(T) = 0$, since $F(T)$ is prescribed, results in the stationarity condition

$$\delta W = \int_0^T [\delta Q \cdot \dot{q} - \dot{Q} \cdot \delta q] dt = 0 \tag{3.19}$$

which determines the minimizing deformation paths $F(t)$.

3.2.3 Rate-independent behavior

The stationarity condition (3.19) simplifies further in the case of rate-independent behavior. Let $q(t)$ be the solution of (3.10) corresponding to a deformation history $F(t)$, and let $s(t)$ be an absolutely continuous, monotonically increasing function of $t \in [0, T]$. The solid is said to be rate-independent if the solution of (3.10) corresponding to the deformation history $F(s(t))$ is $q(s(t))$ for all $F(t)$. Solids which are not rate independent are said to be rate dependent.

A rate-independent theory of inelastic behavior may be formulated by identifying an N-parameter family of convex sets $K(q) \in R^N$. The convex sets $K(q)$, which are allowed to have corners, define the elastic domain of the solid. As will become apparent in subsequent applications to finite-deformation plasticity, an explicit dependence of K on q is generally required in order to account for geometric effects. Introduce

the inelastic potential:

$$\psi(Q,q) = I_{K(q)}(Q) \quad = 0, \qquad \text{if } Q \in K(q) \tag{3.20}$$
$$= \infty, \qquad \text{otherwise.}$$

Here, $I_{K(q)}(Q)$ is the indicator function of the convex set $K(q)$ [Roc70]. Evidently, this function is not differentiable with respect to Q in the ordinary sense, which precludes a direct application of (3.7). Nonetheless, it was noted by Moreau ([Mor62]; [Mor63]; [Mor65]; [Mor66]; [Mor67]; [Mor70]; [Mor71]; [Mor74]; [Mor76]) in his pioneer work on plasticity that the convexity of $K(q)$ permits the definition of a generalized derivative of $I_{K(q)}(Q)$ with respect to Q, or 'subdifferential', which gives the conventional flow rules of plasticity a rigorous mathematical meaning. A detailed discussion of subdifferentials and their relation to plasticity may be found in [Ort81]. For present purposes, it suffices to note that the subdifferential of $I_{K(q)}(Q)$ is the set-valued function

$$f(Q,q) = \partial_Q I_{K(q)}(Q) = \{\dot{q} \quad s.\ t.\ (Q - Q') \cdot \dot{q} \geq 0,\ \forall Q' \in K(q)\}. \tag{3.21}$$

It follows from this definition that the rates $f(Q,q) = 0$ if Q belongs to the interior of $K(q)$, while $f(Q,q)$ is any element of the normal cone if Q is on the boundary $\partial K(q)$ of $K(q)$ [Ort81], in agreement with the conventional definition of the flow rule in rate-independent plasticity. The subdifferential of a differentiable function coincides with its ordinary derivative. Therefore, (3.7) may be extended to the rate-independent case by simply interpreting derivatives with respect to Q in the sense of subdifferentials as required.

An alternative device for sidestepping the mathematical difficulties inherent to rate-independent behavior is to resort to a viscoplastic regularization. A particularly convenient procedure is furnished by the classical Yosida's regularization of nonlinear semigroup theory [Yos65], leading to linear viscoplasticity. The relation between the Yosida regularization and linear viscoplasticity was first noted by Ortiz [Ort81]. Let

$P_{K(q)}(Q)$ denote the closest point projection of R^N onto $K(q)$. Thus,

$$\| Q - P_{K(q)}(Q) \| = \min_{Q' \in K(q)} \| Q - Q' \| \tag{3.22}$$

for some suitable norm $\| \cdot \|$. Then the Yosida or linear viscoplastic regularization of (3.20) is

$$f_\epsilon = \frac{1}{\epsilon}[Q - P_{K(q)}(Q)] \tag{3.23}$$

where ϵ is a viscosity constant which plays the role of a small parameter. This class of kinetic equations satisfies all the regularity requirements assumed in Section 3.2.2. In addition, it follows from general results of nonlinear semigroup theory ([CP69]; [CP70]; [Ort81]) that the solutions $q_\epsilon(t)$ of the initial value problem (3.10) corresponding to the kinetic relations (3.23) and the rate-independent solutions $q(t)$ corresponding to (3.21) satisfy the bound:

$$\| q(t) - q_\epsilon(t) \| \leq C\sqrt{\epsilon t} \tag{3.24}$$

which shows that the linear viscoplastic solution converges to the rate-independent solution in the inviscid limit $\epsilon \to 0$. Since ϵ sets the temporal scale, it additionally follows that the linear viscoplastic solution converges to the rate-independent solution in the quasistatic limit, i. e., for sufficiently slow deformation processes. These results show that the subdifferential formalism (3.21) required to represent rate-independent behavior, which necessitates the consideration of lower semi-continuous inelastic potentials of the form (3.20), may be conveniently sidestepped, if so desired, by considering slightly viscous regularizations of the form (3.23), with the rate-independent behavior recovered in the limit of $\epsilon \to 0$.

It is readily verified that, for rate-independent solids,

$$\delta Q \cdot \dot{q} = 0. \tag{3.25}$$

Thus, if $Q(t)$ is in the interior of $K(q(t))$, then $\dot{q}(t) = 0$ and (3.25) holds. If $\dot{q}(t) \neq 0$, then $\delta Q(t)$ must represent neutral loading and be contained within the tangent cone to $K(q(t))$ at $Q(t)$. But, $\dot{q}(t)$ lies within the normal cone to $K(q(t))$ at $Q(t)$ and, consequently, (3.25) also holds. In view of (3.25), the stationarity condition (3.19) reduces to

$$\delta W = -\int_0^T \dot{Q} \cdot \delta q \, dt = 0 \tag{3.26}$$

for rate-independent solids. Clearly, for a purely elastic deformation history, such that $Q(t)$ lies in the interior of $K(q(t))$ for all $t \in [0, T]$, $\delta q(t)$ is necessarily zero and (3.26) is trivially satisfied. It thus follows that all elastic paths are extremal.

3.2.4 Pseudoelastic incremental behavior

Let $W(F(T); F(0), q(0))$ be the work of deformation per unit undeformed volume computed along a minimizing path joining $F(0)$ to $F(T)$.

Consider now a small variation $\delta F(T)$ of the terminal deformation. The corresponding variation of $W(F(T); F(0), q(0))$ is given by (3.18). But, since by assumption $W(F(T); F(0), q(0))$ is computed along a minimizing path, the stationarity condition (3.19) holds and (3.18) reduces to

$$\delta W = P(T) \cdot \delta F(T). \tag{3.27}$$

This shows that $W(F(T); F(0), q(0))$ is a pseudoelastic potential for $P(T)$, i.e.,

$$P(T) = \frac{\partial W(F(T); F(0), q(0))}{\partial F(T)} \tag{3.28}$$

which is the sought incremental constitutive relation. Despite the similarity between (3.28) and hyperelastic constitutive relations, the inelastic character (history dependent) of the material is clearly belied by the incremental form of $W(F(T); F(0), q(0))$ and its dependence on the initial conditions $(F(0), q(0))$. It follows from material

frame indifference that if $F(t)$ is a minimizing path, then $R(t)F(t)$ is also a minimizing path for any rigid motion $R(t) \in SO(3)$ and does the same work of deformation W over the interval $[0, T]$. In particular, the pseudoelastic strain energy density $W(F(T); F(0), q(0))$ satisfies material frame indifference.

Besides leading to the incremental constitutive relations (3.28), an integration of the kinetic equations (3.4) along a minimizing deformation path yields a terminal value

$$q(T) = K(F(T); F(0), q(0)) \tag{3.29}$$

of the internal variables. By construction, the mapping K is consistent with the kinetic equations (3.4) in the sense that

$$f(F(0), q(0)) = \left[\frac{d}{dT} K(F(T); F(0), q(0))\right]_{T=0} \tag{3.30}$$

for all initial conditions $F(0)$ and $q(0)$. Additionally, because $K(F(T); F(0), q(0))$ is the *exact* integral of (3.4) along a minimizing path, it follows from (3.12) that K satisfies the Lipschitz condition

$$\| K(F(T); F(0), q(0)) - K(F(T); F(0), q'(0)) \| \leq M \| q(0) - q'(0) \| \tag{3.31}$$

which may be regarded as a stability condition (see, e.g., [Gea71], p. 55).

Evidently, actual deformation histories need not be minimizing paths. However, in order to approximate the effect of an arbitrary deformation history $F(t)$, $t \in [0, T]$, we may sample $F(t)$ at discrete times $t_n = n\triangle t$, $n = 0, 1, \ldots N$, $\triangle t = T/N$, and apply the mapping (3.29) recursively to obtain the sequence

$$q_{n+1} = K(F_{n+1}; F_n, q_n), \qquad n = 0, \ldots, N-1 \tag{3.32}$$

where $F_n = F(t_n)$. At every step, the new stresses P_{n+1} derive from the pseudoelastic

energy density $W(F_{n+1}; F_n, q_n)$ as

$$P_{n+1} = \frac{\partial W(F_{n+1}; F_n, q_n)}{\partial F_{n+1}}. \tag{3.33}$$

As expected, the response is history dependent, i. e., P_N depends not only on the terminal deformation F_N but on the complete history of deformation $\{F_n,\ n = 0, \ldots, N\}$. While this incremental procedure is clearly approximate, it follows that the incremental internal variable history converges to the exact one as the number of steps increases. More precisely, the consistency and stability of K, eqs. (3.30) and (3.31) respectively, guarantee that

$$q_{t/\triangle t} \to q(t), \qquad \text{as } \triangle t \to 0 \tag{3.34}$$

(see, e.g., [Gea71], p. 57).

3.2.5 Inelastic boundary value problems

The chief advantage of the incremental procedure just outlined is that the incremental stress-strain relations are pseudoelastic, which opens the way for the application of variational methods to inelastic solids. For the purposes at hand, it is sufficient to consider affine displacement boundary conditions of the form

$$y(x,t) = \bar{F}(t)x, \qquad x \in \partial\Omega, \quad t \in [0,T] \tag{3.35}$$

Since, by the divergence theorem, one has

$$\bar{F}(t) = \frac{1}{|\Omega|}\int_\Omega \nabla y(x,t)dx \tag{3.36}$$

$\bar{F}(t)$ may be regarded as a prescribed history of average deformation. A dual picture, consisting of the application of tractions $T(t) = \bar{P}(t) \cdot n$ all around $\partial\Omega$, has been developed by Ball *et al.* [BCJ95]. Here n denotes the unit normal to $\partial\Omega$. In this approach, $\bar{P}(t)$ represents a history of average stress imparted to the solid by some

suitable loading device.

In anticipation of the emergence of fine microstructures, we adopt a variational definition of equilibrium and identify the stable equilibrium deformations of the solid with the minimizers of the pseudoelastic energy

$$E(y_{n+1}) = \int_\Omega W(\nabla y_{n+1}(x); y_n(x), q_n(x))dx. \tag{3.37}$$

By definition, $E(y_{n+1})$ is the total work of deformation done as the deformation jumps from $F_n(x) = \nabla y_n(x)$ to $F_{n+1}(x) = \nabla y_{n+1}(x)$ along local minimizing paths at all points $x \in \Omega$. It should be carefully noted that, while the deformation gradients $F_n(x)$ determined by the incremental procedure are compatible, the intervening deformation histories connecting $F_n(x)$ to $F_{n+1}(x)$ through local minimizing paths may not be compatible in general. Let $y_{n+1}(x)$ be a solution of the variational problem:

$$E(y_{n+1}) = \inf_{y \in Y_{n+1}} \int_\Omega W(\nabla y(x); y_n(x), q_n(x))dx \tag{3.38}$$

where the infimum is taken over some suitable space of functions satisfying the essential boundary conditions (3.35), e.g., $Y_{n+1} = \{y = \bar{F}_{n+1}x + y_0,\ y_0 \in W_0^{1,\infty}(\Omega; R^3)\}$. In addition, let $q_{n+1}(x)$ be obtained by applying the evolutionary mapping (3.32) locally to $(F_n(x), q_n(x))$ with $F_{n+1}(x) = \nabla y_{n+1}(x)$ at every $x \in \Omega$. In view of the potential relations (3.33), it is clear that the Euler-Lagrange equation corresponding to (3.38) is the equilibrium equation (3.3) and, consequently, for smooth solutions the minimum principle (3.38) and (3.3) are equivalent statements of equilibrium. In view of the local convergence property (3.34) of the incremental procedure, we may reasonably expect, under suitable technical conditions, global convergence of $y_{n+1}(x)$ and $q_{n+1}(x)$ to the solutions $y(x,t)$ and $q(x,t)$ should such solutions exist.

The existence of minimizers of (3.38) depends crucially on the quasiconvexity–or lack of it thereof–of the pseudoelastic strain energy density W (see, e.g., [Dac89]). In particular, if W first begins to lack quasiconvexity over the incremental step (t_n, t_{n+1}), there may not exist any energy-minimizing deformation $y_{n+1}(x) \in Y_{n+1}$. It is often

possible, however, to construct minimizing sequences of deformations $y_{n+1}^{(j)}$ which attain the minimum energy in the limit, i. e., such that

$$\lim_j E(y_{n+1}^{(j)}) = \inf_{y \in Y_{n+1}} \int_\Omega W(\nabla y(x); y_n(x), q_n(x)) dx. \tag{3.39}$$

It should be carefully noted that the limit $y_{n+1}^{(j)} \overset{*}{\rightharpoonup} y_{n+1}$ is not a minimizer in general, i. e.,

$$E(y_{n+1}) > \inf_{y \in Y_{n+1}} \int_\Omega W(\nabla y(x); y_n(x), q_n(x)) dx, \tag{3.40}$$

a manifestation of the lack of lower semicontinuity of the functional $E(y)$. Minimizing sequences often exhibit increasingly fine detail and have been found to describe well certain observed microstructures. The examples given in Section 3.5 demonstrate that certain dislocation structures are amenable to a similar interpretation, namely, as minimizers of the energy functional (3.38).

While the concept of minimizing sequence, a *leitmotiv* of the modern calculus of variations, has proved its worth in many applications, the infinite finiteness of the microstructure predicted by the theory is an obvious flaw. The lack of existence of minimizers is particularly cumbersome in the present incremental setting, as a deformation $y_n(x)$ of finite fineness is required, e.g., at time t_n, as the initial condition for the subsequent step. At the core of the degeneracy of the local theory is the lack of a characteristic or intrinsic length in the constitutive description of the material. In other areas of application, regularized theories have been devised by building additional physics into the model, such as surface energy, capillarity, bending and exchange energy. An effect of these higher-order terms in the energy is to introduce an intrinsic length scale l which sets a lower bound for the fineness of the microstructure. Additionally, the higher-order terms may have a direct influence on the microstructure, e.g., by promoting twin branching [KM92]. Often, the augmented energy $E^\epsilon(y)$ is a singular perturbation of $E(y)$ in the small parameter $\epsilon = l/L$, where L is a characteristic dimension of the crystal. By virtue of the smallness of l, the aug-

mented theories retain the ability to account for fine microstructure. Yet another simple device to eliminate unphysically fine structures from the solution is to restrict the minimization of $E(y)$ to a subspace Y^{ϵ}_{n+1} of functions $y = \bar{F}x + y_0$ such that the support of the Fourier transform of y_0 is contained in the ball $|k| \leq 2\pi/l \equiv \Lambda$, where Λ is the wavenumber cutoff. This device is widely used in statistical field theories (e.g., [CL95]) to eliminate "ultraviolet" divergences, and is similar in spirit to the use of a core cutoff radius in the theory of linear elastic dislocations.

In the case of crystal plasticity, the fineness of the dislocation distribution is evidently constrained by the crystal lattice. Consequently, a characteristic material length is the magnitude $|b|$ of the Burgers vector, and the corresponding small parameter is $\epsilon = |b|/L$. It is conceivable that some singularly perturbed version $E^{\epsilon}(y)$ of $E(y)$ might be justifiable on physical grounds. In this work, we shall primarily focus on those features of dislocation microstructures which can be deduced from the local energy $E(y)$. A brief discussion of microstructural sizes and scaling is given in Section 3.6, albeit within the simplified framework of the so-called 'sharp-interface' approximation ([Mod87]; [Ste88]).

3.3 Application to crystal plasticity

In this section, the preceding general framework is specialized to plastic solids and, as a further special case, to ductile single crystals. Simple models of geometrical softening and latent hardening are introduced which inevitably lead to nonconvex pseudoelastic strain energy densities. This lack of convexity in turn lies at the root of some commonly observed deformation and dislocation structures in crystals, as demonstrated in subsequent sections.

3.3.1 Finite-deformation plasticity

Plastic solids are characterized by the existence of a certain class of deformations F^p, or "plastic" deformations, which leave the crystal lattice undistorted and unrotated,

and, consequently, induce no long-range stresses. In addition to the plastic deformation F^p, some degree of lattice distortion F^e may also be expected in general. One therefore has, locally,

$$F = F^e F^p \tag{3.41}$$

and the free energy density follows in the form

$$\phi = \phi(F^e, \gamma) = \phi(F F^{p-1}, \gamma) \tag{3.42}$$

where γ is some suitable set of internal variables. We suppose that, for fixed γ, ϕ is a nice (e.g., quasiconvex) function of F^e attaining a strict minimum for any $F^e \in SO(3)$. The multiplicative elastic-plastic kinematics (3.41) was first suggested by Lee [Lee69] and further developed by others ([Teo69]; [AR77]; [Hav73]; [HR72]; [Man72]; [Ric71]).

The free energy ϕ is subject to the requirement of material frame indifference. It is evident from (3.41) that F^p remains unchanged upon the superposition of a rotation R on F, as such a rotation is absorbed by–and therefore solely affects–F^e. Assuming that the internal parameters γ are scalar or also remain unchanged upon superimposed rotations, material frame indifference requires that

$$\phi(RF^e, \gamma) = \phi(F^e, \gamma), \qquad \forall R \in SO(3). \tag{3.43}$$

A standard exercise (see, e.g., [Gur81]) then shows that the most general form of ϕ, consistent with the requirements of material frame indifference, is

$$\phi = \phi(C^e, \gamma), \qquad C^e = F^{eT} F^e = F^{p-T} C F^{p-1} \tag{3.44}$$

in accordance with (3.9). In (3.44), C^e is the elastic right Cauchy-Green deformation tensor.

For the standpoint of the general theory developed in the preceding section, F^p

may be regarded as a set of distinguished internal variables, with the remainder of the internal variable set collected in the array $\gamma \in R^N$. Thus, the complete set of internal variables is $q = \{F^p, \gamma\}$. A straightforward calculation gives the thermodynamic force conjugate to F^p as

$$S \equiv -\frac{\partial \phi}{\partial F^p} = F^{eT} \frac{\partial \phi}{\partial F^e}(F^e) F^{p-T}. \tag{3.45}$$

It follows from material frame indifference and representation (3.9) of the internal energy that

$$(SF^{pT}C^e)^T = SF^{pT}C^e \tag{3.46}$$

i.e., the tensor $SF^{pT}C^e$ is symmetric. This places three algebraic constraints on S. Additionally, the thermodynamic forces conjugate to γ are

$$-g \equiv -\frac{\partial \phi}{\partial \gamma}. \tag{3.47}$$

The complete set of driving forces is $Q = \{S, -g\}$. Assuming an inelastic potential of the form $\psi(S, g; F^p, \gamma)$, the flow and hardening rules jointly follow from (3.7) in the form

$$\dot{F}^p = \frac{\partial \psi}{\partial S} \tag{3.48}$$

$$\dot{\gamma} = -\frac{\partial \psi}{\partial g} \tag{3.49}$$

where partial derivatives should be interpreted in the sense of subdifferentials in the rate-independent case.

3.3.2 Ductile single crystals

Next, we apply the general framework just outlined to ductile single crystals. Plastic deformations in single crystals are crystallographic in nature. The conventional

$A \equiv (\bar{1}11)$	$B \equiv (111)$	$C \equiv (11\bar{1})$	$D \equiv (1\bar{1}1)$		
$1 \equiv [011]$	$2 \equiv [0\bar{1}1]$	$3 \equiv [101]$	$4 \equiv [10\bar{1}]$	$5 \equiv [1\bar{1}0]$	$6 \equiv [110]$

Table 3.1: Schmid and Boas' nomenclature.

kinetic relations for F^p, or "flow rule," are of the form [Ric71]

$$\dot{F}^p F^{p-1} = \sum_{\alpha=1}^{N} \dot{\gamma}^\alpha s^\alpha \otimes m^\alpha \tag{3.50}$$

where $\gamma^\alpha \in R$, $s^\alpha \in R^3$, and $m^\alpha \in R^3$ are the slip strain, slip direction and slip-plane normal corresponding to slip system α. Plastic irreversibility requires that

$$\dot{\gamma}^\alpha \geq 0 \tag{3.51}$$

A zero value of a slip rate $\dot{\gamma}^\alpha(t)$ signifies that the corresponding slip system α is inactive at time t. We note that the flow rule (3.50) allows for multiple slip, i. e., for simultaneous activity on more than one system over a region of the crystal. A pair (s^α, m^α) is referred to as a "slip system." For instance, in FCC crystals s^α is any cube face diagonal and m^α, any cube diagonal, which gives the 24 slip systems enumerated in Table 3.2. For ease of reference, we adopt Schmid and Boas' nomenclature [SB61] for the slip systems of an FCC crystal; see Table 3.3.2 and *cf.* Fig. 3.1.

Note that we need to differentiate between pairs of slip systems of the form $(+s, m)$ and $(-s, m)$, as we have required that $\dot{\gamma}^\alpha \geq 0$. We shall denote by $\mathcal{S}$ the collection of all slip systems available for plastic deformation. For processes of pure slip, one has $s^\alpha \cdot m^\alpha = 0$, which, in view of (3.50) gives $\mathrm{tr}(\dot{F}^p F^{p-1}) = 0$ and plastic flow is volume-preserving.

The crystallographic flow rule (3.50) can be given the potential structure (3.48) as follows. Begin by introducing the resolved shear stress τ^α on slip system α as

$$\tau^\alpha = (SF^{pT}) \cdot (s^\alpha \otimes m^\alpha) \tag{3.52}$$

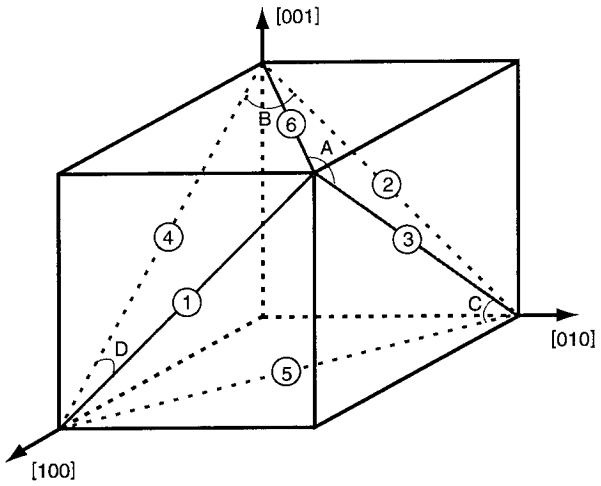

Figure 3.1: Slip systems of an FCC crystal and Schmid and Boas' nomenclature [SB61].

System	B2	B4	B5	A3	A2	A6
$\sqrt{2}s$	$\pm[0\bar{1}1]$	$\pm[10\bar{1}]$	$\pm[\bar{1}10]$	$\pm[101]$	$\pm[01\bar{1}]$	$\pm[\bar{1}\bar{1}0]$
$\sqrt{3}m$	(111)	(111)	(111)	$(\bar{1}11)$	$(\bar{1}11)$	$(\bar{1}11)$
System	C1	C3	C5	D4	D1	D6
$\sqrt{2}s$	$\pm[011]$	$\pm[\bar{1}0\bar{1}]$	$\pm[1\bar{1}0]$	$\pm[\bar{1}01]$	$\pm[0\bar{1}\bar{1}]$	$\pm[110]$
$\sqrt{3}m$	$(\bar{1}\bar{1}1)$	$(\bar{1}\bar{1}1)$	$(\bar{1}\bar{1}1)$	$(1\bar{1}1)$	$(1\bar{1}1)$	$(1\bar{1}1)$

Table 3.2: Slip systems of an FCC crystal.

where the dot product $A \cdot B$ between two matrices A and B is $A_{ij}B_{ij}$. Following Rice [Ric75] we write the flow potential ψ as the sum of slip system contributions, i. e.,

$$\psi(S, g; F^p, \gamma) = \sum_{\alpha=1}^{N} \psi^\alpha(S, g; F^p, \gamma). \tag{3.53}$$

Next, we assume that the crystal obeys Schmidt's rule and write

$$\psi^\alpha = \psi^\alpha(\tau^\alpha - g^\alpha), \tag{3.54}$$

i.e., the slip system flow potential ψ^α depends on $(S, g; F^p, \gamma)$ solely through the corresponding resolved shear overstress $\tau^\alpha - g^\alpha$. In this context, g^α takes on the significance of the critical resolved shear stress for the activation of slip system α. Substitution of (3.53) and (3.54) into (3.48) and (3.49) gives

$$\dot{F}^p = \left(\sum_{\alpha=1}^{N} \frac{\partial \psi^\alpha}{\partial \tau^\alpha} s^\alpha \otimes m^\alpha \right) F^p \tag{3.55}$$

$$\dot{\gamma}^\alpha = -\frac{\partial \psi^\alpha}{\partial g^\alpha} = \frac{\partial \psi^\alpha}{\partial \tau^\alpha}. \tag{3.56}$$

Insertion (3.56) into (3.55) gives the standard crystallographic flow rule (3.50), as required.

3.3.3 Rate-independent behavior

In the particular case of a rate independent crystal, the slip system flow potential takes the form:

$$\begin{aligned} \psi^\alpha &= 0, && \text{if } \tau^\alpha - g^\alpha \leq 0 \\ &= \infty, && \text{otherwise.} \end{aligned} \tag{3.57}$$

Evidently, it follows from (3.52) that, for fixed $(g; F^p, \gamma)$, the elastic domain $K(F^p) = \{S \in R^{3\times 3} \; s.\; t.\; \tau^\alpha - g^\alpha < 0, \; \alpha = 1, \ldots, N\}$ when represented in (SF^{pT})-space is the

intersection of halfspaces and, therefore, is a convex set. Because of the orthogonality condition $s^\alpha \cdot m^\alpha$, it follows that, in (SF^{pT})-space, K is a cylinder coaxial with the hydrostatic axis. In view of (3.52), it is evident that the elastic domain depends on the current value of F^p, which may be regarded as a geometric effect. This illustrates the need for the explicit dependence $K(q)$ of the elastic domain on the internal variables allowed for in Section 3.2.3.

We now turn to the question of minimizing paths for single crystals. For a general plastic material, the incremental work of deformation per unit undeformed volume (3.13) takes the form

$$W = [\phi]_0^T + \int_0^T (S \cdot \dot{F}^p - g \cdot \dot{\gamma}) dt. \tag{3.58}$$

In the special case of single crystals, substitution of (3.50) into (3.58) gives

$$W = [\phi]_0^T + \int_0^T [(\tau - g) \cdot \dot{\gamma}] dt \tag{3.59}$$

where we have grouped all the resolved shear stresses into the array $\tau \in R^N$. Proceeding as in the preceding section, the stationarity condition is found to be

$$\delta W = \int_0^T [(\delta\tau - \delta g) \cdot \dot{\gamma} - (\dot{\tau} - \dot{g}) \cdot \delta\gamma] dt = 0. \tag{3.60}$$

In the rate-independent limit (3.60) reduces to

$$\int_0^T (\dot{\tau} - \dot{g}) \cdot \delta\gamma dt = 0 \tag{3.61}$$

which determines the minimizing deformation paths.

If $\tau^\alpha - g^\alpha < 0$ during $[t_1, t_2] \subset [0, T]$, which corresponds to elastic unloading of the system α, it follows that, necessarily, $\delta\gamma^\alpha = 0$ in that time interval and the corresponding term in (3.61) vanishes. Thus, as expected, all elastic paths are stationary. Suppose now that the crystal has at least five independent slip systems and that we confine our attention to volume preserving deformation histories. By material

frame indifference, we can further restrict our attention to pure stretch deformations $F(t) = U(t)$. This leaves five independent components of deformation. We shall assume that any arbitrary variation $\delta\gamma(t)$ in the slip activity at time t can be attained by a suitable choice of $\delta U(t)$. The variations $\delta\gamma(t)$ being arbitrary, (3.61) requires that $\dot{\tau}^\alpha - \dot{g}^\alpha = 0$ for the active systems. These requirements and the plastic irreversibility constraint (3.51) can be expressed compactly in Kuhn-Tucker form as

$$\tau^\alpha(t) - g^\alpha(t) \leq 0, \qquad \text{and} \quad \dot{\gamma}^\alpha(t) \geq 0, \qquad \text{and} \quad [\tau^\alpha(t) - g^\alpha(t)]\dot{\gamma}^\alpha(t) = 0 \tag{3.62}$$

for all slip systems $\alpha = 1, \ldots, N$, which are the optimality conditions for constrained variational problems ([Roc70]). It follows from the third of (3.62) and (3.59) that

$$W = [\phi]_0^T, \tag{3.63}$$

i. e., the work of deformation along a minimizing path in a rate-independent single crystal equals the change in free energy.

Next, we shall consider such paths as result from constant slip rates $\dot{\gamma}^\alpha$ over the time interval $[0, T]$ under consideration. The slip rates are subject to the plastic irreversibility constraint (3.51) and some of them may vanish identically over the time step. The working assumption is, therefore, that the pattern of slip activity, i. e., the active slip systems and relative slip rates, remains constant throughout the interval $[0, T]$. For these paths,

$$\gamma^\alpha(t) = (1 - t/T)\gamma^\alpha(0) + (t/T)\gamma^\alpha(T) \tag{3.64}$$

and the flow rule (3.50) integrates to

$$F^p(t) = \exp\left\{\sum_{\alpha=1}^{N}[\gamma^\alpha(t) - \gamma^\alpha(0)]s^\alpha \otimes m^\alpha\right\} F^p(0) \tag{3.65}$$

In particular,

$$F^p(\gamma(T); F^p(0), \gamma(0)) = \exp\left\{\sum_{\alpha=1}^{N}[\gamma^\alpha(T) - \gamma^\alpha(0)]s^\alpha \otimes m^\alpha\right\} F^p(0) \tag{3.66}$$

and the elastic right Cauchy-Green deformation tensor at T takes the form

$$C^e(\gamma(T), C(T); F^p(0), \gamma(0)) = F^{p-T}(\gamma(T); F^p(0), \gamma(0))C(T)F^{p-1}(\gamma(T); F^p(0), \gamma(0)) \tag{3.67}$$

where $C(T)$ is given. If, in addition, the path is minimizing, then the work of deformation follows from (3.63) and (3.44) in the form

$$W(\gamma(T), C(T); F^p(0), \gamma(0)) = \phi(C^e(\gamma(T); F^p(0), \gamma(0)), \gamma(T)) - \phi(0). \tag{3.68}$$

The terminal value $\gamma(T)$ of the slip strains then follows from the minimum problem:

$$W(C(T); F^p(0), \gamma(0)) = \min_{\substack{\gamma^\alpha(T)\geq\gamma^\alpha(0)\\ \alpha=1,\ldots,N}} W(\gamma(T), C(T); F^p(0), \gamma(0)). \tag{3.69}$$

Indeed, a trite calculation reveals that

$$\frac{\partial W(\gamma(T), C(T); F^p(0), \gamma(0))}{\partial \gamma(T)} = \tau(T) - g(T) \tag{3.70}$$

and, consequently, the Kuhn-Tucker optimality conditions corresponding to (3.69) are:

$$\tau^\alpha(T) - g^\alpha(T) \leq 0, \quad \text{and} \quad \gamma^\alpha(T) - \gamma^\alpha(0) \geq 0, \quad \text{and} \tag{3.71}$$

$$[\tau^\alpha(T) - g^\alpha(T)][\gamma^\alpha(T) - \gamma^\alpha(0)] = 0 \tag{3.72}$$

in accordance with (3.62).

Let $\mathcal{A}$ be the collection of systems that are active during the time increment.

Thus,

$$\gamma^\alpha(T) > \gamma^\alpha(0) \quad \text{if} \quad \alpha \in \mathcal{A} \tag{3.73}$$

$$\gamma^\alpha(T) = \gamma^\alpha(0) \quad \text{if} \quad \alpha \notin \mathcal{A}. \tag{3.74}$$

Once problem (3.69) has been solved for $\gamma(T)$, for given $C(T)$ and appropriate initial conditions, the plastic deformation gradient history $F^p(t)$, $t \in [0,T]$ follows from (3.64) and (3.65); $C^e(t)$ follows from the second of (3.44) in terms of the as yet unknown deformation history $C(t)$; $S(t)$ follows from (3.45) and (3.46); $\tau(t)$ from (3.52); $g(t)$ from (3.47) and (3.64); and, finally, the minimizing deformation history is any function $C(t)$, with $\det(C(t)) = 1$, satisfying the conditions:

$$\tau^\alpha(t) = g^\alpha(t) \quad \text{if} \quad \alpha \in \mathcal{A} \tag{3.75}$$

$$\tau^\alpha(t) < g^\alpha(t) \quad \text{if} \quad \alpha \notin \mathcal{A}, \tag{3.76}$$

provided that the *ansatz* (3.64) is correct and these constraints can indeed be simultaneously satisfied for all $t \in [0,T]$. It should be noted that constraints (3.75) and (3.76) are satisfied at $t = T$ by the choice of $\gamma(T)$, and the question is, therefore, if the slip pattern can indeed be kept unchanged throughout the deformation increment.

The preceding construction reduces the determination of the pseudoelastic energy density W for rate-independent single crystals to a conventional convex minimization problem for the slip strains. The nature of W is illustrated in subsequent sections for two important examples: crystals undergoing geometrical softening; and crystals exhibiting latent hardening. In both cases, the corresponding energy density W is found to be nonconvex. The particular well structure of W is subsequently taken as a basis for constructing energy-minimizing microstructures which agree remarkably well with observation.

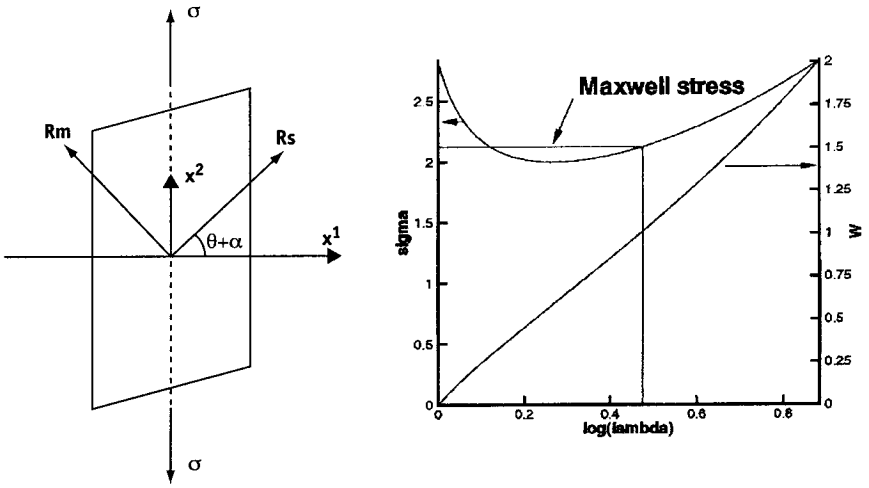

(a) (b)

Figure 3.2: a) Single crystal oriented for single slip loaded in uniaxial tension; b) stress-strain curve showing lack of convexity due to geometrical softening.

3.3.4 Geometrical softening

The deformation of single crystals may result in large lattice rotations and, correspondingly, in sizeable variations in the resolved shear stresses acting on the slip systems. Consider, for simplicity, the case of a crystal oriented for single slip. Under the appropriate conditions, the lattice rotations may sufficiently increase the resolved shear stress on the active slip system to cause the behavior of the crystal to turn unstable, a phenomenon known as geometrical softening [Asa83].

In order to illustrate the concept of geometrical softening and its relation to lack of convexity, we consider the case of single crystal oriented for single slip and loaded in uniaxial tension, Fig. 3.2a. To further simplify the problem, we shall neglect hardening and the elasticity of the crystal, i. e., we take $F^e = R \in SO(3)$, and assume that the axis of loading is contained within the plane defined by the slip direction s and the slip plane normal m. We chose a cartesian reference frame in which the (x_1, x_2)-plane coincides with the (s, m) plane and the x_2-axis is aligned with the loading axis. The crystal then deforms in plane strain within the (x_1, x_2)-plane and the axis of lattice

rotation is the x_3-axis. Let θ be the angle subtended by the initial slip direction s to the x_1 axis and let α be the angle of lattice rotation, so that

$$R = \begin{pmatrix} \cos\alpha & -\sin\alpha & 0 \\ \sin\alpha & \cos\alpha & 0 \\ 0 & 0 & 1 \end{pmatrix} \tag{3.77}$$

and

$$Rs = \begin{pmatrix} \cos(\theta+\alpha) \\ \sin(\theta+\alpha) \\ 0 \end{pmatrix}, \qquad Rm = \begin{pmatrix} -\sin(\theta+\alpha) \\ \cos(\theta+\alpha) \\ 0 \end{pmatrix} \tag{3.78}$$

The activation of the system requires

$$\tau = \sigma \sin(\theta+\alpha)\cos(\theta+\alpha) = g \tag{3.79}$$

where σ is the applied uniaxial stress and g is the constant critical resolved shear stress. The deformation gradient is

$$\begin{aligned} F &= R[I + \gamma s \otimes m] \\ &= \begin{pmatrix} \cos\alpha & -\sin\alpha & 0 \\ \sin\alpha & \cos\alpha & 0 \\ 0 & 0 & 1 \end{pmatrix} + \gamma \begin{pmatrix} -\cos(\theta+\alpha)\sin\theta & \cos(\theta+\alpha)\cos\theta & 0 \\ -\sin(\theta+\alpha)\sin\theta & \sin(\theta+\alpha)\cos\theta & 0 \\ 0 & 0 & 1 \end{pmatrix} \end{aligned} \tag{3.80}$$

Assuming that the specimen stretches under the action of fixed grips furnishes the kinematic constraint

$$F \begin{pmatrix} 0 \\ 1 \\ 0 \end{pmatrix} = \begin{pmatrix} 0 \\ \lambda \\ 0 \end{pmatrix} \tag{3.81}$$

where λ is a prescribed stretch ratio. Inserting (3.80) into (3.81) gives the identities

$$-\sin\alpha + \gamma\cos(\theta+\alpha)\cos\theta = 0, \qquad \cos\alpha + \gamma\sin(\theta+\alpha)\cos\theta = \lambda \tag{3.82}$$

From (3.79) and (3.82) we obtain

$$\sigma = \frac{g}{\sin(\theta+\alpha)\cos(\theta+\alpha)}, \quad \gamma = \frac{\sin\alpha}{\cos(\theta+\alpha)\cos\theta}, \quad \lambda = \cos\alpha + \frac{\sin\alpha\sin(\theta+\alpha)}{\cos(\theta+\alpha)} \tag{3.83}$$

parametrized in terms of α. The deformation power may be variously expressed as

$$\dot{W} = g\dot{\gamma} = \sigma\frac{d\log\lambda}{dt} \tag{3.84}$$

which shows that $W = g\gamma$.

The stress-strain curve of the crystal in terms of the work-conjugate variables $(\sigma, \log\lambda)$ can be obtained by eliminating α from the first and third of (3.83). The stress-strain curve and work density function $W(\log\lambda)$ corresponding to $\theta = \pi/8$ and $\alpha \in [0, \pi/4]$ are shown in Fig. 3.2b. The lack of convexity of the work energy function is evident from the figure. In particular, we note that the stress-strain curve has the familiar up-down-up form of one-dimensional models of displacive phase transitions in solids ([Eri80]; [Sil89]). The equilibrium solutions led to by these models are presently well understood ([TZ95]; [TZ96]) and, by analogy, we may expect crystals undergoing geometrical softening to develop fine microstructure. We shall return to this question in Section 3.5.2.

3.3.5 Latent hardening

Latent hardening tests ([Koc66]; [FBZ80]; [BW91a]; [BW91b]; [Koc64]; [RKC65]) have been widely used to investigate the hardening behavior of single crystals. In latent hardening experiments, the crystal is first oriented for single slip and loaded in uniaxial tension or compression. The crystal is subsequently cut into smaller

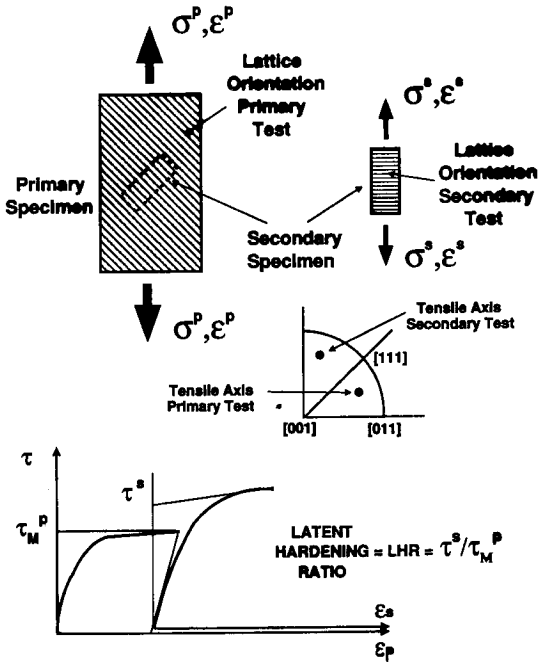

Figure 3.3: Schematic representation of latent hardening tests, showing primary and secondary loading phases and definition of the latent hardening ratio.

specimens which are rotated and re-loaded so as to activate a secondary system; see Fig. 3.3. This type of test enables a direct characterization of the hardening induced in secondary systems by plastic activity in the primary slip system, or latent hardening.

Latent hardening data is often reported in terms of the latent hardening ratio LHR$= \tau_s/\tau_p$, where τ_p and τ_s denote the critical resolved shear stresses on the primary and secondary slip system, respectively. The values of the critical resolved shear stresses are typically obtained from the stress-strain curve by backextrapolation. The experimental data [FBZ80] reveals that the LHR is a function of the prestrain γ_p on the primary system and the strength of the interaction between the primary and secondary systems. For well-annealed FCC crystals the LHR reduces to 1 as $\gamma_p \to 0$, as the initial critical resolved shear stress is the same in all systems. With increasing γ_p, the LHR goes through a maximum and then settles down to a nearly constant value.

The mechanisms underlying this dependence are noteworthy. In the prestraining

stage, the variation of τ_s is determined by dislocation multiplication on the primary system and the attendant increase in the density of point obstacles on the secondary slip planes. Thus, τ_s increases at a high rate typical of the stage II of hardening. By contrast, τ_p increases at a low rate characteristic of the stage I of hardening in crystals oriented for single slip. Consequently, at small prestrains τ_s attains values considerably in excess of τ_p and the LHR rises sharply. For large prestrains, the dislocation density on the primary system saturates and τ_s attains a nearly constant value. Concurrently, τ_p continues to grow slowly due to the self-hardening of the primary system, which results in a downturn in the LHR.

Crystals undergoing plastic deformation are often observed to develop domains of predominantly single slip ([BO54], [PCC55] [Sai63]), a mode of deformation which has been termed "patchy slip" [Asa83]. Several experimental observations of patchy slip are collected in Fig. 3.4. Piercy *et al.* [PCC55] attributed this nonuniform slip mode to latent hardening. They argued that "these results prove the reality of latent-hardening, in the sense that the slip lines of the one system experience difficulty in breaking through the active slip lines of the other one" ([PCC55], p. 337). This conjecture is born out by the bifurcation analysis and numerical simulations of Pierce *et al.* [PAN82]. Thus, Pierce *et al.* [PAN82] applied Hill and Hutchinson's bifurcation analysis [HH75] to Asaro's double-slip planar model of crystals [Asa79] and found that, for sufficiently strong latent hardening, the governing equations may change type from elliptic to parabolic. Pierce *et al.* [PAN82] reasoned that this transition marks the inception of patchy slip. Finite element simulations of specimens subjected to uniaxial tension carried out by Pierce *et al.* [PAN82] do indeed exhibit nonuniform slip patterns consisting of alternating regions of single slip on the primary and secondary systems.

It should be carefully noted, however, that bifurcation analyses of the Hill and Hutchinson type [HH75] are based on the incremental behavior of the solid–the "linear comparison solid" in Hill's parlance–and, consequently, are not fully nonlinear. This inevitably weakens the case for an unequivocal cause-and-effect relation between latent hardening and patchy slip. In subsequent sections, we carry out a nonlinear

(a)

(b)

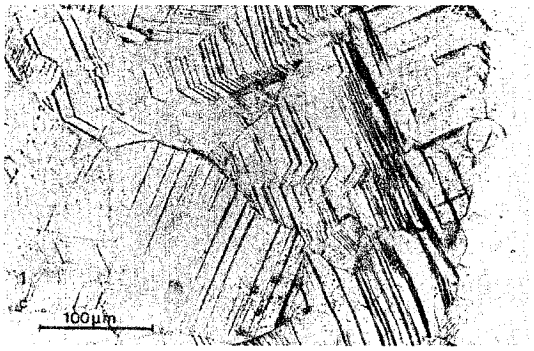

(c)

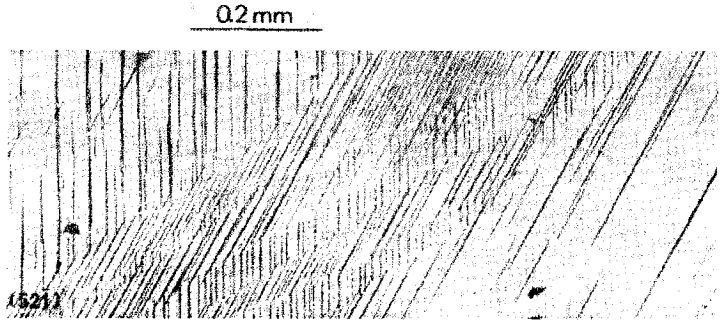

(d)

Figure 3.4: Instances of slip segregation into single-slip domains, or "patchy slip." a) From [BO54]; b) from [Sai63]; c) from [RP80]; d) from [JW84b].

analysis based on the energy minimization theory developed in the foregoing. Within this framework, the transition to patchy slip arises as a consequence of the lack of convexity of the energy function in the presence of latent hardening. The well structure of the pseudoelastic strain energy density suggests that crystals exhibiting latent hardening can reduce the work required to attain a prescribed average deformation by developing microstructures consisting of single-slip variants. Deformation structures based on this *ansatz* are constructed in subsequent sections.

In order to explicitly exhibit the relation between latent hardening, lack of convexity and patchy slip, we resort to a simple model of latent hardening. In particular, we seek a model with the following attributes:

1. Parabolic hardening in single slip: $g^\alpha(\gamma^\alpha) \sim \sqrt{\gamma^\alpha}$.

2. Off-diagonally dominant hardening matrix: $h^{\alpha\beta} > h^{\alpha\alpha}$, $\alpha, \beta = 1, \ldots, N$, $\beta \neq \alpha$, where $h^{\alpha\beta}(\gamma) = \partial g^\alpha / \partial \gamma^\beta$ is the hardening matrix.

These two requirements roughly reflect the phenomenology of latent hardening summarized above. Evidently, the assumption of parabolic hardening can be trivially generalized to an arbitrary power-law dependence of g^α on γ^α, but this generalization will not be pursued here. Begin by assuming an additive decomposition of the free energy of the form

$$\phi = W^e(C^e) + W^p(\gamma) \tag{3.85}$$

Implicit in this decomposition is the assumption that the elastic response of the solid, e.g., upon unloading, is not affected by internal processes, which is a good first approximation for metals. We further suppose that W^e is quasiconvex, which rules out purely elastic microstructures, and that $W^e \geq 0$ and $W^e(I) = 0$. For free energies of the form (3.85), the hardening relations and hardening matrix are

$$g^\alpha = \frac{\partial W^p(\gamma)}{\partial \gamma^\alpha}, \qquad h^{\alpha\beta} = \frac{\partial^2 W^p(\gamma)}{\partial \gamma^\alpha \partial \gamma^\beta}. \tag{3.86}$$

A class of functions $W^p(\gamma)$ which conforms to the requirements stated above is

$$W^p = \frac{2}{3}\tau_0\gamma_0 \left[\sum_{\alpha=1}^{N}\sum_{\beta=1}^{N} a^{\alpha\beta}\frac{\gamma^\alpha}{\gamma_0}\frac{\gamma^\beta}{\gamma_0}\right]^{3/4} \tag{3.87}$$

where τ_0 and γ_0 are a reference resolved shear stress and slip strain, respectively, and $a^{\alpha\beta}$ are interaction coefficients.

Experimentally determined values of the matrix $a^{\alpha\beta}$ have been given by Franciosi and Zaoui [FZ82] for FCC and BCC crystals. They classify the interactions between systems according to whether the dislocations belong to the same system (interaction coefficient a_0), fail to form junctions (interaction coefficient a_1), form Hirth locks (interaction coefficient a_1), co-planar junctions (interaction coefficient a_1), glissile junctions (interaction coefficient a_2), or sessile Lomer-Cottrell locks (interaction coefficient a_3), with $a_0 \leq a_1 \leq a_2 \leq a_3$. These order relations give an off-diagonally dominant hardening matrix $h^{\alpha\beta}$ as required. For copper, a fit to the experimental data gives $a_1/a_0 = 5.7$, $a_2/a_0 = 10.2$, $a_3/a_0 = 16.6$ [CnO92].

A simple geometrical model for the interaction matrix $a^{\alpha\beta}$ has been proposed by Cuitiño and Ortiz [CnO93]. The model is based on counting the number of forest dislocation intersections per unit area of the slip plane, which gives the density of point obstacles. A trite calculation gives

$$a^{\alpha\beta} = \frac{2}{\pi}\sqrt{1-(m^\alpha \cdot m^\beta)^2}. \tag{3.88}$$

In this simple model the slip systems do not self-harden. Indeed, typical resolved shear stresses required to deform a well-annealed crystal in single slip tend to be small compared to those required for multiple slip and, for purposes of understanding the morphology of dislocation structures, they can conveniently and expeditiously be neglected to a first approximation. The relation (3.88) was used by Cuitiño and Ortiz [CnO93] – in lieu of more detailed experimental data – to describe the hardening of Ni_3Al single crystals.

The form of the pseudoelastic strain energy density (3.69) predicted by the model

is of particular interest. Begin by considering a deformation increment from a previously undeformed state, i. e., set $F^p(0) = I$, $\gamma(0) = 0$. From (3.59), (3.85), (3.87) and the assumed properties of W^e, it is clear that $W \geq 0$. In addition, owing to the lack of self-hardening in model (3.88), one has $W(F(T)) = 0$ for any terminal deformation of the form

$$F(T) = R(T)F^p(T), \qquad F^p(T) = I + \gamma^\alpha(T)s^\alpha \otimes m^\alpha, \tag{3.89}$$

i.e., for deformations consisting of single slip followed by an arbitrary lattice rotation $F^e = R \in SO(3)$. Indeed, from the first of (3.89), one has $C^e(T) = I$ and, consequently, $W^e(C^e(T)) = 0$ by the assumed properties of W^e. Additionally, $W^p = 0$ as a consequence of the approximation $a^{\alpha\alpha} = 0$. It therefore follows that *all single-slip deformations constitute "wells,"* or local minima, of the incremental strain energy density W of previously undeformed crystals exhibiting latent hardening. In particular, the energy density W is *nonconvex*, which foreshadows the development of fine microstructures.

To exhibit more explicitly the well structure induced by latent hardening, we consider the simple case of a well-annealed FCC crystal deforming in plane strain within the plane determined by the directions [101] and [010]; see Fig. 3.5a. The normal to this plane is in the $[\bar{1}01]$ direction. Combinations of slip systems which result in plane-strain deformations with this geometry are the pair (111) $[1\bar{1}0]$ and (111) $[0\bar{1}1]$, which jointly gives rise to effective in-plane shear along the $[1\bar{2}1]$ direction; see Fig. 3.5a. Similarly, the systems $(1\bar{1}1)$ [110] and $(1\bar{1}1)$ [011] combine to produce effective in-plane slip along the [121] direction. Finally, the joint operation of the pair of systems $(11\bar{1})$ [101] and $(\bar{1}11)$ [101] also results in the in-plane effective system (010) [101]. By material frame indifference and incompressibility (not considering the elastic compressibility), there are only two independent deformation components, which may be chosen to be $(\epsilon_{11} - \epsilon_{22})$ and ϵ_{12}, where $\epsilon = \log U$ is the logarithmic strain tensor. The corresponding energy function W is displayed in Fig. 3.5b. The lack of convexity of W is immediately apparent. A section of W along a circle $\| \epsilon \| = const.$

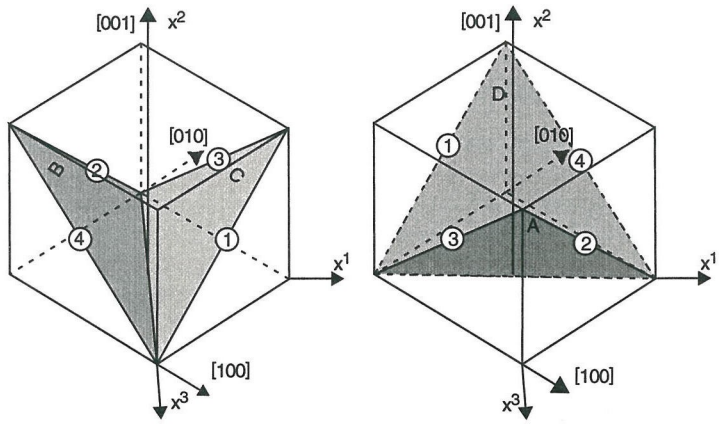

(a) (b)

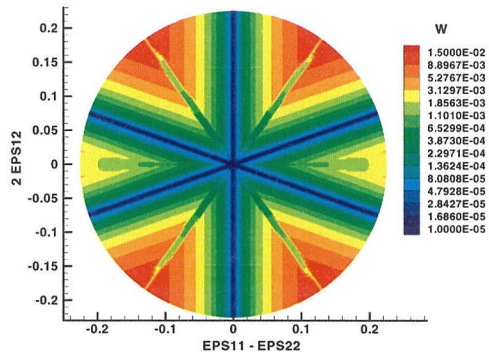

(c)

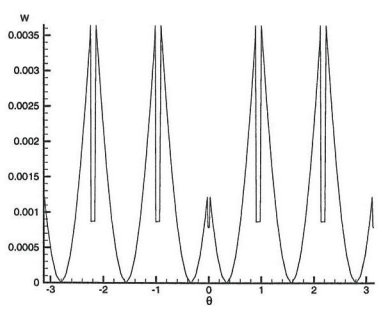

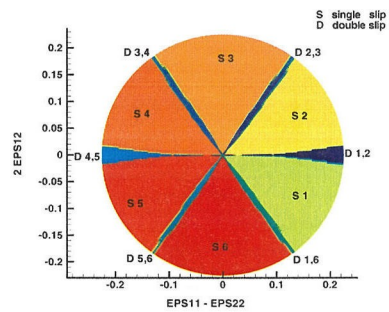

(d) (e)

Figure 3.5: a,b) Crystal orientation leading to plain strain deformation and active slip systems; c) pseudoelastic energy density revealing nonconvexity induced by latent hardening; d) $W(ro, \theta)$, with $0 \leq \theta < 2\pi$; e) active slip systems.

centered at the origin exhibits multiple minima, or "wells," corresponding to single-slip deformation modes. As noted earlier, due to the lack of self-hardening in the model, W vanishes identically at these minima.

Next, consider the incremental deformations over a time interval $[0, T]$ of a crystal that has been prestrained in single slip. In this case,

$$F(0) = R(0)F^p(0), \qquad F^p(0) = I + \gamma^\alpha(0)s^\alpha \otimes m^\alpha \tag{3.90}$$

for some slip system α. Evidently, terminal deformations $F(T)$ requiring the activation of a secondary system inevitably induce latent hardening and, consequently, lead to a $W > 0$. By contrast, a terminal deformation of the form (3.89), resulting from the continuing activation of the prestrained slip system, gives $W = 0$. Therefore, the only energy well available to a crystal prestrained in single corresponds to further single-slip on the prestrained slip system. This reduction in the number of wells due to prestraining in single slip may be regarded as a "training" of the crystal, which is subsequently conditioned to prefer a specific single slip for further deformation. We shall refer to deformation histories of form

$$F(t) = R(t)F^p(t), \qquad F^p(t) = I + \gamma^\alpha(t)s^\alpha \otimes m^\alpha \tag{3.91}$$

as "persistent single slip." Note that the slip-strain history $\gamma^\alpha(t)$ is allowed to be arbitrary and, in particular, may exhibit cycles in the $\pm s^\alpha$ directions such as occur in fatigued single crystals. From the above results, it follows that the incremental energy densities W corresponding to any interval (t_1, t_2) of a history of persistent single slip vanish identically.

3.4 Dislocation structures

The models of geometrical softening and latent hardening developed in the preceding sections lead to nonconvex incremental energy densities. Under these conditions, uniform deformation fields are not minimizers of (3.38) in general. Thus, consider a

macroscopic neighborhood Ω of a ductile single crystal subject to affine displacement boundary conditions of the form (3.35). Then, the crystal can generally do better in energetic terms than to deform uniformly over Ω by exploiting the well structure of the incremental strain energy density W.

For crystals exhibiting latent hardening, the results given in the preceding section show that uniform deformations consisting of persistent single slip are incremental energy minimizers. This suggests a strategy for constructing more general approximate energy minimizers over Ω, namely, to seek compatible deformation fields satisfying (3.35) which consist locally of persistent single slip, i. e., which are of the form

$$F_\epsilon(x,t) = R_\epsilon(x,t)F^p_\epsilon(x,t) \tag{3.92}$$

$$F^p_\epsilon(x,t) = I + \gamma_\epsilon(x,t)s_\epsilon(x) \otimes m_\epsilon(x), \qquad (s_\epsilon(x), m_\epsilon(x)) \in \mathcal{S} \tag{3.93}$$

over a subset $\Omega_\epsilon \subset \Omega$. Note that this is strictly a problem of compatibility. The reason for not insisting on persistent single slip *almost everywhere* in Ω is that compatibility of deformations, e.g., at the boundary, will in general require the introduction of boundary layers involving complex slip patterns and elastic strains. However, we expect that the measure $|\Omega - \Omega_\epsilon|$ can be made arbitrarily small by refining the microstructure. If, in addition, the energy density remains bounded almost everywhere, it follows that the sequence $F^{(j)}(x,t) = F_{1/j}(x,t)$ defines an incremental energy minimizing sequence.

A fundamental question concerns which average deformation histories $\bar{F}(t)$ can be accommodated by the microstructures just described. It is clear that, for any such deformation history, the crystal is trained into a pattern of local persistent single slip early on, and subsequent average deformations must be compatible with the established microstructure. Within the framework of linearized kinematics, a plausible conjecture is that, for crystals possessing a sufficiently rich set $\mathcal{S}$ of slip systems, e.g., five or more independent slip systems, incremental energy minimizing sequences of persistent single slip exist for any history of volume-preserving average

deformation gradients of the form

$$\bar{F}(t) = I + f(t)\bar{G} \tag{3.94}$$

where $f(t)$ is any absolutely continuous function of time in the interval $[0, T]$, and $\bar{G}$ is a constant traceless matrix. A plausibility argument supporting this conjecture is given in Section 3.4.3. The linearized kinematics framework is particularly relevant in high-cycle fatigue, where typical deformation amplitudes are of the order of 10^{-3}. Indeed, many of the examples of microstructures given in Section 3.5 pertain to high-cycle fatigue of single crystals and polycrystals.

So far we have formulated the problem of microstructural development in ductile single crystals in terms of compatible deformation fields $F(x, t)$, and the mathematical description of dislocation structures has not as yet been addressed. However, the connection between deformation and dislocation structures is readily made. Thus, while $F(x, t)$ must be compatible, i. e., it must be a gradient for all $t \in [0, T]$ in some suitable weak sense, the plastic deformation field $F^p(x, t)$ is not subject to any such requirement. Physically, the incompatibility of $F^p(x, t)$ represents a distribution of dislocations within the crystal. To see this, let Γ be a smooth closed circuit inscribed within the undeformed crystal, or Burgers circuit. Owing to the incompatibility of F^p, the vector

$$b(\Gamma) = \oint_{\Gamma} F^p \cdot dx \tag{3.95}$$

is not zero in general but amounts to the vector sum of the undeformed or true Burgers vectors of all dislocations encircled by Γ. Let Σ be any smooth surface bordering on Γ. Then, by Stokes theorem,

$$b(\Gamma) = \int_{\Sigma} (F^p \times \nabla) \cdot N dS \tag{3.96}$$

where N is the unit normal to Σ and dS is the element of area. Following Nye

([Nye53]; see also [Mur87]), the dislocation density tensor is defined as

$$A = F^p \times \nabla \tag{3.97}$$

whereupon (3.96) can be rewritten as

$$b(\Gamma) = \int_\Sigma A \cdot N dS. \tag{3.98}$$

It is evident from (3.97) that A is a measure of the incompatibility of $\mathbf{F}^p$ and that, from a continuum perspective, dislocations are inextricably related to incompatibility. A direct consequence of definition (3.97) is that

$$A \cdot \nabla = 0. \tag{3.99}$$

This identity embodies the physical requirement that dislocation lines cannot end abruptly in the interior of the crystal. Indeed, if the surface Σ in (3.96) is closed, then an application of the divergence theorem and (3.99) shows that the net Burgers vector flux through the surface is zero, as required. Identity (3.99) also embodies Frank's rule for dislocation reactions.

The dislocation density tensor corresponding to a single dislocation line supported on a curve C in Ω is

$$A(x) = b \otimes t(x)\delta_C(x) \tag{3.100}$$

where b is the Burgers vector of the dislocation, t is the unit tangent to C and δ_C is the Dirac-delta supported on C. Another noteworthy special case is that of continuously distributed parallel dislocations, for which

$$A = \rho b \otimes t \tag{3.101}$$

where ρ is the dislocation length per unit volume.

It follows from the fundamental relation (3.97) that representation (3.92) and (3.93) describes not only deformation microstructures but dislocation microstructures as well. However, it bears emphasis that the present approach is at variance with investigations of low energy dislocation structures which regard the dislocation density tensor A, e.g., representing an ensemble of discrete dislocations, as the primary field, and seek to minimize the long-range stresses–or the corresponding elastic strain energy–induced by A. By contrast, in the present approach F^p is the primary unknown field and A derives from it through (3.97). In particular, the dislocation distribution is consistent with a history of plastic slip in the crystal. In addition, long-range stresses are absent from the crystal by construction, as the elastic deformation F^e is required to be locally a rotation.

3.4.1 Dislocation walls

In this and subsequent sections, we proceed to describe some simple structures of the form (3.92) and (3.93), namely, interfaces and laminates. Despite their simplicity, these structures suffice to explain a number of experimental observations, as demonstrated in Section 3.5.

We begin by characterizing all possible planar interfaces separating two uniformly deformed regions of the crystal undergoing single slip. By analogy to the crystallographic theory of martensite, we shall refer to each of the regions separated by the interface as variants. The deformations of the variants are, therefore,

$$F^{\pm}(t) = R^{\pm}(t)(I + \gamma^{\pm}(t)s^{\pm} \otimes m^{\pm}), \quad (s^{\pm}, m^{\pm}) \in \mathcal{S}, \quad t \in [0, T] \tag{3.102}$$

where the labels $\pm$ refer to the plus and minus sides of the interface as determined by the unit normal N. The active systems in each of the variants are assumed to remained unchanged throughout the deformation. For definiteness we shall further suppose that the crystal is initially undeformed, i. e.,

$$R^{\pm}(0) = I, \qquad \gamma^{\pm}(0) = 0 \tag{3.103}$$

and we shall require the functions $R^{\pm}(t)$ and $\gamma^{\pm}(t)$ to be absolutely continuous. In particular, we rule out unphysical discrete jumps in either the lattice rotations or the slip strains.

Compatibility across the interface demands

$$[\![F]\!] = F^+ - F^- = [\![y_{,N}]\!] \otimes N \tag{3.104}$$

The rotation R^- can be set to the identity without loss of generality. Then, R^+ may be regarded as the rotation of the $(+)$ variant relative to the $(-)$ variant. In addition, the slip strain γ^- may conveniently be utilized to parametrize the motion instead of time. Then, the compatibility condition (3.104) must be satisfied for all values of γ^-. Eq. (3.104) imposes four constraints on $[\![F]\!]$, namely, that the determinant and the three principal minors of $[\![F]\!]$ vanish identically. Thus, for fixed γ^-, (3.104) defines a system of four nonlinear equations in the four unknowns γ^+, R^+. The problem is, therefore, to find all solutions (γ^+, R^+) of this system of equations.

Of particular interest is the dislocation structure attendant to an interface. As noted in the foregoing, while the deformation gradients F are required to be compatible at the interface in the sense of (3.104), the plastic deformations need not be compatible in general, and the incompatibility of F^p is equivalent to a dislocation distribution of density (3.97). For interfaces, and application of (3.97) in a distributional sense, gives

$$A(x) = -[\![F^p]\!] \times N\delta_{\Pi}(x) \tag{3.105}$$

where Π is the plane of the interface and δ_{Π} is the Dirac-delta supported on Π. As expected, the dislocations are confined to the interface and form a two-dimensional dislocation array. In the special case of variants undergoing single slip,

$$A(x) = [\![\gamma s \otimes m]\!] \times N\delta_{\Pi}(x) \tag{3.106}$$

$$= (\gamma^+ s^+) \otimes (N \times m^+)\delta_{\Pi}(x) - (\gamma^- s^-) \otimes (N \times m^-)\delta_{\Pi}(x) \tag{3.107}$$

A comparison of this density and (3.101) reveals that the dislocation wall comprises two bundles of parallel dislocations of line density, Burgers vector and direction

$$\rho^{\pm} = \frac{\gamma^{\pm}}{b}\delta_{\Pi}(x), \qquad b^{\pm} = bs^{\pm}, \qquad t^{\pm} = N \times m^{\pm} \tag{3.108}$$

respectively. In (3.108), b is the magnitude of the Burgers vector. The dislocation density tensor can alternatively be computed from the jump in elastic part $\mathbf{F}^e$ of the deformation gradient. Thus, inserting (3.41) into (3.105) and using (3.104) leads to

$$A(x) = ([\![F^{e-1}]\!]F^{+}) \times N\delta_{\Pi}(x) = ([\![F^{e-1}]\!]F^{-}) \times N\delta_{\Pi}(x) \tag{3.109}$$

In the absence of long-range stresses, $\mathbf{F}^{e\pm} = \mathbf{R}^{\pm} \in SO(3)$, and one has

$$A(x) = ([\![R^{T}]\!]F^{+}) \times N\delta_{\Pi}(x) = ([\![R^{T}]\!]F^{-}) \times N\delta_{\Pi}(x) \tag{3.110}$$

which shows that the dislocation density tensor is related to the misorientation $[\![R^T]\!]$ of the variants.

Two-dimensional dislocation arrangements of the type just described have been variously termed dislocation boundaries and dislocation walls. Dislocation arrays are often used as mathematical representations of grain boundaries [HL68], but here the emphasis is on dislocation boundaries composed solely of glide dislocations. Because the walls contain dislocations belonging to two different slip systems, they are commonly termed dipolar walls. Planar dislocation walls of well-defined crystallographic orientations are often observed, e.g., as part of the labyrinth structures which develop in cyclically deformed crystals oriented for multiple slip ([AKLM84]; [Cha81]; [MB82]; [BBT85]; [JW84a]; [LVD86]); and in the "fence" structures observed during the early stages of stage II of hardening in FCC crystals [Ste66]. Specific examples of dislocation walls observed in FCC crystals are presented in Section 3.5.

It has been long known (see, e.g., [Nab67]) that certain infinite dislocation walls do not induce long-range elastic stresses in the crystal and, consequently, constitute low-energy dislocation structures. Not surprisingly, therefore, those dislocation walls

turn up ubiquitously as energy minimizers in numerical simulations of ensembles of discrete dislocations ([Neu86]; [LBN93]). In the present theory, the dislocation walls which are devoid of long-range stresses are precisely those for which $F^{e\pm} = R^{\pm} \in SO(3)$, as posited in (3.102). However, it should be carefully noted that the precise crystallographic nature of dislocation walls which is observed experimentally does not necessarily follow by simple minimization of the interaction energy of discrete dislocations, but, as demonstrated in Section 3.5.1, requires the additional kinematical assumption of persistent single slip in the variants.

The enforcement of compatibility at the interface in incremental or eulerian form proves useful in the analysis of certain interfaces. Let

$$l = \nabla v = \dot{F} F^{-1} \tag{3.111}$$

be the spatial velocity gradient. For persistent single slip on both sides of the interface, a straightforward calculation gives

$$l^{\pm} = \dot{\gamma}^{\pm} (R^{\pm} s^{\pm}) \otimes (R^{\pm} m^{\pm}) + \dot{R}^{\pm} (R^{\pm})^{-1}. \tag{3.112}$$

Evidently, $l^{\pm}$ represent the superposition of incremental slip on the rotated systems $(R^{\pm} s^{\pm}, R^{\pm} m^{\pm})$ and incremental lattice rotations $\dot{R}^{\pm} (R^{\pm})^{-1}$. In a spatial setting, the compatibility condition (3.104) becomes

$$[\![l]\!] = l^{+} - l^{-} = [\![v_{,n}]\!] \otimes n \tag{3.113}$$

where n represents the current unit normal to the plane of discontinuity. For volume-preserving deformations, it follows that $\mathrm{tr}(l^{\pm}) = 0$, which in view of (3.113) necessitates

$$[\![v_{,n}]\!] \cdot n = 0. \tag{3.114}$$

The relation between $([\![y_{,N}]\!], N)$ and $([\![v_{,n}]\!], n)$ follows simply by inserting (3.111)

into (3.113), with the result

$$[\![v_{,n}]\!] = \| (F^-)^{-T} N \| ([\![\dot{y}_{,N}]\!] - \dot{F}^+ (F^+)^{-1} [\![y_{,N}]\!]), \qquad n = \frac{(F^-)^{-T} N}{\| (F^-)^{-T} N \|}. \tag{3.115}$$

For variants undergoing single slip, insertion of (3.112) into (3.113) gives

$$\dot{\gamma}^+ (R^+ s^+) \otimes (R^+ m^+) + \dot{R}^+ (R^+)^{-1} - \dot{\gamma}^- s^- \otimes m^- = [\![v_{,n}]\!] \otimes n. \tag{3.116}$$

The instantaneous lattice rotation may be eliminated by decomposing (3.116) into symmetric and skewsymmetric parts, with the result

$$\mathrm{sym}([\![v_{,n}]\!] \otimes n) = \dot{\gamma}^+ \mathrm{sym}[(R^+ s^+) \otimes (R^+ m^+)] - \dot{\gamma}^- \mathrm{sym}(s^- \otimes m^-) \tag{3.117}$$

$$\mathrm{skw}([\![v_{,n}]\!] \otimes n) = \dot{\gamma}^+ \mathrm{skw}[(R^+ s^+) \otimes (R^+ m^+)] + \dot{R}^+ (R^+)^{-1} - \dot{\gamma}^- \mathrm{skw}(s^- \otimes m^-). \tag{3.118}$$

Here

$$\mathrm{sym} A_{ij} = \frac{1}{2}(A_{ij} + A_{ji}), \qquad \mathrm{skw} A_{ij} = \frac{1}{2}(A_{ij} - A_{ji}) \tag{3.119}$$

signify the symmetric and skewsymmetric components of a tensor A.

It therefore follows that a necessary condition for compatibility is that the left-hand side of (3.117) be the symmetric part of a traceless rank-one tensor. It is a simple matter to verify that a traceless symmetric second-order tensor over R^3 is the symmetric part of a traceless rank-one tensor iff its determinant vanishes. To see this, let $A = \mathrm{sym}(a \otimes n)$, with $a \cdot n = 0$. Clearly, $A(a \times n) = 0$, which shows that A is singular and, consequently, its determinant is zero. Conversely, let $\det(A) = 0$. Since, in addition, $\mathrm{tr}(A) = 0$ by assumption, the eigenvalues of A are of the form $\{-\gamma/2, \gamma/2, 0\}$ for some $\gamma \in R$. Let $\{e_1, e_2, e_3\}$ be the corresponding eigenvectors and set $a = \gamma s$, $s = (e_2 \pm e_1)/\sqrt{2}$, $m = (e_2 \mp e_1)/\sqrt{2}$. Then, $\mathrm{sym}(a \otimes m) = -(\gamma/2) e_1 \otimes e_1 + (\gamma/2) e_2 \otimes e_2 = A$, which completes the proof. It follows from this derivation that the symmetric part of a traceless rank-one tensor may be regarded as

the small-strain tensor corresponding to an infinitesimal slip strain γ on the plane of normal m in the direction s. It should be carefully noted that there are two equivalent representations of A obtained by exchanging the roles of s and m.

An application of this result to (3.117) yields the condition

$$\det\{\dot{\gamma}^{+}\mathrm{sym}[(R^{+}s^{+})\otimes(R^{+}m^{+})]-\dot{\gamma}^{-}\mathrm{sym}(s^{-}\otimes m^{-})\}=0 \tag{3.120}$$

which, after some trite algebra, reduces to the equation

$$\begin{aligned}[R^{+}s^{+},R^{+}m^{+},s^{-}][R^{+}s^{+},R^{+}m^{+},m^{-}]\dot{\gamma}^{+}=\\ [s^{-},m^{-},R^{+}s^{+}][s^{-},m^{-},R^{+}m^{+}]\dot{\gamma}^{-}\end{aligned} \tag{3.121}$$

where $[a,b,c]=(a\times b)\cdot c$ is the triple product. The infinitesimal lattice rotation $\dot{R}^{+}(R^{+})^{-1}$ can be determined from (3.118) as follows. Let $(-\dot{\gamma}/2,\dot{\gamma}/2,0)$ be the eigenvalues and (e_1,e_2,e_3) the eigenvectors of $\{\dot{\gamma}^{+}\mathrm{sym}[(R^{+}s^{+})\otimes(R^{+}m^{+})]-\dot{\gamma}^{-}\mathrm{sym}(s^{-}\otimes m^{-})\}$. Then,

$$[\![v_{,n}]\!]=\dot{\gamma}(e_2\pm e_1)/\sqrt{2} \tag{3.122}$$

$$n=(e_2\mp e_1)/\sqrt{2} \tag{3.123}$$

and it follows from (3.118) that

$$\begin{aligned}\omega^{+} &\equiv \dot{R}^{+}(R^{+})^{-1}\\ &= \pm\mathrm{skw}([\![v_{,n}]\!]\otimes n)-\\ &\qquad \dot{\gamma}^{+}\mathrm{skw}[(R^{+}s^{+})\otimes(R^{+}m^{+})]+\dot{\gamma}^{-}\mathrm{skw}(s^{-}\otimes m^{-}).\end{aligned} \tag{3.124}$$

We shall refer to interfaces such that

$$\begin{aligned}&[R^{+}s^{+},R^{+}m^{+},s^{-}][R^{+}s^{+},R^{+}m^{+},m^{-}]\neq 0,\quad \text{and}\\ &[s^{-},m^{-},R^{+}s^{+}][s^{-},m^{-},R^{+}m^{+}]\neq 0\end{aligned} \tag{3.125}$$

as "nondegenerate" interfaces. Assuming that the nondegeneracy condition (3.125) holds for $t \in [0, T]$ and that $\gamma^-(t)$ is given, then eqs. (3.121), (3.124) and the initial conditions (3.103) define an initial value problem for $\gamma^+(t)$ and $R^+(t)$. This problem has two solutions, or branches, depending on the choice of sign in eq. (3.124). In degenerate cases eq. (3.121) is trivially satisfied and the geometry of the interfaces cannot be determined incrementally. Instead, the jump condition (3.104) must be enforced directly.

3.4.2 Simple laminates

Simple laminates reveal useful insights into commonly observed deformation structures and furnish the basic building block for recursive lamination. Let L be a characteristic dimension of the domain Ω of the crystal and let $l \ll L$, $\epsilon = l/L \ll 1$. Define the characteristic functions $\chi_\epsilon^\pm(\xi) : [0, l) \to R$ of the variants as

$$\chi_\epsilon^+(\xi) = \begin{cases} 0, & \text{if } \xi \in [0, \nu^- l); \\ 1, & \text{if } \xi \in [\nu^- l, l), \end{cases} \tag{3.126}$$

$$\chi_\epsilon^-(\xi) = 1 - \chi_\epsilon^+(\xi) \tag{3.127}$$

with $\nu^- \in [0, 1]$. Next extend these functions to the whole real line by periodicity. In addition, let $\nu^+ = 1 - \nu-$, so that $\nu^+ + \nu^- = 1$. Next, consider two deformation histories $F^\pm(t)$ of the form (3.102) satisfying the jump condition (3.104). Pairs of deformations of this form are exhaustively classified for FCC crystals in Section 3.5. Then, the corresponding laminate of layer thickness l and volume fractions $\nu^\pm$ is characterized by deformation gradients, rotations and plastic deformations of the

form

$$F_\epsilon(x,t) = \chi_\epsilon^+(x\cdot N)F^+(t) + \chi_\epsilon^-(x\cdot N)F^-(t) \tag{3.128}$$

$$F_\epsilon^e(x,t) = \chi_\epsilon^+(x\cdot N)R^+(t) + \chi_\epsilon^-(x\cdot N)R^-(t) \tag{3.129}$$

$$F_\epsilon^p(x,t) = \chi_\epsilon^+(x\cdot N)(I+\gamma^+(t)s^+\otimes m^+) + \chi_\epsilon^-(x\cdot N)(I+\gamma^-(t)s^-\otimes m^-) \tag{3.130}$$

respectively. By construction, this deformation field is weakly compatible and, consequently, there is a continuous displacement field $y(x,t)$ whose gradient is $F(x,t)$ almost everywhere. The average deformation in the laminate is

$$\bar{F}(t) = \nu^+F^+(t) + \nu^-F^-(t) \tag{3.131}$$

which is independent of ϵ. The dislocation structure corresponding to laminates consists of an array of parallel dislocation walls of the type (3.105), i. e.,

$$A(x,t) = \sum_{k=1}^{\infty}[\![\gamma(t)s\otimes m]\!]\times N[\delta(x\cdot N - kl) - \delta(x\cdot N - (\nu^- + k)l)]. \tag{3.132}$$

Periodic arrays of dislocation walls of this type are very frequently found in FCC crystals, *cf.* Section 3.5.

Now let the crystal be subject to affine boundary conditions (3.35) with $\bar{F}(t)$ given by (3.131). Clearly, the deformation field (3.128) is not affine at the boundary and, consequently, fails to be strictly compatible with $\bar{F}$. Following [BJ87], compatibility can be restored by the introduction of a narrow boundary layer of thickness l. The details of the construction of the boundary layer may be found in [BJ87]. Let Ω_ϵ consist of Ω with the boundary layer excluded. Then, by construction, the restriction of F_ϵ to Ω_ϵ is of the form (3.128) and the incremental energy density W remains bounded within the boundary layer as $\epsilon\to 0$, which ensures that $F^{(j)} = F_{1/j}$ defines an incremental energy minimizing sequence.

3.4.3 Sequential lamination

From a macroscopic viewpoint, lamination effectively enriches the class of average deformation histories which are incremental energy minimizers, from the original class of persistent single slip histories (3.91) to deformation histories of the form (3.128). This process of enrichment may be continued recursively, leading to the definition of sequentially laminated microstructures. Treatments of sequential lamination may be found in [Koh91], [Bha91], [Bha92], [KS86] and [Ped93]. Experimental evidence of possible sequential lamination in FCC crystals is presented in Section 3.5.

Uniform deformations may conventionally be categorized as rank-zero laminates. Laminates of rank one have been explicitly defined in Section 3.4.2. Following Kohn [Koh91], a laminate of rank-r is a layered mixture of two rank-$(r-1)$ laminates, which affords an inductive definition of laminates of any rank. As noted by Kohn [Koh91], the construction of sequential laminates assumes a separation of scales: the length scale l_r of the rth-rank layering satisfies $l_r \ll l_{r-1}$.

Evidently, sequential laminates have a binary tree structure. The nodes of the tree are occupied by deformations histories $F_i(t)$, $i = 1, \ldots, n$, where n is the number of nodes, or order, of the tree. The root deformation is the average deformation history $\bar{F}(t)$. Each node in the tree has either two children or none at all. Nodes with a common parent are called siblings. Nodes without children are called leaves. Nodes which are not leaves are said to be internal. The deformation histories of the children of node i will be denoted $F_i^{\pm}(t)$. Each generation is called a level. The root occupies level 0 of the tree. The number of levels is the rank r of the tree. Level l contains at most 2^l nodes. The example in Fig. 3.6a represents a rank-three laminate of order eleven. The leaves of the tree are nodes 6 to 11. The children of, e.g., node 2 are nodes 4 and 5, with $F_2^-(t) = F_4(t)$ and $F_2^+(t) = F_5(t)$. The sequential laminate defined by the tree is shown in Fig. 3.6b.

The deformation history $F_i(t)$ of an internal node i is an average of the deformation

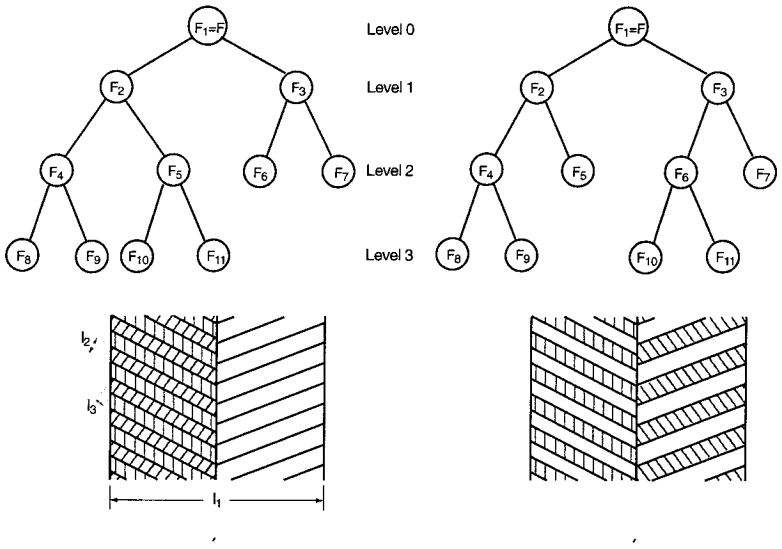

(a) (b)

Figure 3.6: Two sequential laminates with nine kinematical degrees of freedom.

histories $F_i^{\pm}(t)$ of its children, i. e.,

$$F_i(t) = \nu_i^-(t)F_i^-(t) + \nu_i^+(t)F_i^+(t), \qquad \nu_i^-(t) + \nu_i^+(t) = 1. \tag{3.133}$$

It therefore follows that the deformation history $F_i(t)$ of an l-level node is the average deformation history of a $(r-l)$-rank laminate. Additionally, siblings must be rank-one compatible, i. e.,

$$F_i^+(t) - F_i^-(t) = a_i(t) \otimes N_i(t), \qquad |N_i(t)| = 1. \tag{3.134}$$

We shall say that a sequential laminate is "persistent" if the interface normals N_i and volume fractions $\nu_i^{\pm}$ are independent of time. In addition, we shall say that a sequential laminate undergoes persistent single slip if it is persistent and the deformation histories of all of its leaves are of the form (3.91).

Sequential lamination furnishes a plausibility argument in support of conjecture (3.94). We begin by considering a time-independent average deformation gradient $\bar{F}$

and address the question of whether such deformation can be matched on average by a sequential laminate of finite rank in which all leaves deform in single slip. Since single-slip deformations are volume preserving, $\bar{F}$ must itself necessarily be volume preserving for the laminate to be possible. Evidently, each leave i in the laminate introduces the four degrees of freedom R_i and γ_i. Additionally, each internal node i possesses the additional degree of freedom ν_i^- or ν_i^+, and introduces four rank-one compatibility constraints. Consequently, the number of independent degrees of freedom of the laminate is $d = 4n_l - 3n_i$, where n_l is the number of leaves and n_i is the number of internal nodes. Matching the nine components of $\bar{F}$ on average requires $d \geq 9$. For a rank-one laminate, $n_l = 2$, $n_i = 1$, and $d = 5$. For a complete rank-two laminate, $n_l = 4$, $n_i = 3$, and $d = 7$. Thus, two levels of lamination are not sufficient to match an arbitrary average deformation gradient in general. By contrast, the two rank-three laminates shown in Fig. 3.6 have $n_l = 6$, $n_i = 5$, and $d = 9$ as required. It therefore follows that the number of degrees of freedom required to match an arbitrary average deformation gradient may be attained with three levels of lamination.

In general, the condition $d \geq 9$ is necessary but not sufficient for the existence of single-slip laminates matching any arbitrary volume-preserving average deformation gradient $\bar{F}$ on average. Thus, in addition to having a sufficient number of degrees of freedom, the system of nonlinear equations (3.133) and (3.134) in the leaf unknowns R_i, γ_i, and the internal node unknowns ν_i^-, a_i and N_i, must have solutions for arbitrary $\bar{F}$. Physically, this in turn requires the crystal to possess a large enough class $\mathcal{S}$ of independent slip systems. The crystallographic flow rule (3.50) requires five independent slip systems to match an arbitrary volume-preserving rate of deformation, but it is not known if this criterion is a sufficient condition for the existence of laminates as well.

Finally, we consider average deformation histories of the form (3.94) within the framework of linearized kinematics. Within this approximation, single-slip deformation gradients admit the representation: $F = I + \omega + \gamma \mathrm{sym}(s \otimes m)$, where ω is a skewsymmetric tensor representing a small rotation. Let the laminate corresponding to the average deformation $\bar{F} = I + G$ be determined by ω_i and γ_i, at the leaves, and

ν_i^-, a_i and N_i at the internal nodes. Then, it follows immediately from the structure of equations (3.133) and (3.134) that the laminate corresponding to $F = I + f(t)G$ is determined by $f(t)\omega_i$ and $f(t)\gamma_i$, at the leaves, and ν_i^-, $f(t)a_i$ and N_i at the internal nodes. We note that the laminate undergoes persistent single slip, as required. It therefore follows that, in the context of linearized kinematics, the existence of a sequential single-slip laminate for an average deformation gradient $\bar{F} = I + G$ guarantees the existence of a persistent single-slip sequential laminate for any average deformation history of the form $\bar{F}(t) = I + f(t)G$.

3.5 Application to FCC crystals

The dislocation structures which arise in FCC single crystals and polycrystals subjected to monotonic and cyclic loading have been extensively documented in the literature and, consequently, provide a convenient test of the theory developed in the foregoing. We adopt throughout the Schmid and Boas nomenclature described in Section 3.3.2. The slip systems of FCC crystals are enumerated in Table 3.2.

3.5.1 Nondegenerate interfaces

We begin by considering interfaces which are nondegenerate at small strains, i.e., for $R^+ \approx I$. Since all the slip systems in an FCC crystal are symmetry-related, one of the systems meeting at the interface, e.g., on the (-) side, can be fixed without loss of generality. Then, for each system $(s^+, m^+) \in \mathcal{S}$ the nondegeneracy condition (3.125) may be verified at $R^+ = I$, leading to a complete enumeration of the nondegenerate interfaces of FCC crystals. The geometry of these interfaces then follows from (3.122) and (3.123). The results of these calculations are summarized in Tables 3.3 and 3.4. It should be carefully noted that the roles of $[\![v_{,n}]\!]$ and n are interchangeable. The crystallographic nature of the interface planes is noteworthy. As demonstrated subsequently, Tables 3.3 and 3.4 are a compendium of commonly observed dislocation walls, which atests to the soundness of the theory.

System (-) A2 / System (+)	B4	B5	C5	C3	D6	D4	D1	C1
$\dot{\gamma}^+/\dot{\gamma}^-$	-2/3	2/3	1	-3/2	3/2	-1	1	-1
$[\![v,n]\!]$	$[13\bar{1}]$	$[2\bar{1}\bar{1}]$	$[10\bar{1}]$	$[12\bar{1}]$	$[1\bar{1}2]$	$[1\bar{1}0]$	[100]	[010]
n	$(2\bar{1}\bar{1})$	$(1\bar{1}3)$	$(1\bar{1}1)$	$(3\bar{1}1)$	$(31\bar{1})$	$(11\bar{1})$	$(00\bar{1})$	$(\bar{1}00)$
System (-) A3 / System (+)	B4	B5	B2	C5	D6	D4	D1	C1
$\dot{\gamma}^+/\dot{\gamma}^-$	1	1	3/2	2/3	3/2	1	-1	2/3
$[\![v,n]\!]$	$[\bar{1}00]$	$[1\bar{1}1]$	[211]	$[1\bar{2}\bar{1}]$	$[\bar{1}1\bar{2}]$	[001]	[111]	[311]
n	(010)	$(0\bar{1}\bar{1})$	$(1\bar{3}1)$	$(1\bar{1}3)$	$(\bar{1}3\bar{1})$	$(0\bar{1}0)$	$(1\bar{1}0)$	$(1\bar{2}\bar{1})$
System (-) A6/ System (+)	B4	B5	B2	C5	C3	D4	D1	C1
$\dot{\gamma}^+/\dot{\gamma}^-$	1	1	-3/2	1	3/2	2/3	2/3	-1
$[\![v,n]\!]$	$[0\bar{1}\bar{1}]$	[100]	$[11\bar{3}]$	[001]	$[12\bar{1}]$	$[\bar{1}3\bar{1}]$	$[1\bar{1}\bar{2}]$	$[10\bar{1}]$
n	$(11\bar{1})$	$(00\bar{1})$	(211)	$(0\bar{1}0)$	(113)	$(\bar{1}12)$	$(3\bar{1}\bar{1})$	(111)
System (-) B2 / System (+)	A3	C5	C3	D6	D4	D1	A6	C1
$\dot{\gamma}^+/\dot{\gamma}^-$	2/3	-3/2	1	-1	3/2	-1	-2/3	1
$[\![v,n]\!]$	$[1\bar{3}1]$	$[11\bar{2}]$	$[1\bar{1}1]$	$[11\bar{1}]$	$[1\bar{2}1]$	$[\bar{1}00]$	$[11\bar{3}]$	[100]
n	$(2\bar{1}\bar{1})$	$(3\bar{1}1)$	$(\bar{1}\bar{1}0)$	$(\bar{1}0\bar{1})$	$(\bar{3}11)$	(010)	(211)	(001)
System (-) B4 / System (+)	A3	C5	C3	D6	D1	A6	C1	A2
$\dot{\gamma}^+/\dot{\gamma}^-$	1	3/2	1	2/3	-2/3	1	1	-3/2
$[\![v,n]\!]$	[010]	$[11\bar{2}]$	[001]	$[\bar{1}2\bar{1}]$	$[3\bar{1}\bar{1}]$	$[\bar{1}1\bar{1}]$	$[1\bar{1}\bar{1}]$	$[2\bar{1}\bar{1}]$
n	$(\bar{1}00)$	$(\bar{1}3\bar{1})$	$(0\bar{1}0)$	$(\bar{1}\bar{1}3)$	$(\bar{1}2\bar{1})$	$(0\bar{1}\bar{1})$	$(\bar{1}\bar{1}0)$	$(\bar{1}3\bar{1})$
System (-) B5/ System (+)	A3	C3	D6	D4	D1	A6	C1	A2
$\dot{\gamma}^+/\dot{\gamma}^-$	1	2/3	1	3/2	1	1	-2/3	3/2
$[\![v,n]\!]$	$[\bar{1}1\bar{1}]$	[112]	[001]	$[12\bar{1}]$	$[1\bar{1}\bar{1}]$	[100]	$[3\bar{1}\bar{1}]$	$[2\bar{1}\bar{1}]$
n	$(0\bar{1}\bar{1})$	$(1\bar{3}1)$	$(0\bar{1}0)$	$(\bar{1}13)$	$(\bar{1}0\bar{1})$	(001)	(112)	$(1\bar{1}3)$

Table 3.3: Geometry of nondegenerate interfaces between single-slip variants in FCC crystals at small strains (Part A). It should be carefully noted that the roles of $[\![v,n]\!]$ and n are interchangeable.

System (-) C1 / System (+)	B4	B5	B2	A3	D6	D4	A6	A2
$\dot{\gamma}^+/\dot{\gamma}^-$	1	-3/2	1	3/2	-2/3	2/3	-1	-1
$[\![v,n]\!]$	$[110]$	$[3\bar{1}\bar{1}]$	$[100]$	$[1\bar{2}\bar{1}]$	$[11\bar{3}]$	$[\bar{1}31]$	$[10\bar{1}]$	$[\bar{1}00]$
n	$(\bar{1}11)$	$(\bar{1}\bar{1}\bar{2})$	$(00\bar{1})$	(311)	$(21\bar{1})$	$(\bar{2}\bar{1}1)$	$(\bar{1}\bar{1}\bar{1})$	(010)
System (-) C3 / System (+)	B4	B5	B2	D6	D4	D1	A6	A2
$\dot{\gamma}^+/\dot{\gamma}^-$	1	3/2	1	1	1	-3/2	2/3	-2/3
$[\![v,n]\!]$	$[0\bar{1}0]$	$[\bar{1}3\bar{1}]$	$[110]$	$[\bar{1}\bar{1}\bar{1}]$	$[010]$	$[2\bar{1}1]$	$[\bar{1}\bar{1}\bar{3}]$	$[3\bar{1}1]$
n	(001)	$(11\bar{2})$	$(1\bar{1}1)$	$(0\bar{1}1)$	$(\bar{1}00)$	$(\bar{1}\bar{3}\bar{1})$	$(12\bar{1})$	$(12\bar{1})$
System (-) C5 / System (+)	B4	B2	A3	D6	D4	D1	A6	A2
$\dot{\gamma}^+/\dot{\gamma}^-$	2/3	-2/3	3/2	1	1	3/2	1	1
$[\![v,n]\!]$	$[11\bar{2}]$	$[3\bar{1}1]$	$[1\bar{1}3]$	$[100]$	$[\bar{1}11]$	$[2\bar{1}1]$	$[0\bar{1}0]$	$[10\bar{1}]$
n	$(\bar{1}31)$	$(\bar{1}\bar{1}\bar{2})$	$(\bar{1}21)$	$(00\bar{1})$	$(0\bar{1}1)$	$(1\bar{1}\bar{3})$	(001)	$(\bar{1}1\bar{1})$
System (-) D1 / System (+)	B4	B5	B2	A3	C5	C3	A6	A2
$\dot{\gamma}^+/\dot{\gamma}^-$	-3/2	1	-1	-1	2/3	-2/3	3/2	1
$[\![v,n]\!]$	$[121]$	$[1\bar{1}\bar{1}]$	$[010]$	$[111]$	$[2\bar{1}1]$	$[131]$	$[1\bar{1}\bar{2}]$	$[100]$
n	$(3\bar{1}\bar{1})$	(101)	(100)	$(1\bar{1}0)$	$(1\bar{1}\bar{3})$	$(2\bar{1}1)$	(311)	(001)
System (-) D4 / System (+)	B5	B2	A3	C5	C3	A6	C1	A2
$\dot{\gamma}^+/\dot{\gamma}^-$	2/3	2/3	1	1	1	3/2	3/2	-1
$[\![v,n]\!]$	$[1\bar{1}\bar{3}]$	$[1\bar{2}1]$	$[0\bar{1}0]$	$[0\bar{1}1]$	$[\bar{1}00]$	$[\bar{1}\bar{3}1]$	$[21\bar{1}]$	$[11\bar{1}]$
n	$(\bar{1}2\bar{1})$	$(\bar{3}\bar{1}1)$	(001)	$(1\bar{1}\bar{1})$	(010)	$(\bar{1}12)$	$(\bar{1}\bar{3}\bar{1})$	$(\bar{1}\bar{1}0)$
System (-) D6 / System (+)	B4	B5	B2	A3	C5	C3	C1	A2
$\dot{\gamma}^+/\dot{\gamma}^-$	3/2	1	-1	2/3	1	1	-3/2	2/3
$[\![v,n]\!]$	$[\bar{1}\bar{1}3]$	$[0\bar{1}0]$	$[11\bar{1}]$	$[\bar{1}3\bar{1}]$	$[100]$	$[111]$	$[113]$	$[31\bar{1}]$
n	(121)	(001)	(101)	$(\bar{1}\bar{1}2)$	(001)	$(0\bar{1}1)$	$(21\bar{1})$	$(1\bar{1}2)$

Table 3.4: Geometry of nondegenerate interfaces between single-slip variants in FCC crystals at small strains (Part B). It should be carefully noted that the roles of $[\![v,n]\!]$ and n are interchangeable.

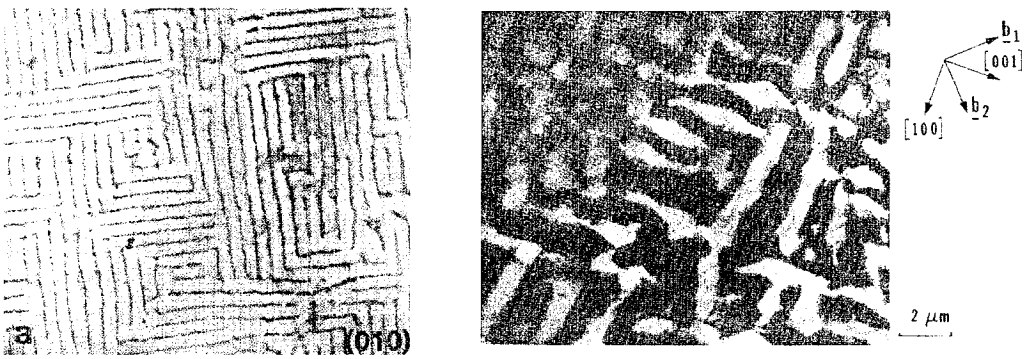

(a) (b)

Figure 3.7: a) Copper single crystal fatigued with tensile axis [001], showing labyrinth wall structure on [100] and [001]-planes [JW84a]; b) (010)-cross section of a copper single crystal specimen showing labyrinth dislocation structure [AKLM84].

As an example, we choose $(s^-, m^-) = \big([10\bar{1}], (111)\big) \equiv$ B4. A common test configuration involves the activation of a pair of orthogonal Burgers vectors in a fatigued single crystal, which corresponds to the B4-A3 and B4-C3 interfaces in tables 3.3 and 3.4. In these cases, the interface normals predicted by the theory are of the $\{100\}$ type, in agreement with experimentally observed wall orientations ([DBL86]; [LVD86]; [RP80]; [Cha81]; [BBT85]; [MB82]; [JW84a]; [AKLM84]; [WM84]; [LKK84]; [Jin87]). For instance, Jin and Winter [JW84a] have reported the labyrinth structure shown in Fig. 3.7a, corresponding to cyclically deformed copper single crystals loaded in the [001] direction. The (010) section of the specimen shown in the figure clearly exhibits traces of (001) and (100) dislocation walls. A similar labyrinth structure is also evident in Fig. 3.7b, corresponding to cyclically deformed copper single crystals oriented between [012] and $[\bar{1}35]$, followed by *in situ* cyclic straining in pure shear [AKLM84].

For a [001] crystal such as tested by Jin and Winter [JW84a], Fig. 3.7a, the eight systems B4, B2, A3, C3, D4, D1, C1 and A2 are potentially active with a Schmid factor $\tau/\sigma = 0.40825$. The interfaces leading to (001) dislocation walls are: B4-C3, B2-C1, A3-D4 and D1-A2; the interfaces giving (100) dislocation walls are: B4-A3,

B2-D1, B2-C1, C3-D4, D1-A2 and C1-A2. The geometry of the B4-C3 interface is shown in Fig. 3.8a. It is noteworthy that the Burgers vectors involved are mutually orthogonal, a feature that has long been thought to be characteristic of labyrinth structures. Both sets of interfacial dislocations have the common direction $[1\bar{1}0]$, in accordance with (3.108). The remaining (001)-interfaces are related to the B4-C3 interface by symmetry operations in the cubic symmetry group which leave the loading direction [001] and the wall plane (001) invariant. Thus, the A2-D1 interface is obtained from the B4-C3 interface by a 90° rotation about the [001] axis; the B2-C1 interface is obtained from the B4-C3 interface by a reflection about the $(1\bar{1}0)$ plane; and the A3-D4 interface is obtained from the B2-C1 interface by a 90° rotation about the [001] axis.

The geometries of the B4-A3, B2-D1 and B2-C1 interfaces are shown in Figs. 3.8b-d. As before, the Burgers vectors of the active systems are mutually orthogonal. In the B4-A3 interface, both sets of interfacial dislocations have the common direction $[01\bar{1}]$, in accordance with (3.108). The B2-D1 and B2-C1 interfaces contain two families of orthogonal screw dislocations along the [011] and $[0\bar{1}1]$ directions. The remaining (100)-interfaces are obtained from the B4-A3, B2-D1 and B2-C1 interfaces by the application of symmetry operations in the cubic symmetry group which leave the loading direction [001] and the wall plane (001) invariant. Thus, the C3-D4 and C1-A2 interfaces are obtained from the B4-A3 and B2-D1 interfaces by the application of 180° rotations about the [001] axis; and the D1-A2 interface follows from the B2-C1 interface by the application of a reflection about the (100) plane.

Other theoretically predicted interfaces are also born out by observation. Thus, Jin [Jin87] observed a labyrinth structure in cyclically deformed copper single crystals loaded in the [011] direction. Fig. 3.9a shows a $(0\bar{1}1)$-section of the specimen. Traces of two sets of dislocation walls along the [100] and [011] directions are clearly apparent in the figure. All dislocation wall traces are of comparable width, which is suggestive of (011) and (100) walls perpendicular to the $(0\bar{1}1)$ plane. Jin [Jin87] noted that the most highly stressed slip planes for this configuration are B4, B5, A3 and A6. Walls of (011) orientation are consistent with B4-A6 and B5-A3 interfaces, while (100)-walls

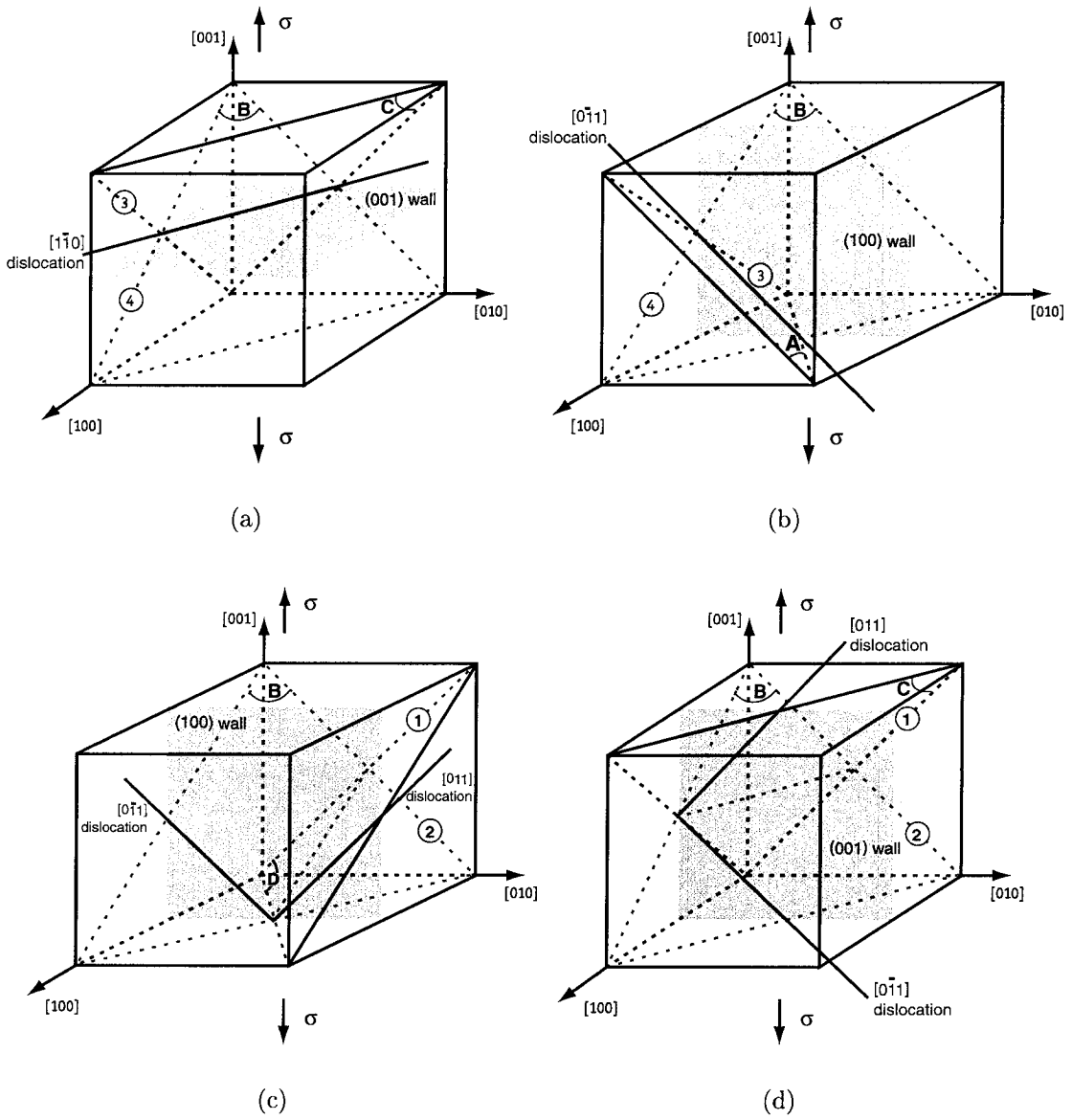

Figure 3.8: a) Geometry of the B4-C3 interface; b) geometry of the B4-A3 interface; c) geometry of the B2-D1 interface; d) geometry of the B2-C1 interface.

correspond to the B4-A3 and B5-A6 interfaces; see Fig. 3.10f. A similar structure was observed by Charsley [Cha81], Fig. 3.9b, in polycrystalline copper alloys fatigued to saturation.

Observations of Jin [Jin83] and [JW84b] of dislocation structures on $(1\bar{1}1)$ foils of a copper single crystal cyclically deformed along the $[\bar{1}12]$ axis show dislocation wall traces in the [110] and $[\bar{1}12]$ directions. For this loading axis, the highest resolved shear stresses occur on systems B4 and C1, with a Schmid factor of 0.40825. The two types of B4-C1 interfaces correspond to $(1\bar{1}\bar{1})$ and (110) dislocation walls, Tables 3.3 and 3.4. These walls intersect the $(1\bar{1}1)$ plane along the [110] and $[\bar{1}12]$ directions, respectively, in agreement with observation. In polycrystalline copper, walls of the {110} type have also been found by Boutin [Bou83] and by Wang *et al.* [WM84], Fig. 3.11; and walls of the {111} type have been observed by Liu *et al.* in fatigued polycrystalline copper [Yum89], Fig. 3.12.

Lepistö *et al.* [LKK86] reported wall structures in copper single crystals cycled in the $[\bar{1}11]$ direction. In this orientation, the systems B4, B5, C5, D4, D1 and C1 are all potentially active with a common Schmid factor of 0.27217. A $(12\bar{1})$ section of the specimen revealed an arrangement of parallel dislocation wall traces in the [101] direction, Fig. 3.13. These traces are consistent with B4-C5 and D4-C1 interfaces, which give $(1\bar{3}\bar{1})$ walls; and B4-C1 and C5-D4 interfaces, which result in $(1\bar{1}\bar{1})$ walls, Fig.řefInterfacesFig3. Walls of the {113} type have also been observed by Boutin ([Bou83]; [DBL86]; [DHL86]), Fig. 3.15a and by Liu *et al.* [Yum89] in polycrystalline copper.

3.5.2 Degenerate interfaces

Next we seek to characterize the degenerate interfaces of FCC crystals. These interfaces fall into three categories: interfaces between coplanar systems with coincident normals $m^+ = m^-$ and different slip directions $s^+ \neq s^-$; interfaces between cross-glide systems having coincident slip directions $s^+ = s^-$ and different normals $m^+ \neq m^-$; and interfaces involving one single slip system, i. e., such that $m^+ = m^-$ and $s^+ = s^-$.

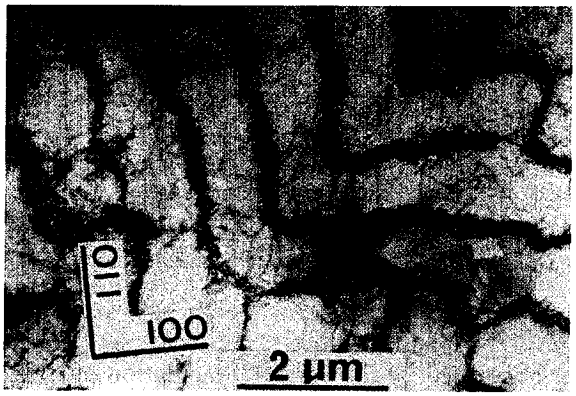

(a)

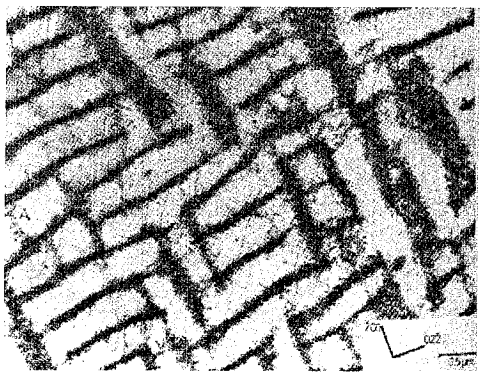

(b)

Figure 3.9: Further examples of the labyrinth structure. a) $(0\bar{1}1)$-section of copper single crystal cycled in the [011] direction [Jin87]; b) polycrystalline Cu-Ni alloy fatigued to saturation [Cha81].

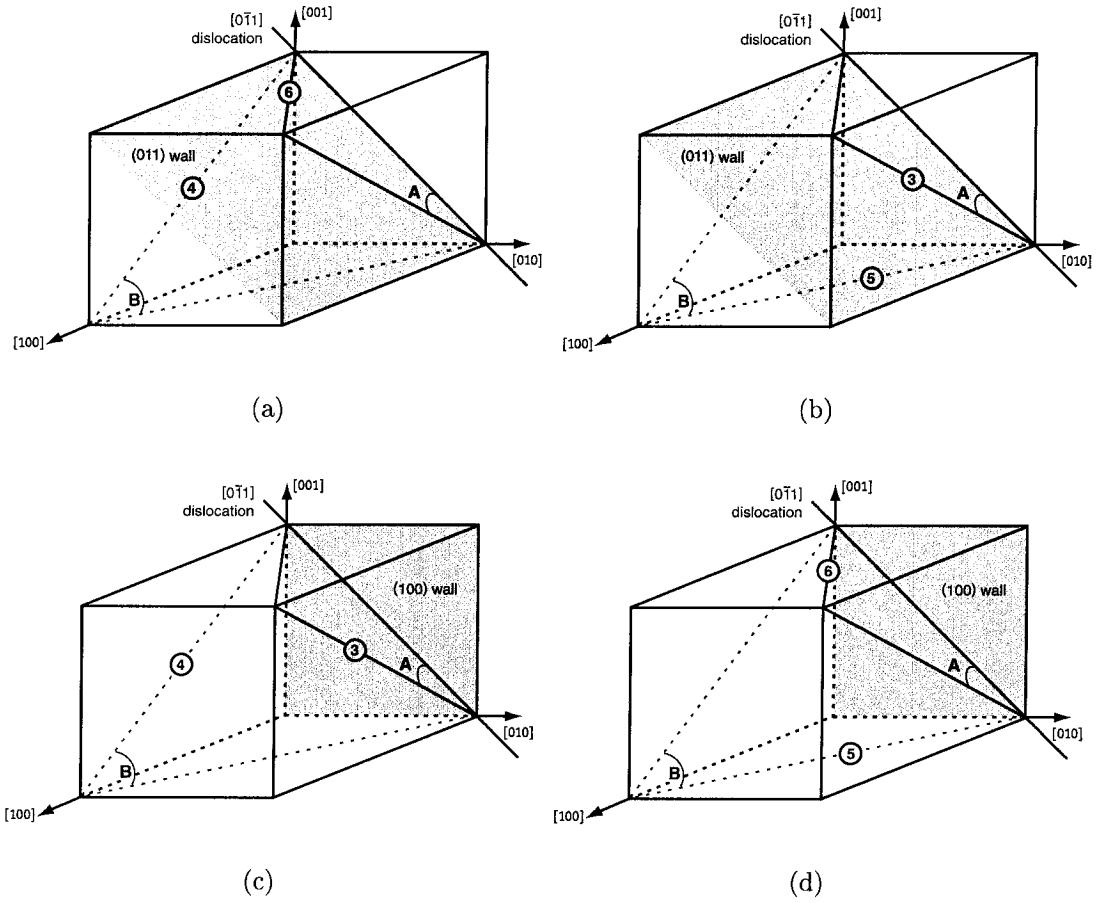

Figure 3.10: a) Geometry of the B4-A6 interface; b) geometry of the B5-A3 interface; c) geometry of the B4-A3 interface; d) geometry of the B5-A6 interface.

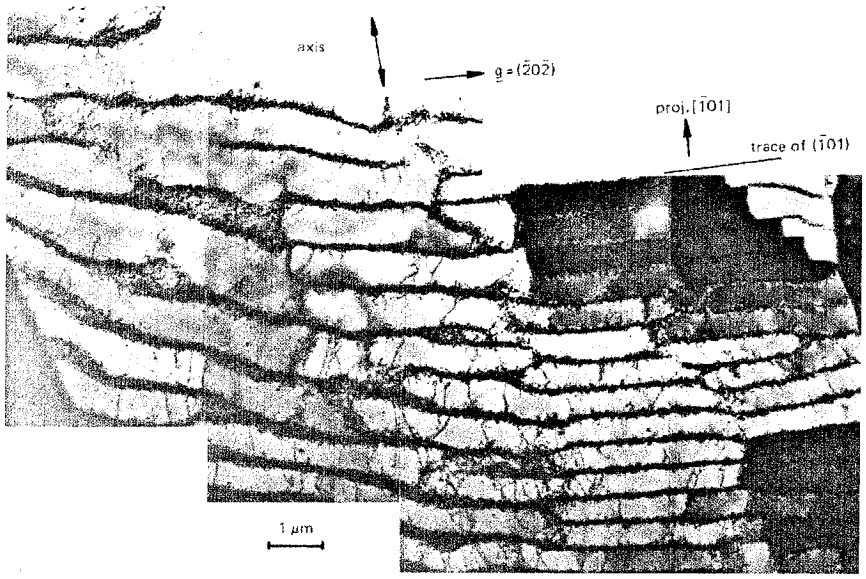

(a)

Figure 3.11: (101) wall structure in fatigued polycrystalline copper [WM84].

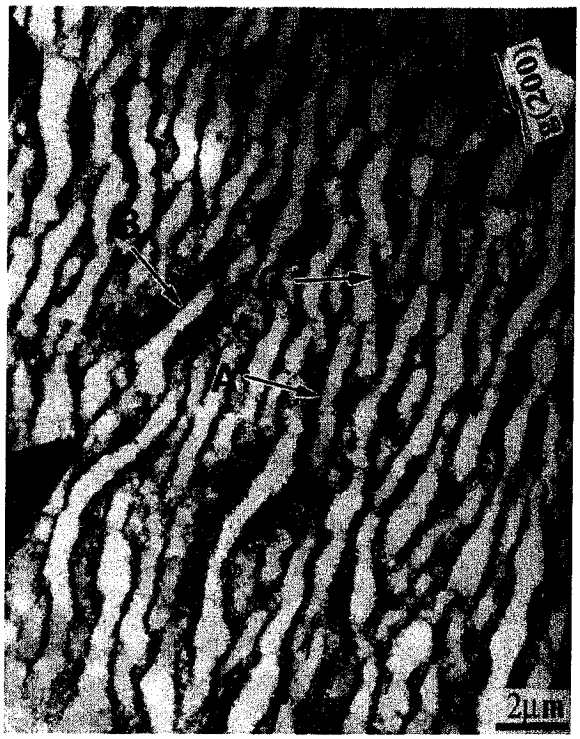

(a)

Figure 3.12: $(11\bar{1})$ wall structure in fatigued polycrystalline copper [Yum89].

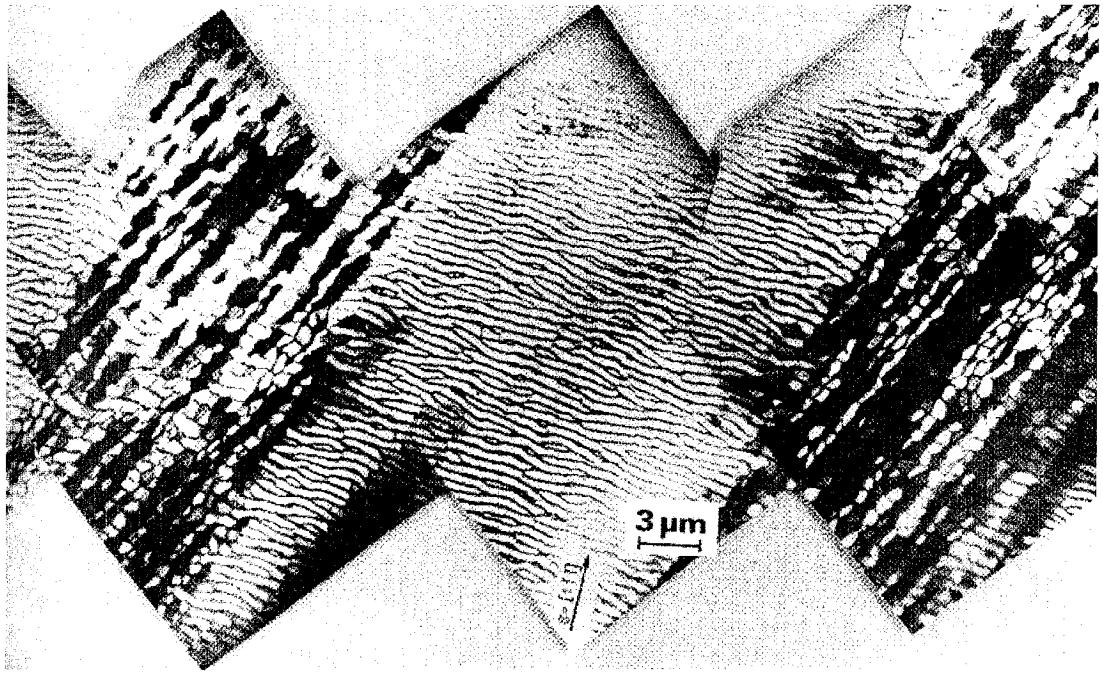

(a)

Figure 3.13: $(12\bar{1})$ section of fatigued $[\bar{1}11]$ single crystal showing possible $(1\bar{3}\bar{1})$ or $(1\bar{1}\bar{1})$ wall structure [LKK86].

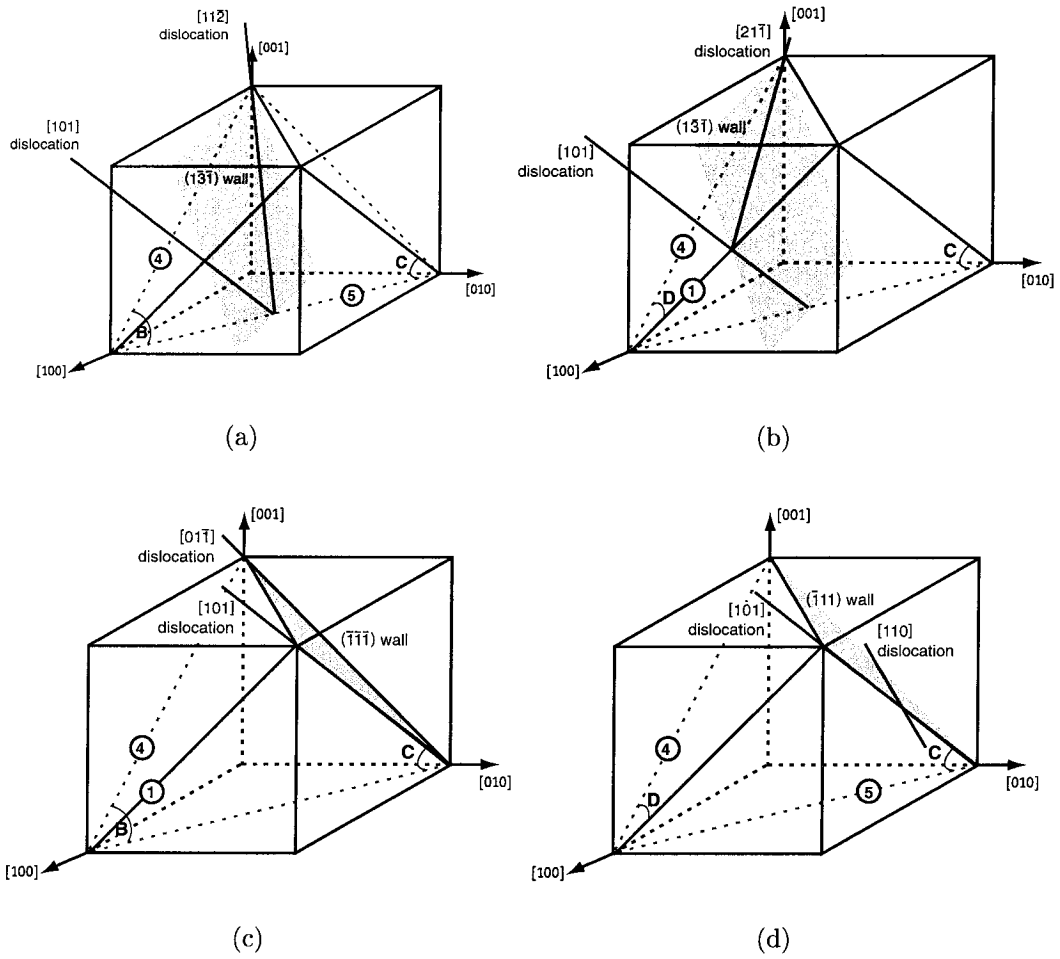

Figure 3.14: a) Geometry of the B4-C5 interface; b) geometry of the D4-C1 interface; c) geometry of the B4-C1 interface; d) geometry of the C5-D4 interface.

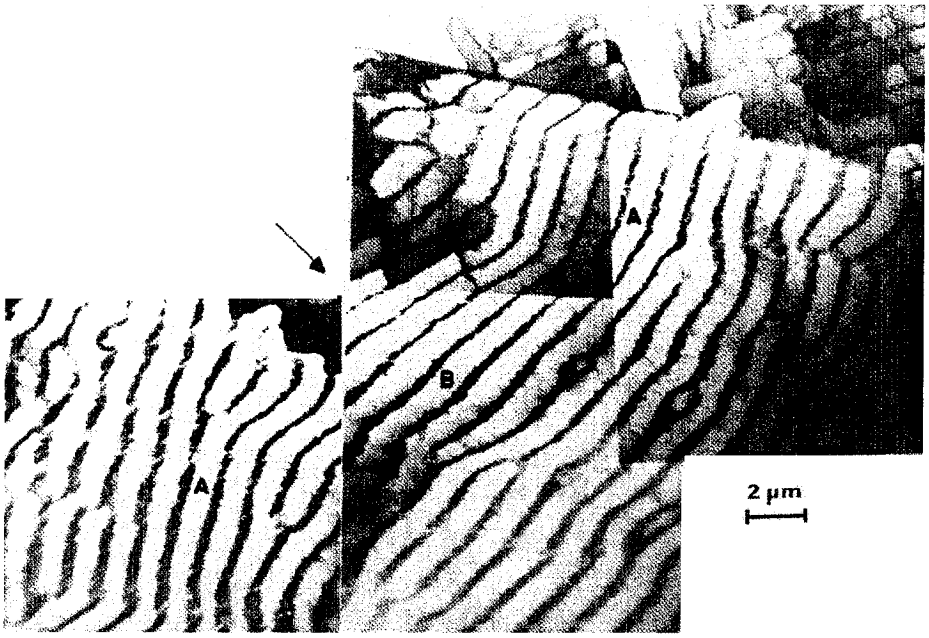

(a)

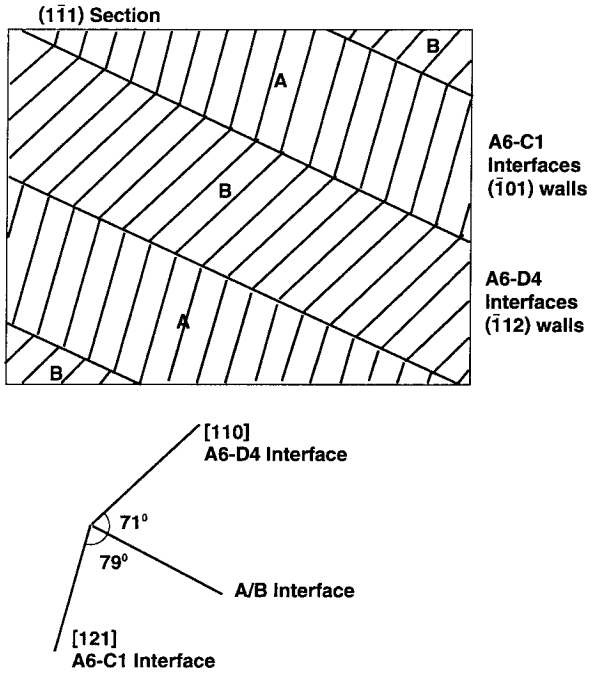

(b)

Figure 3.15: a) Detail of fatigued polycrystalline copper showing ($\bar{1}$01) walls (region A) and either ($\bar{1}$12) or ($\bar{1}$13) walls (region B) ([Bou83]; [DBL86]; [DHL86]). b) Rank-two laminate predicted by the theory.

In all these cases, eq. (3.121) is trivially satisfied and the jump condition (3.104) must be directly enforced in order to ascertain the geometry of the interface.

Pairs of coplanar systems having a common normal satisfy (3.104) with

$$R^+ = R^- \equiv R, \qquad [\![y,_N]\!] = \gamma^+ s^+ - \gamma^- s^-, \qquad N = m^+ = m^- \equiv m. \tag{3.135}$$

In these interfaces, the slip strains $\gamma^\pm$ are not constrained by compatibility and may be chosen arbitrarily. Evidently, coplanar interfaces are parallel to the common slip plane. Coplanar slip zones have been observed by Higashida *et al.* [HTN86] to form during the stage I of hardening in a Cu-1at.%Ge single crystal loaded in monotonic tension near the [321] direction, Fig. 3.16a. For a crystal in this orientation, the primary slip system is C3, with a Schmid factor of 0.46657. However, Higashida *et al.* [HTN86] observed that the systems C1 and C5 are predominantly active in coplanar slip zones, while the activity on the more loaded primary system C3 is largely inhibited. Indeed, the joint activation of the C1 and C5 systems does result in an energetic advantage over the activation of system C3, as demonstrated subsequently in Section 3.5.3.

Similarly, pairs of cross-glide systems having a common slip direction satisfy (3.104) with

$$\begin{aligned} R^+ = R^- \equiv R, \qquad & [\![y,_N]\!] = \| \gamma^+ m^+ - \gamma^- m^- \| \, s, \\ N \;\; = \;\; & \frac{\gamma^+ m^+ - \gamma^- m^-}{\| \gamma^+ m^+ - \gamma^- m^- \|} \end{aligned} \tag{3.136}$$

where we write $s \equiv s^+ = s^-$. As in the coplanar case, the slip strains $\gamma^\pm$ are not constrained by compatibility and may be chosen arbitrarily.

Finally, we consider interfaces involving nontrivial rank-one connections of a slip system with itself. Evidently, a class of interfaces of this type can be constructed as in the coplanar case, leading to

$$R^+ = R^- \equiv R, \qquad [\![y,_N]\!] = (\gamma^+ - \gamma^-) s, \qquad N = m. \tag{3.137}$$

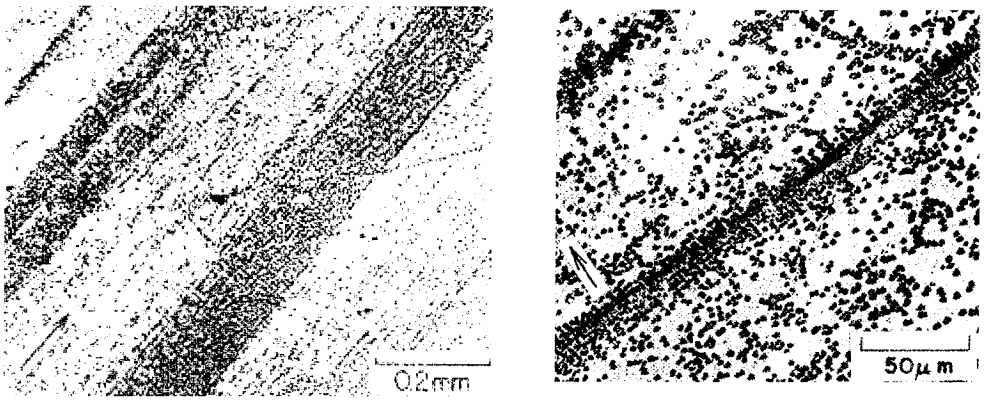

(a) (b)

Figure 3.16: Cu-1at.%Ge alloy crystal oriented near [321] and deformed monotonically to 30% strain [HTN86]. a) Coplanar slip zones revealed by etch pits on the conjugate plane; b) etch pit configuration due to secondary dislocations in the vicinity of kink bands.

It should be noted that in this case the plastic deformations $F^{p\pm}$ are themselves rank-one compatible and, in view of (3.105), the interfaces are free of dislocations. The dislocations are either pushed out to infinity or bind tightly to form dense walls of zero net Burgers vector, such as the rungs in the ladder structure which arises in single crystals oriented for single slip and fatigued to saturation, Fig. 3.17. Such walls are invisible within the present continuum description of dislocations, and regions of the crystal containing them are indistinguishable from the defect-free crystal.

The matrix-persistent slip band (PSB) boundaries in cyclically deformed single crystals oriented for single slip constitute a prime example of this type of interface (e.g., [MAH79]; [WM84]), Fig. 3.17. The planes of the PSBs are ostensibly parallel to primary slip plane, in accordance with (3.137). It bears emphasis, however, that the inhomogeneous character of slip in this structure cannot be explained on the basis of latent hardening, as only one system is kinematically necessary to match the average strain. An alternative explanation may be based on the geometrical softening phenomenon discussed in Section 3.3.4. We shall return to this question in

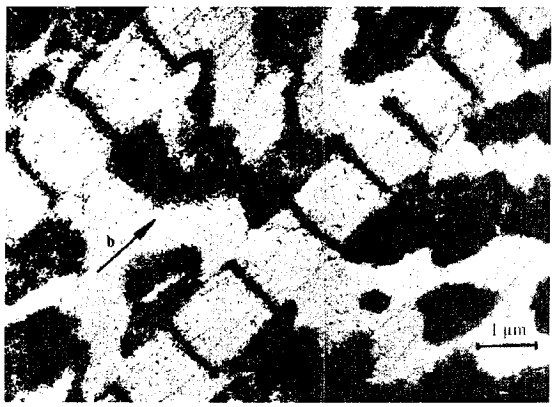

(a)

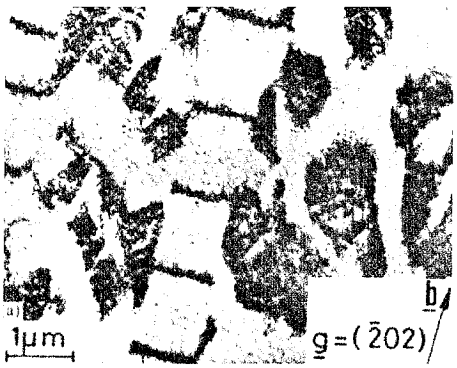

(b)

Figure 3.17: Views of the $(1\bar{2}1)$ section of Cu crystals oriented for single slip and fatigued to saturation at room temperature revealing matrix and persistent slip bands (PSB) a) From Mughrabi, Ackermann and Hertz [MAH79]; b) from Wang and Mughrabi [WM84].

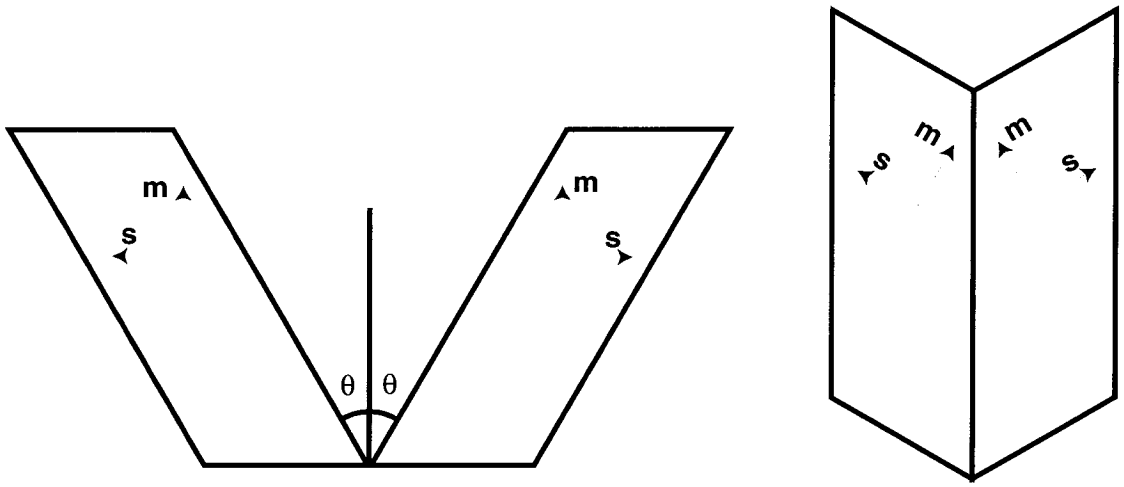

Figure 3.18: Schematic of kink formation. a) Slip strains $\gamma^{\pm} = \pm \tan\theta$; b) rotations through $\pm \tan\theta$.

Section 3.5.3.

A complementary class of single-system interfaces can be constructed as follows. Choose the interface normal $N = s$, i. e., any vector of type $\langle 110 \rangle$, and impart slip strains $\gamma^{\pm} = \pm \tan\theta$ on both sides of the interface, Fig. 3.18a. Restore compatibility by effecting rotations $R^{\pm} = Q\, R(s \times m; \pm\theta)$. Here, the notation $R(e; \alpha)$ is used to denote a rotation about an axis e through and angle α, and Q is an arbitrary rotation. Since the planes on both sides of the interface remain unstretched along the $s \times m$ direction and stretch by the same amount in the m direction, the rotated crystals fit compatibly, Fig. 3.18b. The resulting deformations are

$$F^{\pm} = Q\, R(s \times m; \pm\theta)\, [I \pm \tan\theta s \otimes m]. \tag{3.138}$$

These satisfy (3.104) with

$$[\![y_{,N}]\!] = 2 \sin\theta Q m, \qquad N = s. \tag{3.139}$$

The deformations (3.138) of the variants can alternatively be rewritten as

$$\begin{aligned} F^{\pm} &= Q[\cos\theta s \otimes s + \sec\theta m \otimes m + (s \times m) \otimes (s \times m)] \\ &\qquad [I \pm \sin\theta\cos\theta m \otimes s] \qquad (3.140) \\ &= Q[I \pm \tan\theta m \otimes s] \\ &\qquad [\cos\theta s \otimes s + \sec\theta m \otimes m + (s \times m) \otimes (s \times m)]. \qquad (3.141) \end{aligned}$$

Thus the variant deformations consist of the composition of slip strains of magnitude $\gamma = \pm\sin\theta\cos\theta$ on the plane of normal s in the direction m, followed by stretches of magnitude $\cos\theta$ and $\sec\theta$ in the directions s and m, respectively, followed by an arbitrary rotation Q; or, equivalently, the composition of stretches of magnitude $\cos\theta$ and $\sec\theta$ in the directions s and m, respectively, followed by slip strains of magnitude $\gamma = \pm\tan\theta$ on the plane of normal s in the direction m, followed by an arbitrary rotation Q. The dislocation density tensor (3.105) evaluates to

$$A(x) = 2\tan\theta s \otimes (s \times m)\delta_{\Pi}(x) \qquad (3.142)$$

which represents a planar array of parallel edge dislocations, or tilt boundary.

This type of interface arises in the so-called "fence" structures observed during the early stages of stage II of hardening in FCC crystals [Ste66], Fig. 3.19. Because the dislocation walls are normal to the primary slip direction, eq. (3.139), they are sometimes termed "kinks," and the resulting deformation structures "kink bands" [HTN86], [Cah51]. Higashida *et al.* [HTN86] observed the emergence of kink bands at the onset of stage II of hardening in a Cu-1at.%Ge single crystal loaded in monotonic tension near the [321] direction. As noted above, for a crystal in this orientation, the primary slip system active is C3. In a $(\bar{1}11)$-section of the specimen, the kink bands were revealed by dense etch-pit arrays normal to the Burgers vector, Fig. 3.16b.

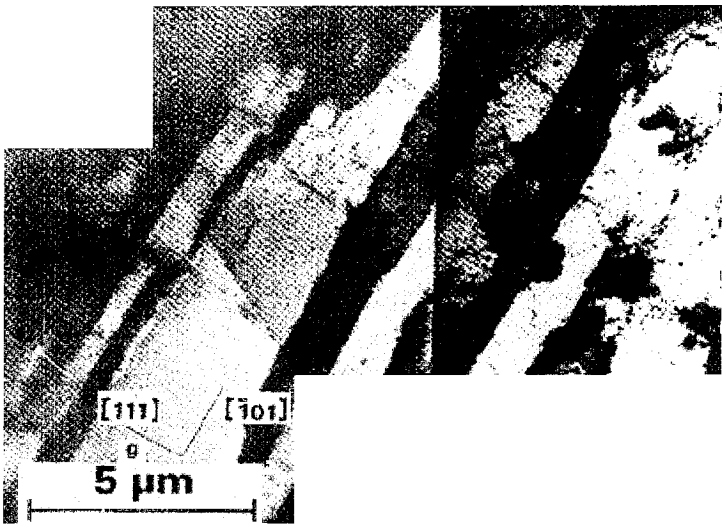

Figure 3.19: Fences normal to the slip in copper deformed to stage III [Ste66].

3.5.3 Simple laminates

By lamination of single-slip variants, crystals can attain a larger class of average deformations $\bar{F}$ while remaining essentially free of long-range stresses. For instance, for coplanar variants the average deformation of the corresponding laminate is

$$\bar{F} = R(I + \gamma s \otimes m) \tag{3.143}$$

with

$$\gamma = \| \nu^+\gamma^+ s^+ + \nu^-\gamma^- s^- \|, \qquad s = \frac{\nu^+\gamma^+ s^+ + \nu^-\gamma^- s^-}{\| \nu^+\gamma^+ s^+ + \nu^-\gamma^- s^- \|}. \tag{3.144}$$

This represents a single-slip deformation on the common plane m in the effective slip direction s. Evidently, by varying the slip activities $\gamma^\pm$ of the systems and their volume fractions $\nu^\pm$, any effective slip direction s orthogonal to m can be achieved. Thus, coplanar laminates effectively extend the crystallographic slip-system set $\mathcal{S}$ to include all systems (s, m) consisting of a cube diagonal m and any direction s orthogonal to m.

As noted in Section 3.5.2, coplanar slip zones have been observed by Higashida *et al.* [HTN86] to form during the stage I of hardening in a Cu-1at.%Ge single crystal loaded in monotonic tension near the [321] direction, Fig. 3.16a. For a crystal in this orientation, the slip direction giving the maximum Schmid factor is [527] which, evidently, is not a crystallographic slip direction. It should be noted that slip in the maximum Schmid factor direction minimizes the work W required to attain a given prescribed deformation, which in turn is in accordance with the minimum principle (3.38). Higashida *et al.* observed that the primary coplanar slip systems C1 and C5 are predominantly active in nearly equal amounts in the coplanar slip zones. The optimal slip direction [527] can be effectively attained as in eq. (3.144) through the combined operation of the systems C1 and C5 with $\gamma_{C1} = \gamma_{C5}$ and $\nu_{C1} = 7/12$, $\nu_{C5} = 5/12$. This ability of coplanar slip zones to effectively match the optimal slip direction confers them an energetic advantage which explains their occurrence in actual crystals.

Likewise, for cross-glide variants having a common Burgers vector, the average deformation of the laminate is of the same form (3.135) with

$$\gamma = \| \nu^+\gamma^+ m^+ + \nu^-\gamma^- m^- \|, \qquad m = \frac{\nu^+\gamma^+ m^+ + \nu^-\gamma^- m^-}{\| \nu^+\gamma^+ m^+ + \nu^-\gamma^- m^- \|} \tag{3.145}$$

Thus, the average deformation is of the single-slip type on the effective plane m along the common slip direction s. By varying the slip activities $\gamma^\pm$ of the systems and their volume fractions $\nu^\pm$, any effective normal m orthogonal to s can be achieved and, consequently, cross-glide laminates effectively extend the crystallographic slip-system set $\mathcal{S}$ to include all systems (s, m) consisting of a cube-face diagonal s and any normal m orthogonal to s.

Finally, we turn to single-system laminates. We begin by considering the "slip-band" geometry in which the interfaces are parallel to the slip plane. As noted in Section 3.5.3, a prime example of this type of lamination is furnished by the matrix-PSB structure characteristic of single crystals oriented for single slip and fatigued to saturation (e.g., [MAH79]; [WM84]), Fig. 3.17. In this microstructure, the average

deformation is carried almost completely by the PSB's, and the matrix remains nearly undeformed by comparison. The average deformation is again of the form (3.143), with

$$\gamma = \nu^{+}\gamma^{+} + \nu^{-}\gamma^{-} \tag{3.146}$$

where $\nu^{\pm}$ and $\gamma^{\pm}$ are the volume fractions and slip strains in the matrix and PSB. A similar deformation pattern is observed in the form of slip bands during the stage I of hardening of most FCC crystals [FW59]. Eq. (3.146) is the basic kinematic relation underlying the so-called "two-phase model" of cyclic deformation [Win74].

Evidently, slip-band structures cannot be caused by latent hardening, as only one system is in operation in those structures. A plausible alternative mechanism is geometrical softening, Section 3.3.4, which results in the up-down-up stress-strain curve characteristic of displacive phase transitions, Fig. 3.2b. Under these conditions, the work of deformation of the crystal is minimized by the development of two phases–the matrix and the bands–which jointly operate at the Maxwell stress [Eri80]. This stress is determined by the equal-area rule, i. e., the two regions demarcated by the Maxwell line and the stress-strain curve must be identical, Fig. 3.2b. We note that the Maxwell stress may be considerably lower than that required for the operation of the slip system. The strains of the phases are those corresponding to the intersections of the Maxwell line with the ascending, or stable, parts of the stress-strain curve. In crystals which are elastically stiff, the matrix strain determined by this construction is small, in keeping with observation [Mug78], and approaches zero in the rigid-plastic limit. The volume fractions of the two phases follow from Gibbs rule.

For kink interfaces, the average deformation follows from (3.140) and (3.141) in

the form

$$\begin{aligned}\bar{F} &= Q[\cos\theta s \otimes s + \sec\theta m \otimes m + (s \times m) \otimes (s \times m)] \\ &\qquad [I + (\nu^+ - \nu^-)\sin\theta\cos\theta m \otimes s] \quad (3.147) \\ &= Q[I + (\nu^+ - \nu^-)\tan\theta m \otimes s] \\ &\qquad [\cos\theta s \otimes s + \sec\theta m \otimes m + (s \times m) \otimes (s \times m)] \quad (3.148)\end{aligned}$$

where, as before, $\nu^{\pm}$ are the volume fractions occupied by the + and − variants, respectively, with $\nu^+ + \nu^- = 1$. It follows from (3.147) and (3.148) that the average deformation which can be attained by a single-system laminate consists of the composition of a slip strain of magnitude $\gamma = (\nu^+ - \nu^-)\sin\theta\cos\theta$ on the plane of normal s in the direction m, followed by stretches of magnitude $\cos\theta$ and $\sec\theta$ in the directions s and m, respectively, followed by an arbitrary rotation Q; or, alternatively, the composition of stretches of magnitude $\cos\theta$ and $\sec\theta$ in the directions s and m, respectively, followed by a slip strain of magnitude $\gamma = (\nu^+ - \nu^-)\tan\theta$ on the plane of normal s in the direction m, followed by an arbitrary rotation Q. In the special case in which both variants are mixed in equal proportions, i. e., $\nu^+ = \nu^-$, the average deformation takes the form: $\bar{F} = QU$, where U is a stretch tensor with principal stretches $(\cos\theta, \sec\theta, 1)$ and principal directions $(s, m, s \times m)$, and Q is an arbitrary rotation. A clear example of this type of lamination is the fence structures observed during the early stages of stage II of hardening in FCC crystals [Ste66], Fig. 3.19. The alternating $\pm\theta$ misorientations about an axis in the slip plane predicted by the theory, eq. (3.138), are evident in the figure.

As noted in Section 3.4.2, the dislocation structure corresponding to first-order laminates consists of an array of parallel dislocation walls of the type (3.132). With the exception of labyrinth structures, all the dislocation walls discussed in Section 3.5.3 are observed to occur in roughly parallel arrays and, therefore, provide further examples of lamination; see Figs. 3.11, 3.12, 3.13, 3.15a, 3.16, 3.17, 3.19.

3.5.4 Sequential laminates

A few of the dislocation structures reported in the literature may arguably be interpreted as instances of sequential lamination. For instance, Fig. 3.20 shows a detail of an interior grain in a polycrystalline copper specimen tested in fatigue by Rasmussen and Pedersen [RP80]. A set of nearly horizontal fine laminates occupying nearly vertical parallel bands separated by other bands of cell structures is clearly visible in the figure, which would appear to furnish an example of a rank-two laminate. Another seeming example of a rank-two laminate is revealed by Fig. 3.15a, which shows a region of extended wall structure observed by Boutin [Bou83] in a fatigued polycrystalline copper. The structure consists of $(\bar{1}01)$ walls (region A) and either $(\bar{1}12)$ or $(\bar{1}13)$ walls (region B). These two types of laminates may be seen to occupy roughly horizontal alternating bands in Fig. 3.15a, which may be regarded as defining the first level of the laminate. It is interesting to note that both examples correspond to polycrystals, which inevitably develop complex deformations at the single grain level. Indeed, as noted in Section 3.4.3, the accommodation of general deformations by single slip requires several levels of lamination and, consequently, sequential laminates are more likely to arise in polycrystals.

The geometry of the dislocation structure shown in Fig. 3.15a may be ascertained much in the same way as the geometry of interfaces was determined in Section 3.4.1. We begin by analyzing the fine laminates A and B. Since the wall traces in Fig. 3.15a are of roughly equal thickness, it seems reasonable to presume that the section of the figure is orthogonal to both sets of walls, i. e., a $(1\bar{1}1)$ section. The wall traces on the $(1\bar{1}1)$ are [121] in laminate A and [110] in laminate B. Interfaces leading to $(\bar{1}01)$ walls are A2-C5 and A6-C1; interfaces resulting in $(\bar{1}12)$ walls are A6-D1 and A6-D4; and interfaces giving $(\bar{1}13)$ walls are C5-D1 and B5-D4. Assume that the walls in the B laminate are of the $(\bar{1}12)$ type and that the A and B interfaces are A6-C1 and A6-D4, respectively. As noted in Section 3.4.1, each of the A and B laminates has the eight degrees of freedom $\dot{R}^{\pm}(R^{\pm})^{-1}$ and $\dot{\gamma}^{\pm}$, and is subject to four compatibility conditions resulting from (3.113). This leaves four effective degrees of

freedom per laminate, e.g., $\dot{R}^-(R^-)^{-1}$ and $\dot{\gamma}^-$. The average deformation rates $l_{A,B}$ of laminates A and B follow from relations (3.113), (3.121), (3.122) and (3.123) in terms of the degrees of freedom $\dot{R}^-_{A,B}(R^-_{A,B})^{-1}$ and $\dot{\gamma}^-_{A,B}$. In computing averages, we assume equal volume fractions $\nu^- = \nu^+ = 1/2$, as suggested by the widths of the variants in Fig. 3.15a. Four degrees of freedom, e.g., $\dot{R}^-_A(R^-_A)^{-1}$ and $\dot{\gamma}^-_A$, can be fixed without loss of generality. The deformation rates $l_{A,B}$ are subject to the rank-one compatibility condition (3.113). This places four constraints which suffice to determine $\dot{R}^-_B(R^-_B)^{-1}$ and $\dot{\gamma}^-_B$. The treatment of these equations is now identical to that given in Section 3.4.1 to interfaces, leading to equations of the form (3.122) and (3.123) giving the orientation of the A-B interface. A straightforward calculation gives $n_{A-B} = (0.534523, 0.801785, 0.26726)$, the trace of which on the $(1\bar{1}1)$ plane is $[-1.06904, 0.267262, 1.33631]$, or, approximately, $(2, 3, 1)$ and $[\bar{4}, 1, 5]$. The geometry predicted by the theory is shown in Fig. 3.15b. The agreement between theory and observation may be deemed satisfactory in view of the considerable irregularities and uncertainty in the experimentally observed structure. It is conceivable that a better agreement with experiment might be obtained by considering a different combination of interfaces, but such possibility will not be pursued here.

It is interesting to note that the dislocation walls bend or split within narrow transition layers separating regions A and B. The thickness of these layers is of the order of the wall spacing in the second-level fine laminates. While average deformations of the A and B bands may be expected to be rank-one compatible, as required to prevent long-range stresses, the strict compatibility within the bands requires the introduction of elastically strained boundary layers. The trade-off between refinement of the microstructure, which tends to decrease the elastic energy in the boundary layers, and the self-energy of the dislocation walls, which tends to increase with refinement, is addressed in the next section.

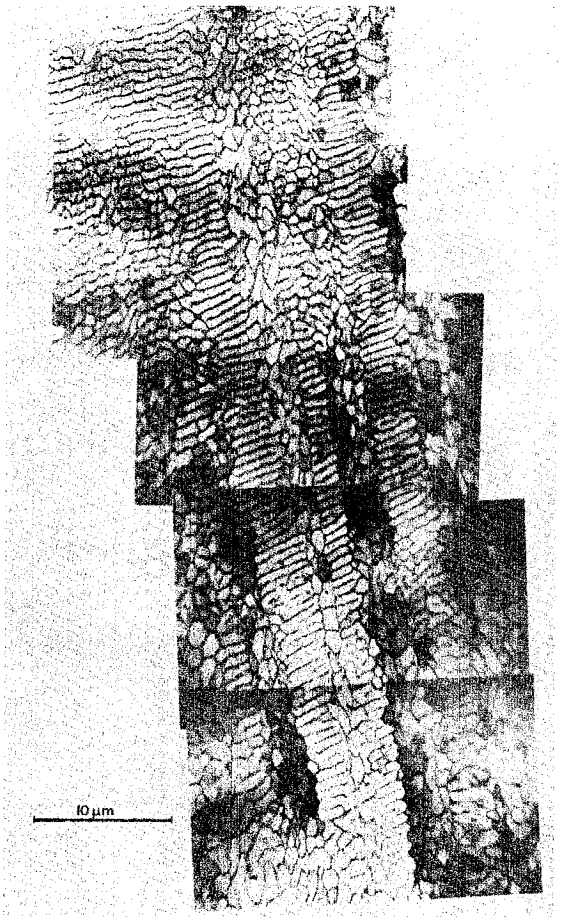

Figure 3.20: Nested bands of wall structure in a matrix of disoriented cells in polycrystal Cu fatigued to saturation [RP80].

3.6 Dislocation self-energy and scaling

The precise manner in which microstructural dimensions, such as laminate thicknesses and cell sizes, scale with various macroscopic variables has been the subject of considerable study. For instance, a widely accepted theory of cell size evolution is based on the assumption of "similitude," to wit, that a structure which is stable under a stress τ will be stable under a stress 2τ when shrunk to one-half its size. The similitude conjecture has been verified experimentally for a number of materials ([Han69]; [SH72]) and has been justified on the basis of energy minimization ([Hol70]; [SH72]; [KW70]; [KWvdM82]). Another scaling relation which holds for a wide range of materials and deformations states that the flow stress τ scales with the square root of the mean dislocation line density ρ ([OH66]; [MK81]). This law, in conjunction with similitude, implies that the dislocation cell size scales as $1/\sqrt{\rho}$.

The theory developed in the foregoing is purely local, i. e., it lacks an intrinsic length scale. As a consequence, the local theory furnishes no information regarding absolute microstructural dimensions or scaling laws such as just described. While a detailed study of these issues is beyond the scope of the present work, it is nevertheless of some immediate interest to demonstrate how the local theory can be extended in a physically meaningful manner so as to incorporate an intrinsic length scale commensurate with the crystal lattice parameter. In the local theory, dislocations are regarded as being continuously distributed with density $A(x)$ given by (3.97). The free energy density is given by (3.42) which accounts for the long-range elastic distortions of the lattice and, therefore, suffices to compute the dislocation interaction energy. However, the free energy density (3.42) does not account for the self-energy of the dislocations. Indeed, this energy scales with the dislocation length, the estimation of which requires the consideration of discrete dislocation lines and, consequently, an explicit acknowledgement of the discreteness of the lattice.

A nonlocal extension of the theory can be obtained–in the spirit of the so-called "sharp-interface" approximation ([Mod87]; [Ste88])–simply by adding to the free energy density (3.42) the self-energy density of the dislocations, which we proceed to

calculate. On the scale of the lattice, plastic slip occurs on discrete crystallographic planes in integer multiples of the Burgers vector ([Fon87]; [Fon88]; [CK88]). Consider a dislocation loop C of Burgers vector b on a slip plane of normal m. For simplicity, suppose that the crystal has slipped by b over the area Σ of the slip plane bounded by C. The corresponding microscopic plastic deformation is

$$F^p = I + b \otimes m\chi_\Sigma \delta(x \cdot m) \tag{3.149}$$

where χ_Σ is the characteristic function of Σ on the slip plane $x \cdot m = 0$. Inserting this expression into (3.97), a straightforward calculation gives

$$A(x) = b \otimes (\nu \times m)\delta_C(x) \tag{3.150}$$

where ν is the unit normal to C within the slip plane and $\delta_C(x)$ is the Dirac delta supported on C. The dislocation length contained in a volume Ω of the crystal is, therefore,

$$L = \int_\Omega \frac{|A|}{|b|} dx. \tag{3.151}$$

Let T denote the dislocation self-energy per unit length, or dislocation line tension. Assume, for simplicity, that T is independent of the orientation of the dislocation line. A commonly used expression for T is [KW89]

$$T = C\mu|b|^2 \tag{3.152}$$

where μ is an average shear modulus and C is a constant of the order of 0.3. The assumption of a well-defined line tension permits writing the self-energy of the dislocations as

$$E^{\text{self}} = TL = \int_\Omega \frac{T|A|}{|b|} dx \tag{3.153}$$

which, in view of (3.97), can be put in the form

$$E^{\text{self}} = \int_{\Omega} \frac{T}{|b|} |F^p \times \nabla| dx. \tag{3.154}$$

In this simple model, the self-energy density is

$$\phi^{\text{self}}(F^p \times \nabla) = \frac{T}{|b|} |F^p \times \nabla| \tag{3.155}$$

and the total free energy density follows from (3.42) and (3.155) as

$$\phi^{\text{total}} = \phi(FF^{p-1}, \gamma) + \phi^{\text{self}}(F^p \times \nabla) \tag{3.156}$$

which replaces (3.42). By way of example, consider a planar interface Π separating two uniformly deformed regions of the crystal. In view of (3.105), the corresponding self-energy density is

$$\phi^{\text{self}}(x) = \frac{T}{|b|} | \, [\![F^p]\!] \times N \, | \delta_{\Pi}(x). \tag{3.157}$$

Thus, the scalar

$$\Gamma = \frac{T}{|b|} | \, [\![F^p]\!] \times N \, | \tag{3.158}$$

plays the role of a surface energy for the interface. This is in close analogy to crystallographic twinning, where a surface energy can be assigned to the twin boundaries. We note that, in view of (3.152) and (3.158), the surface energy Γ vanishes in the formal limit of $|b| \to 0$.

Evidently, the self-energy $\phi^{\text{self}}(F^p \times \nabla)$ depends on the plastic deformation gradient and its inclusion in (3.156) renders the theory nonlocal. While in the local theory a periodic microstructure $F^p(x)$ can be scaled to $F^p(x/\epsilon)$ without affecting the energy density, the self-energy density is magnified by a factor of $1/\epsilon$. Thus, in the nonlocal theory an energy cost is incurred when the scale of the microstructure is refined.

This type of energy trade-offs have been extensively investigated in other contexts such as the mathematical theory of martensitic transformations [BJ87], and thin films [GO94]. In particular, Kohn and Müller [KM92] have shown that surface energy, in addition to setting an absolute length scale, can also influence the morphology of the microstructures, e.g., by promoting twin branching.

Dislocation walls in parallel arrays are often observed to be fairly uniformly spaced at a distance l of the order of 1 μm. Consideration of the dislocation self-energies yields a simple estimate of l. For simplicity, we assume that the geometry of the interfaces is not affected by the dislocation self-energy. From the standpoint of the local theory, a dislocation structure such as shown in Fig. 3.15a may be regarded as a member of a minimizing sequence $F_\epsilon(x)$ of compatible deformations, with $\epsilon = l/L$ and L a characteristic macroscopic dimension of the crystal such as the grain size. As mentioned earlier, compatibility between two laminates, or between a laminate and the boundary, generally requires the introduction of boundary layers of thickness $\sim l$ at their interface. The elastic energy in these boundary layers is of the order of $\mu\gamma^2 L^2 l$, where γ is a representative slip strain. From (3.152) and (3.158), the surface energy density Γ is of the order of $C\mu|b|\gamma$, while the surface energy of the crystal is of the order of $C\mu|b|\gamma L^3/l$. Assuming additivity of energies, the total energy of the crystal follows as

$$E^{\text{total}} = C_1\mu\gamma^2 L^2 l + C_2\mu|b|\gamma\frac{L^3}{l} \tag{3.159}$$

for some constants C_1 and C_2 of order unity. Minimization of E^{total} with respect to l gives

$$l = C_3\sqrt{\frac{|b|L}{\gamma}} \tag{3.160}$$

whereupon (3.159) becomes

$$E^{\text{total}} = C_4\mu\sqrt{|b|}\gamma^{3/2}L^{5/2} \tag{3.161}$$

for some constants C_3 and C_4 of order unity.

The scaling law $l \sim \gamma^{-1/2}$ is consistent with observations of the dependence of cell sizes on the applied strain [BK86]. The scaling laws $l \sim L^{1/2}$, $E^{\text{total}} \sim L^{5/2}$ were derived by Ball and James for martensite [BJ87] and can be improved by a self-similar construction involving branching [KM92]. Using $|b| = 2.56 \times 10^{-10}$ m, $\gamma = 2.5 \times 10^{-3}$ and $L = 10^{-5}$ m, as representative of fatigue in copper, (3.160) gives $l \sim 10^{-6}$ m, which is in the ball park of experimental observation.

3.7 Summary and discussion

Dislocation structures have been variously investigated by considering ensembles of discrete dislocations and minimizing their interaction energy ([Neu86]; [LBN93]); or by seeking dipolar walls satisfying Frank's minimum energy condition ([Fra50]; [HL68]; [BS86]). Here we have pursued a different line of inquiry based on direct methods of the calculus of variations. These methods seek to characterize solutions directly as energy minimizers, instead of as solutions of the Euler equations of the energy functional. We part company with the majority of investigations of low energy dislocation structures by placing primary emphasis on *deformation* microstructures and regarding the dislocations as manifestations of the incompatibility of the plastic deformation gradient field. Within this framework, we show that the incremental displacements of inelastic solids follow as minimizers of a suitably defined pseudoelastic energy function. In crystals exhibiting latent hardening, the energy function is nonconvex and has wells corresponding to single slip deformations. This favors microstructures consisting locally of single slip. Several deformation microstructures constructed in accordance with this prescription have been shown to be in correspondence with commonly observed dislocation structures. Finally, we have shown that a characteristic length scale can be built into the theory by taking into account the self energy of the dislocations. The extended theory leads to scaling laws which appear to be in good qualitative and quantitative agreement with observation.

It is noteworthy that the fundamental factor determining the development of dis-

location structures is the lack of convexity of the incremental energy functional. The connection between lack of convexity and the emergence of fine microstructure is presently well-established in a number of applications such as martensitic transformations, micromagnetics, liquid crystals and thin films. From this perspective, the overriding emphasis once placed on formulating constitutive restrictions guaranteeing existence and uniqueness of solutions of boundary value problems seems somewhat misplaced. For instance, Drucker's celebrated postulates (see, e.g., [Lub90]) are equivalent to the assumption of convexity of the incremental boundary value problem and, consequently, guarantee existence, uniqueness and regularity of classical minimizers (e.g., [Dac89]). Thus, while convexity may be desirable in structural applications, it has the unfortunate effect of ruling out solutions with fine microstructure. Therefore, the case of primary interest as regards the investigation of microstructural development concerns precisely those materials which *do not* obey Drucker's postulates. This new constitutive paradigm represents a sharp – and refreshing – departure from classical plasticity theory.

A number of open questions remain to be addressed. For instance, it is not known to us what rules—if any—govern the turns and bends in labyrinth structures; or whether cell structures may also be understood as compatible arrangements of regions of single slip. In addition, it would be desirable to have constructions enabling the determination of energy-minimizing microstructures for general deformation histories. The question of scaling laws and their relation to nonlocal extensions of the theory has merely been touched upon in this paper and is in need of much further development. These present uncertainties notwithstanding, it is hoped that the theory formulated in this paper will provide a convenient basis for a rigorous and systematic mathematical investigation of the effective behavior of ductile single crystals with microstructure.

Chapter 4 Conclusions and future work

A micromechanically based model for F.C.C. metals subject to cyclic loads oriented for single slip has been developed. The model accounts for crystal plasticity, and two hardening mechanisms: a) dislocation trapping for the main slip system and b) forest pinning for the secondary systems, and dipole annihilation in the PSBs with the attendant vacancy production. The vacancy production was found to be responsible for the elongation of the PSB. A vacancy diffusion model has also been implemented and the outward flux of vacancies through the free surface is found to be partly responsible for the grooving process. Finite element simulations have been performed in order to check the feasibility of the postulated mechanisms taken into account. The results obtained show good agreement with published experimental data. Crack nucleation sites have been identified and number of cycles to failure estimated.

Future work in this field should include: multiple PSBs simulations, which is a possible mechanism for intrusions; analysis of the influence of the load orientation on the surface profile and life expectancy; a model of the development of PSBs from a uniform matrix; influence of temperature and environmental effects; extension to alloys; analysis of polycrystals, where failure is caused by the nucleation of a fatigue crack at a grain on the surface and its propagation into the bulk; the influence of grain-boundary structures, in particular high-angle boundaries where crack nucleation has been observed. More experimental data is needed to fully understand all the underlying mechanics, especially if three-dimensional models are desired.

In the second part of this thesis, chapter 3, a non-convex energy funtion has been found to underlie the formation of microstructures in F.C.C crystals subject to fatigue loads. It has been determined that non-convexity, which is due to latent hardening and geometrical softening, favors single-slip variants over uniform multi-slip deformation. It has also been found that the interfaces between the single-slip variants are in good agreement with published TEM observations of cells, walls and

labyrinth structures. The "patchy slip" phenomena has been effectively explained, but additional work is needed to understand features such as the intersection between walls and gaps in the walls. Incremental numerical models, with latent hardening values obtained from experiment, may also be implemented to simulate the evolution of the microstructure with deformation.

Bibliography

[ABW76] J. G. Antonopoulos, L. M. Brown, and A. T. Winter. Vacancy dipoles in fatigued copper. *Philosophical Magazine*, 34:549–563, 1976.

[Aif87] E. C. Aifantis. The physics of plastic deformation. *International Journal of Plasticity*, 3:211–247, 1987.

[AKLM84] F. Ackermann, L.P. Kubin, J. Lepinoux, and H. Mughrabi. The Dependence of Dislocation Microstructure on Plastic Strain Amplitude in Cyclically Strained Copper Single Crystals. *Acta Metallurgica*, 32:715–725, 1984.

[Alb38] W.A.J. Albert. Arch. Miner. Geognoise Berg. *Hüttenkunde*, 10:215, 1838.

[AR77] R. J. Asaro and J. R. Rice. Strain localization in ductile single crystals. *Journal of the Mechanics and Physics of Solids*, 25:309, 1977.

[Asa79] R. J. Asaro. Geometrical Effects in the Inhomogeneous Deformation of Ductile Single Crystals. *Acta Metallurgica*, 27:445–453, 1979.

[Asa83] R. J. Asaro. Micromechanics of Crystals and Polycrystals. *Advances in Applied Mechanics*, 23:1–115, 1983.

[AW76] J.G. Antonopoulos and A.T. Winter. Weak beam study of dislocation structures in fatigued copper. *Philosophical Magazine*, 33:87–95, 1976.

[BBH69] S. J. Basinski, Z. S. Basinski, and A. Howie. Early stages of fatigue in copper single crysta. *Philosophical Magazine*, 19:899–924, 1969.

[BBT85] L. Boulanger, A. Bisson, and A. A. Tavassoli. Labyrinth structure and persistent slip bands in fatigued 316 stainless steel. *Philosophical Magazine*, A51:L5–L11, 1985.

[BCJ95] J. M. Ball, C. Chu, and R. D. James. Hysteresis during stress-induced variant rearrangement. *Journal de Physique IV*, 5:C8–245–C8–251, 1995.

[BG79] R. W. Balluffi and A. V. Granato. Dislocations, vacancies and instertitials. In F.R.N. Nabarro, editor, *Dislocations in Solids*, volume 4, Dislocations in Metallurgy, New York, 1979. North-Holland.

[BH59] T. Broom and R. K. Ham. The hardening of copper single crystals by fatigue. *Proceedings of the Royal Society of London*, A 251:186–199, 1959.

[BH82] A. N. Brooks and T. J. R. Hughes. Streamline Upwind Petrov-Galerkin Formulations for Convection Dominated Flows with Particular Emphasis on the Incompressible Navier-Stokes Equations. *Computer Methods in Applied Mechanics and Engineering*, 32 (1-3):199–259, 1982.

[Bha91] K. Bhattacharya. Wedge-like microstructure in martensites. *Acta Metallurgica et Materialia*, 39:2431–2444, 1991.

[Bha92] K. Bhattacharya. Self-accommodation in martensite. *Archive for Rational Mechanics and Analysis*, 120:201–244, 1992.

[BJ87] J. M. Ball and R. D. James. Fine Phase Mixtures as Minimizers of Energy. *Archive for Rational Mechanics and Analysis*, 100:13–52, 1987.

[BK86] M.N. Bassim and R.J. Klassen. Variation in Dislocation Cell Size with Local Strain in a Low Alloy Steel. *Materials Science and Engineering*, 81:163–167, 1986.

[BKB80] Z. S. Basinski, A. S. Korbel, and S. J. Basinski. The temperature dependence of the saturation stress and dislocation structure in fatigued copper single crystals. *Acta Metallurgica*, 28:191–207, 1980.

[BM65] R. C. Boettner and A. J. McEvily. Fatigue slip band formation in silicon-iron. *Acta Metallurgica*, 13:937, 1965.

[BO54] W. Boas and G. J. Ogilvie. The Plastic Deformation of a Crystal in a Polycrystalline Aggregate. *Acta Metallurgica*, 2:655–659, 1954.

[BO85] L. M. Brown and S. L. Ogin. Role of internal stresses in the nucleation of fatigue cracks. In B. A. Bilby, K. J. Miller, and J. R. Willis, editors, *Fun-*

damentals of deformation and fracture : Eshelby memorial symposium, pages 501–528, New York, 1985. Cambridge University Press.

[Bou83] J. Boutin. PhD thesis, École Polytechnique de Montréal, Canada, 1983.

[BPB83] Z. S. Basinski, R. Pascual, and S. J. Basinski. Low amplitude fatigue of copper single crystals –I The role of surface in fatigue failure. *Acta Metallurgica*, 31:591–602, 1983.

[BS86] J. B. Bilde-Sorensen. Deformation bands in ¡120¿ grains in coarse-grained aluminum. *Materials Science and Engineering*, 81:211–216, 1986.

[BW91a] J. L. Bassani and T. Y. Wu. Latent hardening in single crystals. 1. Theory and experiments. *Proceedings of the Royal Society of London*, A435:1–19, 1991.

[BW91b] J. L. Bassani and T. Y. Wu. Latent hardening in single crystals. 2. Analytical characterization and predictions. *Proceedings of the Royal Society of London*, A435:21–41, 1991.

[Cah51] R. W. Cahn. *Journal of the Institute of Metals*, 79:129, 1951.

[CF57] P. Coulomb and J. Friedel. *Dislocations and Mechanical Properties of Crystals.* Wiley, New York, 1957.

[CH57] A. H. Cottrell and D. Hull. Extrusion and intrusion by cyclic slip in copper. *Proceedings of the Royal Society of London*, A 242:211–213, 1957.

[Cha81] P. Charsley. Dislocation arrangements in polycrystalline copper alloys fatigued to saturation. *Materials Science and Engineering*, 47:181–185, 1981.

[CK88] M. Chipot and D. Kinderlehrer. Equilibrium configurations of crystals. *Archive for Rational Mechanics and Analysis*, 103:237–277, 1988.

[CL81] A. S. Cheng and C. Laird. Fatigue life behavior of copper single crystals. Part I: Observations of crack nucleation. *Fatigue of Engineering Materials and Structures*, 4:331–341, 1981.

[CL95] P. M. Chaikin and T. C. Lubensky. *Principles of condensed matter physics.* Cambridge University Press, Cambridge, England, 1995.

[CM76] P. Carter and J. B. Martin. Work bounding functions for plastic materials. *Journal of Applied Mechanics*, 98:434–438, 1976.

[CnO92] A. M. Cuitiño and M. Ortiz. Computational Modelling of Single Crystals. *Modelling and Simulation in Materials Science and Engineering*, 1:255–263, 1992.

[CnO93] A. M. Cuitiño and M. Ortiz. Constitutive Modeling of $L1_2$ Intermetallic Crystals. *Materials Science and Engineering*, A170:111–123, 1993.

[CnO96] A. M. Cuitiño and M. Ortiz. Ductile Fracture by Vacancy Condensation in FCC Single Crystals. *Acta Metallurgica*, 44 (2):427–436, 1996.

[Cof54] L.F. Coffin. A study of the effects of cyclic thermal stresses on a ductile metal. *Transactions of the ASME*, 76:931–950, 1954.

[CP69] G. Crandall and A. Pazy. Semi-groups of nonlinear contractions and dissipative sets. *Journal of Functional Analysis*, 6:376–418, 1969.

[CP70] G. Crandall and A. Pazy. On accretive sets in Banach spaces. *Journal of Functional Analysis*, 5:204–217, 1970.

[Dac89] B. Dacorogna. *Direct Methods in the Calculus of Variations.* Springer-Verlag, New York, 1989.

[DBL86] J. I. Dickson, J. Boutin, and G. L'Epeŕance. An explanation of labyrinth walls in fatigued FCC metals. *Acta Metallurgica*, 34:1505–1514, 1986.

[DEM86] K. Differt, U. Essmann, and H. Mughrabi. A model of extrusions and intrusions in fatigued metals. II. Surface roughening by random irreversible slip. *Philosophical Magazine*, A 54, 2:237–258, 1986.

[DHL86] J. I. Dickson, L. Handfield, and G. L'Epeŕance. Geometrical factors influencing the orientations of dipolar dislocation structures produced by cyclic deformation of fcc metals. *Materials Science and Engineering*, 81:477–492, 1986.

[EGM81] U. Essmann, U. Gösele, and H. Mughrabi. A model of extrusions and intrusions in fatigued metals. I. Point-defect production and the growth of extrusions. *Philosophical Magazine*, A 44:405–426, 1981.

[EH03] J. A. Ewing and J. C. Humfrey. The fracture of metals under rapid alterations of stress. *Philosophical Transactions of the Royal Society of London A*, 200:241–250, 1903.

[Eri80] J. L. Ericksen. Some phase transitions in crystals. *Archive for Rational Mechanics and Analysis*, 73:99–124, 1980.

[Fai64] W. Fairbairn. Experiments to determine the effect of impact, vibratory action, and long continued changes of load on wrought iron girders. *Proceedings of the Royal Society of London*, 154:311, 1864.

[FBZ80] P. Franciosi, M. Berveiller, and A. Zaoui. Latent hardening in copper and aluminium single crystals. *Acta Metallurgica*, 28:273, 1980.

[Fel65] C. E. Feltner. A debris mechanism of cyclic strain hardening for FCC metals. *Philosophical Magazine*, A 12:1229–1248, 1965.

[FL75] J. M. Finney and C. Laird. Strain localization in cyclic deformation of copper single crystals. *Philosophical Magazine*, A 31:339–366, 1975.

[FM66] A. J. E. Foreman and M. J. Makin. Dislocation Movement through Random Arrays of Obstacles. *Philosophical Magazine*, 14:911, 1966.

[FM67] A. J. E. Foreman and M. J. Makin. Dislocation movement through random arrays of obstacles. *Canadian J. Phys.*, 45:273, 1967.

[FMP74] N.E. Frost, K.J. Marsh, and L.P. Pook. *Metal Fatigue.* Clarendon Press, Oxford, UK, 1974.

[Fon87] I. Fonseca. Variational methods for elastic crystals. *Archive for Rational Mechanics and Analysis*, 97:189–220, 1987.

[Fon88] I. Fonseca. The Lower Quasiconvex Envelope of the Stored Energy Function for an Elastic Crystal. *J. Math. Pures et Appl.*, 67:175–195, 1988.

[For53] P. J. E. Forsyth. Exudation of material from slip bands at the surface of fatigued crystals of an aluminium-copper alloy. *Nature*, 171:172–173, 1953.

[For57] P. J. E. Forsyth. Slip band damage and extrusion. *Proceedings of the Royal Society of London*, A 242:198–202, 1957.

[Fra50] F. C. Frank. Proceedings of the Pittsburgh Symposium on the Plastic Deformation of Crystalline Solids. Technical report, Office of Naval Research, Washington, DC, 1950.

[Fra85a] P. Franciosi. F.C.C. single crystals hardening: anisotropy and stacking fault energy. In *ICSMA Symp.*, page 281, Montreal, Canada, 1985.

[Fra85b] P. Franciosi. The concepts of latent hardening and strain hardening in metallic single crystals. *Acta Metallurgica*, 33:1601, 1985.

[Fra88] P. Franciosi. On flow and work hardening expression correlations in metallic single crystal plasticity. *Revue Phys. Appl.*, 23:383, 1988.

[FS55] P. J. E. Forsyth and C. A. Stubbington. The slip band extrusion effect observed in some aluminum alloys subjected to cyclic stresses. *Journal of the Institute of Metals*, 83:395, 1955.

[FW59] J. T. Fourie and H. Wilsdorf. A study of slip lines in α-brass as revealed by the electron microscope. *Acta Metallurgica*, 7:339–349, 1959.

[FZ82] P. Franciosi and A. Zaoui. Multislip in F.C.C. crystals: A theoretical approach compared with experimental data. *Acta Metallurgica*, 30:1627, 1982.

[FZ83] P. Franciosi and A. Zaoui. Glide mechanisms in B.C.C. crystals: an investigation of the case of α-iron through multislip and latent hardening tests. *Acta Metallurgica*, 31:1331, 1983.

[Gea71] C. W. Gear. *Numerical Initial Value Problems in Ordinary Differential Equations.* Prentice-Hall, Englewood Cliffs, N. J., 1971.

[GLL95] M. Glazov, L. M. Llanes, and C. Laird. Self-organized dislocation-structures (SODS) in fatigued metals. *Physica Status Solidi*, A 149:297–321, 1995.

[GM75] J. C. Grosskreutz and H. Mughrabi. Description of the work-hardened structure at low temperature in cyclic deformation. In A.S. Argon, editor, *Constitutive Equations in Plasticity*, pages 251–326, Cambridge, Mass, 1975. MIT Press.

[GO94] G. Gioia and M. Ortiz. The morphology and folding patterns of buckling-driven thin-film blisters. *Journal of the Mechanics and Physics of Solids*, 42:531–559, 1994.

[Gou33] H. J. Gough. Crystalline structure in relation to failure of metals – especially by fatigue. *Edgar Marburg Lecture, Proceedings of the American Society for Testing of Materials*, 33, Part II:3–114, 1933.

[GS32] H.J. Gough and D.G. Sopwith. Atmospheric action as a factor in fatigue of metals. *Journal of the Institute of Metals*, 49:93–122, 1932.

[Gur81] M.E. Gurtin. *An introduction to continuum mechanics.* Academic Press, New York, 1981.

[Han55] R. F. Hanstock. Fatigue phenomena in high-strength aluminium alloys. *Journal of the Institute of Metals*, 83:11, 1955.

[Han69] N. Hansen. *Transactions of the Metallurgical Society of the AIME*, 245:2061, 1969.

[Hav73] K. S. Havner. On the mechanics of crystalline solids. *Journal of the Mechanics and Physics of Solids*, 21:383, 1973.

[HD78] H. N. Hahn and D. J. Duquette. The effect of surface dissolution on fatigue deformation and crack nucleation in copper and copper 8% aluminum single crystals. *Acta Metallurgica*, 26:279, 1978.

[Hem59] M. Hempel. Slip bands, twins and precipitation processes in fatigue stressing. In B.L. Averbach, D.K. Felbeck, G.T. Hahn, and D.A. Thomas, editors, *Fracture*, pages 376–411, Cambridge, Mass., 1959. MIT Press.

[HG69] J.R. Hancock and J.C. Grosskreutz. Mechanisms of fatigue hardening in copper single crystals. *Acta Metallurgica*, 17:77–97, 1969.

[HH75] R. Hill and J. W. Hutchinson. Bifurcation Phenomena in the Plane Strain Tension Test. *Journal of the Mechanics and Physics of Solids*, 23:239–264, 1975.

[HKW86] N. Hansen and D. Kuhlmann-Wilsdorff. Low Energy Dislocation Structures due to Unidirectional Deformation at Low Temperatures. *Materials Science and Engineering*, 81:141–161, 1986.

[HL68] J. P. Hirth and J. Lothe. *Theory of Dislocations.* McGraw-Hill, New York, 1968.

[HN86] A. Hunsche and P. Neumann. Quantitative measurement of persistent slip band profiles and crack initiation. *Acta Metallurgica*, 34:207–217, 1986.

[Hod49] E.A. Hodgkinson. Report of the commissioners appointed to enquire into the application of iron to railway structures. Technical Report Command Paper N^0 1123, His Majesty's Stationery Office, London, 1849.

[Hol70] D. L. Holt. *Journal of Applied Physics*, 41:3197, 1970.

[HR72] R. Hill and J. R. Rice. Constitutive analysis of elastic-plastic crystals at arbitary strains. *Journal of the Mechanics and Physics of Solids*, 20:401, 1972.

[HTN86] K. Higashida, J. Takamura, and N. Narita. The Formation of Deformation Bands in f.c.c. Crystals. *Materials Science and Engineering*, 81:239–258, 1986.

[Hug87] T. J. R. Hughes. *The finite element method : linear static and dynamic finite element analysis.* Prentice-Hall, Englewood Cliffs, N.J., 1987.

[JD66] D. Jones and W. D. Dover. Enhanced diffusion rates during the fatigue of metals. *Nature, London*, 209:704, 1966.

[Jin83] N. Y. Jin. Dislocation–structures in fatigued copper single–crystals oriented for double–slip. *Philosophical Magazine*, 48:L33, 1983.

[Jin87] N.Y. Jin. Dislocation structures in cyclically deformed [011] copper crystals. *Philosophical Magazine Letters*, 56:23–28, 1987.

[JJ65] E. W. Johnson and H. H. Johnson. Imperfection density of fatigued and annealed copper via electrical resistivity measurements. *Transactions of the Metallurgical Society of the AIME*, 233:1333–1339, 1965.

[JW84a] N. Y. Jin and A. T. Winter. Dislocation structures in cyclically deformed [001] copper crystals. *Acta Metallurgica*, 32:1173–1176, 1984.

[JW84b] N. Y. Jin and T. Winter. Cyclic deformation of copper single crystals oriented for double slip. *Acta Metallurgica*, 32:989–995, 1984.

[KB78] R. Kwadjo and L. M. Brown. Cyclic hardening of magnesium single crystals. *Acta Metallurgica*, 26:1117–1132, 1978.

[KM92] R. V. Kohn and S. Müller. Branching of Twins near an Austenite-Twinned-Martensite Interface. *Philosophical Magazine*, A66:697–715, 1992.

[Koc60] U. F. Kocks. *Acta Metallurgica*, 8:345, 1960.

[Koc64] U. F. Kocks. Latent hardening and secondary slip in aluminum and silver. *Transactions of the Metallurgical Society of the AIME*, 230:1160, 1964.

[Koc66] U. F. Kocks. A statistical theory of flow stress and work-hardening. *Philosophical Magazine*, 13:541, 1966.

[Koh91] R.V. Kohn. The relaxation of a double-well energy. *Continuum Mechanics and Thermodynamics*, 3:193–236, 1991.

[KOK+77] K. Katigiri, A. Omura, K. Koyanagi, J. Awatani, T. Shiraishi, and H. Kaneshiro. Early stage crack tip morphology in fatigued copper. *Metallurgical Transactions A*, 8:1769–1773, 1977.

[KS86] R. V. Kohn and G. Strang. Optimal design and relaxation of variational problems, I, II and III. *Communications on Pure and Applied Mathematics*, 39:113–137, 139–182, 353–377, 1986.

[KW70] D. Kuhlmann-Wilsdorff. *Metallurgical Transactions*, 1:3173, 1970.

[KW79] D. Kuhlmann-Wilsdorf. Dislocation behavior in fatigue. IV. Quantitative interpretation of friction stress and back stress derived from hysteresis loops. *Materials Science and Engineering*, 39:231–245, 1979.

[KW89] D. Kuhlmann-Wilsdorf. Theory of plastic deformation: properties of low energy dislocation structures. *Materials Science and Engineering*, A113:1, 1989.

[KWL80] D. Kuhlmann-Wilsdorf and C. Laird. Dislocation behavior in fatigue. V. Breakdown of loop patches and formation of persistent slip bands and dislocation walls. *Materials Science and Engineering*, 46:209–219, 1980.

[KWvdM82] D. Kuhlmann-Wilsdorff and J. H. van der Merwe. Theory of dislocation cell sizes in deformed metals. *Materials Science and Engineering*, 55:79, 1982.

[KZ73] I. Kovács and L. Zsoldos. *Dislocation and plastic deformation.* Pergamon Press, Oxford, 1973.

[Lai76] C. Laird. The fatigue limits of metals. *Materials Science and Engineering*, 22:231–236, 1976.

[LBN93] V. A. Lubarda, J. A. Blume, and A. Needleman. An Analysis of Equilibrium Dislocation Distributions. *Acta Metallurgica et Materialia*, 41:625–642, 1993.

[LCM86] C. Laird, P. Charsley, and H. Mughrabi. Low energy dislocation structures produced by cyclic deformation. *Materials Science and Engineering*, 81:433–450, 1986.

[Lee69] E. H. Lee. Elastic-plastic deformation at finite strains. *Journal of Applied Mechanics*, 36:1, 1969.

[Lin92] T.H. Lin. Micromechanics of crack initiation in high cycle fatigue. *Advances in Applied Mechanics*, 29:2–62, 1992.

[LKK84] T. K. Lepistö, V. T. Kuokkala, and P. O. Kettunen. Dislocation arrangements in cyclically deformed copper single crystals. *Materials Science and Engineering*, 81:457–463, 1984.

[LKK86] T. K. Lepistö, V. T. Kuokkala, and P. O. Kettunen. Dislocation arrangements in cyclically deformed copper single crystals. *Materials Science and Engineering*, 81:457–463, 1986.

[Lub72] J. Lubliner. On the Thermodynamic Foundations of Non-Linear Solid Mechanics. *International Journal of Non-Linear Mechanics*, 7:237–254, 1972.

[Lub73] J. Lubliner. On the Structure of the Rate Equations of Materials with Internal Variables. *Acta Mechanica*, 17:109–119, 1973.

[Lub90] J. Lubliner. *Plasticity Theory.* Macmillan Publishing Company, New York, 1990.

[LVD86] G. L'Esperance, J. B. Vogt, and J. L. Dickson. The identification of labyrinth wall orientations in cyclically deformed AISI-SAE 316 stainless steel. *Materials Science and Engineering*, 79:141–147, 1986.

[LW75] R. L. Lyles and H. G. F. Wilsdorf. Microcrack Nucleation and Fracture insilver Crystals. *Acta Metallurgica*, 23:269–277, 1975.

[LWMC89] C. Laird, Z. Wang, B. T. Ma, and H. F. Chai. Low energy dislocation structures produced by cyclic softening. *Materials Science and Engineering*, A113:245–257, 1989.

[MAH79] H. Mugharbi, F. Ackermann, and K. Herz. Persistent slip bands in fatigued face-centered and body-centered cubic metals. Technical report, American Society for Testing and Materials, Philadelphia, 1979.

[Mai69] G. Maier. Some theorems for plastic strain rates and plastic strains. *Journal de Mécanique*, 8:5, 1969.

[Man72] J. Mandel. Plasticité classique et viscoplasticité. Technical report, Lecture Notes, Int. Centre for Mech. Sci., Udine, Berlin:Springer, 1972.

[May60] A. N. May. A model of metal fatigue. *Nature, London*, 185:303–304, 1960.

[MB82] K. Mecke and C. Blochwitz. Saturation dislocation structures in clyclically deformed nickel single crystals of different orientations. *Crystal Research and Technology*, 17:743–758, 1982.

[MH85] A. Mizukami and T. J. R. Hughes. A Petrov-Galerkin Finite Element Method for Convection Dominated Flows - An Accurate Upwinding Technique for Satisfying the Maximum Principle. *Computer Methods in Applied Mechanics and Engineering*, 50 (2):181–193, 1985.

[Min45] M.A. Miner. Cumulative damage in fatigue. *Journal of Applied Mechanics*, 12:159–164, 1945.

[MK81] H. Mecking and U. F. Kocks. *Acta Metallurgica*, 29:1865, 1981.

[ML89a] B. T. Ma and C. Laird. Overview of fatigue behavior in copper single crystals – I. Surface morphology and stage I crack initiation sites for tests at constant strain amplitude. *Acta Metallurgica*, 37:325–336, 1989.

[ML89b] B. T. Ma and C. Laird. Overview of fatigue behavior in copper single crystals – II. Population, size, distribution and growth kinetics of stage I crack for tests at constant strain amplitude. *Acta Metallurgica*, 37:337–348, 1989.

[MN90] T. Mura and Y. Nakasone. A theory of fatigue crack initiation is solids. *Journal of Applied Mechanics*, 57:1–6, 1990.

[Mod87] L. Modica. Gradient theory of phase transitions and minimal interface criterion. *Archive for Rational Mechanics and Analysis*, 98:123–142, 1987.

[Mor62] J.J. Moreau. Décomposition orthogonale dans un espace Hilbertien selon deux cônes mutuellement polaires. *C. R. Acad. Sci. Paris*, 255:233–240, 1962.

[Mor63] J.J. Moreau. Fonctionnelles sous-différentiables. *C. R. Acad. Sci. Paris*, 257:4117–4119, 1963.

[Mor65] J.J. Moreau. Proximité et dualité dans un space Hilbertien. *Bull. Soc. Math. France*, 93:273–299, 1965.

[Mor66] J.J. Moreau. Convexity and duality. In E.R. Caianello, editor, *Functional Analysis and Optimization*, pages 145–169. Academic Press, 1966.

[Mor67] J.J. Moreau. Fonctionelles convexes. Séminaires sur les equations à dérivées partielles, Collége de France, 1967.

[Mor70] J.J. Moreau. Sur les lois de frottement, de plasticité et de viscosité. *C. R. Acad. Sci. Paris*, 271:608–611, 1970.

[Mor71] J.J. Moreau. Sur l'evolution d'un système elasto-visco-plastique. *C. R. Acad. Sci. Paris*, 273:118–121, 1971.

[Mor74] J.J. Moreau. On unilateral constraints, friction and plasticity. In G. Capriz and G. Stampacchia, editors, *New Variational Techniques in Mathematical Physics*, pages 175–322. Centro Internazionale Matematico Estivo, II Ciclo 1973, Edizioni Cremonese, Roma, 1974.

[Mor76] J.J. Moreau. Application of convex analysis to the treatment of elastoplastic systems. In P. Germain and B. Nayroles, editors, *Applications of Methods of Functional Analysis to Problems in Mechanics*. Springer-Verlag, 1976.

[MP66] J. B. Martin and A. R. S. Ponter. A note on a work inequality in linear viscoelasticity. *Quarterly of Applied Mathematics*, 24:161, 1966.

[Mug78] H. Mughrabi. The cyclic hardening and saturation behaviour of copper single crystals. *Materials Science and Engineering*, 33:207–223, 1978.

[Mug80] H. Mughrabi. Microscopic mechanisms of metal fatigue. In P. Haasen, V. Gerold, and G. Kostorz, editors, *The Strength of Metals and Alloys*, pages 1615–1639, Oxford, 1980. Pergamon Press.

[Mug81] H. Mughrabi. Cyclic plasticity of matrix and persistent slip bands in fatigued metals. In O. Brulin and R. K. T. Hsieh, editors, *Continuum Models of Discrete Systems*, volume 4, pages 241–257, London, 1981. North-Holland.

[Mur87] T. Mura. *Micromechanics of defects in solids*. Kluwer Academic Publishers, Boston, 1987.

[Nab67] F. R. N. Nabarro. *Theory of crystal dislocations*. Oxford Univeristy Press, Oxford, England, 1967.

[Neu86] P. Neumann. Low Energy Dislocation Configurations: A Possible Key to the Understanding of Fatigue. *Materials Science and Engineering*, 81:465–475, 1986.

[NVF77] P. Neumann, V. Vehoff, and H. Fuhlrott. On the mechanisms of fatigue crack growth. In D. M. R. Taplin, editor, *Fourth International Conference on Fracture. Fracture 1977*, volume 2, page 1313, Oxford, 1977. Pergamon Press.

[Nye53] J. F. Nye. Some geometrical relations in dislocated crystals. *Acta Metallurgica*, 1:153–162, 1953.

[OH66] H. M. Otte and J. J. Hren. *Experimental Mechanics*, 6:177, 1966.

[OP82] M. Ortiz and E. P. Popov. A Statistical Theory of Polycrystalline Plasticity. *Proceedings of the Royal Society of London*, A379:439–458, 1982.

[Ort81] M. Ortiz. *Topics in constitutive theory for inelastic solids.* PhD thesis, University of California at Berkeley, Berkeley, California, 1981.

[PAN82] D. Pierce, R.J. Asaro, and A. Needleman. An Analysis of Nonuniform and Localized Deformation in Ductile Single Crystals. *Acta Metallurgica*, 30:1087–1119, 1982.

[PCC55] G. R. Piercy, R. W. Cahn, and A. H. Cottrell. A Study of Primary and Conjugate Slip in Crystals of alpha-Brass. *Acta Metallurgica*, 3:331–338, 1955.

[PE63] P.C. Paris and F. Erdogan. A critical analysis of crack propagation laws. *Journal of Basic Engineering*, 85:528–534, 1963.

[PE92] D. A. Porter and K. E. Easterling. *Phase Transformations in Metals and Alloys.* Chapman and Hall, London, UK, 1992.

[Ped93] P. Pedregal. Laminates and microstructure. *European Journal of Applied Mathematics*, 4:121–149, 1993.

[PGA61] P.C. Paris, M.P. Gomez, and W.P. Anderson. A rational analytic theory of fatigue. *The trend in engineering*, 13:9–14, 1961.

[Pol70] J. Polák. The effect of intermediate annealing on the electrical resistivity and shear stress of fatigued copper. *Scripta Metallurgica*, 4:761–764, 1970.

[PVMZ87] J. Peraire, M. Vahdati, K. Morgan, and O. C. Zienkiewicz. Adaptive Remeshing for Compressible Flow Computations. *Journal of Computational Physics*, 72:449–466, 1987.

[RH66] R. Roberge and H. Herman. Fatigue - Generation of vacancies. *Nature, London*, 211:178, 1966.

[Ric71] J. R. Rice. Inelastic constitutive relations for solids: an internal-variable theory and its applications to metal plasticity. *Journal of the Mechanics and Physics of Solids*, 19:433, 1971.

[Ric75] J. R. Rice. Continuum mechanics and thermodynamics of plasticity in relation to microscale deformation mechanisms. In A.S. Argon, editor, *Constitutive Equations in Plasticity*, pages 23–79, Cambridge, Mass, 1975. MIT Press.

[RKC65] B. Ramaswami, U. F. Kocks, and B. Chalmers. Latent hardening in silver and Ag-Au alloy. *Transactions of the Metallurgical Society of the AIME*, 233:927, 1965.

[RO97] E. A. Repetto and M. Ortiz. A micromechanical model of fatigue-crack nucleation in f. c. c. metals. *Acta Materialia*, 45:2577–2595, 1997.

[Roc70] R.T. Rockafellar. *Convex analysis.* Princeton University Press, Princeton, N.J., 1970.

[RP80] K.V. Rasmussen and O.B. Pedersen. Fatigue of Copper Polycrystals at Low Plastic Strain Amplitudes. *Acta Metallurgica*, 28:1467–1478, 1980.

[RW89] J. R. Rice and J. S. Wang. Embrittlement of interfaces by solute segregation. *Materials Science and Engineering*, A107:23–40, 1989.

[Sai63] S. Saimoto. *Low Temperature Tensile Deformation of Copper Single Crystals Oriented for Multiple Slip.* PhD thesis, M. I. T., Cambridge, Mass., 1963.

[SB61] E. Schmid and N. Boas. *Kristall. Plastizität.* Springer, Berlin, 1961.

[SH72] M. R. Staker and D. L. Holt. *Acta Metallurgica*, 1972:569, 1972.

[Sil89] S. Silling. Phase changes induced by deformation in isothermal elastic crystals. *Journal of the Mechanics and Physics of Solids*, 37:293–316, 1989.

[SL69] J. F. Soechting and R. H. Lance. A bounding principle in the theory of work-hardening plasticity. *Journal of Applied Mechanics*, 36:228, 1969.

[Ste66] J. W. Steeds. *Proceedings of the Royal Society of London*, A292:343, 1966.

[Ste88] P. Sternberg. The Effect of a Singular Perturbation on Nonconvex Variational Problems. *Archive for Rational Mechanics and Analysis*, 101:209–260, 1988.

[Sur91] S. Suresh. *Fatigue of Materials.* Cambridge University Press, Cambridge, England, 1991.

[Teo69] C. Teodosiu. A dynamic theory of dislocations and its applications to the theory of the elastic-plastic continuum. In J. A. Simmons, editor, *Conf. Fundamental Aspects of Dislocation Theory*, volume 2, page 837, Washington, 1969. Natl. Bureau of Standards Special Publication.

[Teo82] C. Teodosiu. *Elastic Models of Crystal Defects.* Springer-Verlag, New York, 1982.

[TM81] K. Tanaka and T. Mura. A dislocation model for fatigue crack initiation. *Journal of Applied Mechanics*, 48:97–102, 1981.

[TWL56] N. Thompson, N. J. Wadsworth, and N. Louat. The origin of fatigue crack in copper. *Philosophical Magazine*, 1:113–126, 1956.

[TZ95] L. Truskinovsky and G. Zanzotto. Fine-scale microstructures and metastability in one-dimensional elasticity. *Meccanica*, 30:557–589, 1995.

[TZ96] L. Truskinovsky and G. Zanzotto. Ericksen's Bar Revisited: Energy Wiggles. *Journal of the Mechanics and Physics of Solids*, 44:1371–1408, 1996.

[VCNM90] G. Venkataraman, Y-W. Chung, Y. Nakasone, and T. Mura. Free energy formulation of fatigue crack initiation along persistent slip bands: calculation of the S-N curves and crack depths. *Acta Metallurgica et Materialia*, 18:31–40, 1990.

[WA85] D. Walgraef and E. C. Aifantis. Dislocation patterning in fatigued metals as a result of dynamical instabilities. *Journal of Applied Physics*, 58:688–691, 1985.

[Wil82] H. G. H. Wilsdorf. The Role of Glide and Twinning in the Final Separation of Ruptured Gold Crystals. *Acta Metallurgica*, 23:1247–1258, 1982.

[Win74] A. T. Winter. A model for the fatigue of copper at low plastic strain amplitudes. *Philosophical Magazine*, 29:719–738, 1974.

[WM84] R. Wang and H. Mughrabi. Secondary cyclic hardening in fatigued copper monocrystals and polycrystals. *Materials Science and Engineering*, 63:147–163, 1984.

[Woo58] W. A. Wood. Formation of fatigue cracks. *Philosophical Magazine*, 3:692–699, 1958.

[Woo73] P.J. Woods. Low-amplitude fatigue of copper and copper-5 at. crystals. *Philosophical Magazine*, 28:155–193, 1973.

[Yos65] K. Yosida. *Functional Analysis.* Springer-Verlag, Berlin, 1965.

[Yum89] L. Yumen. Low-energy dislocation structure in cyclycally deformed quench-tempered steel. *Materials Science and Engineering*, A113:237–244, 1989.